

Proton-number fluctuations in $\sqrt{s_{NN}} = 2.4$ GeV Au + Au collisions studied with the High-Acceptance DiElectron Spectrometer (HADES)

J. Adamczewski-Musch,⁵ O. Arnold,^{11,10} C. Behnke,⁹ A. Belounnas,¹⁷ A. Belyaev,⁸ J. C. Berger-Chen,^{11,10} A. Blanco,² C. Blume,⁹ M. Böhmer,¹¹ P. Bordalo,² S. Chernenko,^{8,*} L. Chlad,¹⁸ I. Ciepał,³ C. Deveau,¹² J. Dreyer,⁷ E. Epple,^{11,10} L. Fabbietti,^{11,10} O. Fateev,⁸ P. Filip,¹ P. Fonte,^{2,†} C. Franco,² J. Friese,¹¹ I. Fröhlich,⁹ T. Galatyuk,^{6,5} J. A. Garzón,¹⁹ R. Gernhäuser,¹¹ M. Golubeva,¹³ R. Greifehagen,^{7,‡} F. Guber,¹³ M. Gumberidze,^{5,6} S. Harabasz,^{6,4} T. Heinz,⁵ T. Hennino,¹⁷ S. Hlavac,¹ C. Höhne,^{12,5} R. Holzmann,⁵ A. Ierusalimov,⁸ A. Ivashkin,¹³ B. Kämpfer,^{7,‡} T. Karavicheva,¹³ B. Kardan,⁹ I. Koenig,⁵ W. Koenig,⁵ M. Kohls,⁹ B. W. Kolb,⁵ G. Korcyl,⁴ G. Kornakov,⁶ F. Kornas,⁶ R. Kotte,⁷ A. Kugler,¹⁸ T. Kunz,¹¹ A. Kurepin,¹³ A. Kurilkin,⁸ P. Kurilkin,⁸ V. Ladygin,⁸ R. Lalik,⁴ K. Lapidus,^{11,10} A. Lebedev,¹⁴ L. Lopes,² M. Lorenz,⁹ T. Mahmoud,¹² L. Maier,¹¹ A. Malige,⁴ A. Mangiarotti,² J. Markert,⁵ T. Matulewicz,²⁰ S. Maurus,¹¹ V. Metag,¹² J. Michel,⁹ D. M. Mihaylov,^{11,10} S. Morozov,^{13,15} C. Müntz,⁹ R. Münzer,^{11,10} L. Naumann,⁷ K. Nowakowski,⁴ Y. Parpottas,^{16,§} V. Pechenov,⁵ O. Pechenova,⁵ O. Petukhov,¹³ K. Piasecki,²⁰ J. Pietraszko,⁵ W. Przygoda,⁴ K. Pysz,³ S. Ramos,² B. Ramstein,¹⁷ N. Rathod,⁴ A. Reshetin,¹³ P. Rodriguez-Ramos,¹⁸ P. Rosier,¹⁷ A. Rost,⁶ A. Rustamov,⁵ A. Sadovsky,¹³ P. Salabura,⁴ T. Scheib,⁹ H. Schuldes,⁹ E. Schwab,⁵ F. Scozzi,^{6,17} F. Seck,⁶ P. Sellheim,⁹ I. Selyuzhenkov,^{5,15} J. Siebenson,¹¹ L. Silva,² U. Singh,⁴ J. Smyrski,⁴ Yu. G. Sobolev,¹⁸ S. Spataro,²¹ S. Spies,⁹ H. Ströbele,⁹ J. Stroth,^{9,5} C. Sturm,⁵ O. Svoboda,¹⁸ M. Szala,⁹ P. Tlusty,¹⁸ M. Traxler,⁵ H. Tsertos,¹⁶ E. Usenko,¹³ V. Wagner,¹⁸ C. Wendisch,⁵ M. G. Wiebusch,⁹ J. Wirth,^{11,10} D. Wójcik,²⁰ Y. Zanevsky,^{8,*} and P. Zumbach⁵

(HADES Collaboration)

¹*Institute of Physics, Slovak Academy of Sciences, 84228 Bratislava, Slovakia*

²*LIP (Laboratório de Instrumentação e Física Experimental de Partículas), 3004-516 Coimbra, Portugal*

³*Institute of Nuclear Physics, Polish Academy of Sciences, 31-342 Kraków, Poland*

⁴*Smoluchowski Institute of Physics, Jagiellonian University of Cracow, 30-059 Kraków, Poland*

⁵*GSI Helmholtzzentrum für Schwerionenforschung GmbH, 64291 Darmstadt, Germany*

⁶*Technische Universität Darmstadt, 64289 Darmstadt, Germany*

⁷*Institut für Strahlenphysik, Helmholtz-Zentrum Dresden-Rossendorf, 01314 Dresden, Germany*

⁸*Joint Institute of Nuclear Research, 141980 Dubna, Russia*

⁹*Institut für Kernphysik, J. W. Goethe-Universität, 60438 Frankfurt, Germany*

¹⁰*Excellence Cluster "Origin and Structure of the Universe," 85748 Garching, Germany*

¹¹*Physik Department E62, Technische Universität München, 85748 Garching, Germany*

¹²*II. Physikalisches Institut, Justus Liebig Universität Giessen, 35392 Giessen, Germany*

¹³*Institute for Nuclear Research, Russian Academy of Science, 117312 Moscow, Russia*

¹⁴*Institute of Theoretical and Experimental Physics, 117218 Moscow, Russia*

¹⁵*National Research Nuclear University MEPhI (Moscow Engineering Physics Institute), 115409 Moscow, Russia*

¹⁶*Department of Physics, University of Cyprus, 1678 Nicosia, Cyprus*

¹⁷*Institut de Physique Nucléaire, CNRS-IN2P3, Université Paris-Sud, Université Paris-Saclay, F-91406 Orsay Cedex, France*

¹⁸*Nuclear Physics Institute, The Czech Academy of Sciences, 25068 Rez, Czech Republic*

¹⁹*LabCAF. F. Física, Universidad de Santiago de Compostela, 15706 Santiago de Compostela, Spain*

²⁰*Uniwersytet Warszawski, Wydział Fizyki, Instytut Fizyki Doświadczalnej, 02-093 Warszawa, Poland*

²¹*Dipartimento di Fisica and INFN, Università di Torino, 10125 Torino, Italy*



(Received 21 February 2020; accepted 9 June 2020; published 24 August 2020)

We present an analysis of proton-number fluctuations in $\sqrt{s_{NN}} = 2.4$ GeV $^{197}\text{Au} + ^{197}\text{Au}$ collisions measured with the High-Acceptance DiElectron Spectrometer (HADES) at GSI Helmholtzzentrum für Schwerionenforschung, Darmstadt. With the help of extensive detector simulations done with Isospin Quantum Molecular Dynamics (IQMD) transport model events including nuclear clusters, various nuisance effects influencing the observed proton cumulants have been investigated. Acceptance and efficiency corrections have been applied as a function of fine-grained rapidity and transverse momentum bins, as well as considering local track density dependencies. Next, the effects of volume changes within particular centrality selections have been considered

*Deceased.

†Present address: Coimbra Polytechnic, ISEC, Coimbra, Portugal.

‡Present address: Technische Universität Dresden, 01062 Dresden, Germany.

§Present address: Frederick University, 1036 Nicosia, Cyprus.

and beyond-leading-order corrections have been applied to the data. The efficiency and volume-corrected proton number moments and cumulants K_n of orders $n = 1, 2, 3$, and 4 have been obtained as a function of centrality and phase-space bin, as well as the corresponding correlators C_n . We find that the observed correlators show a power-law scaling with the mean number of protons, i.e., $C_n \propto \langle N \rangle^n$, indicative of mostly long-range multiparticle correlations in momentum space. We also present a comparison of our results with Au + Au collision data obtained at the Relativistic Heavy Ion Collider (RHIC) at similar centralities but higher $\sqrt{s_{NN}}$.

DOI: [10.1103/PhysRevC.102.024914](https://doi.org/10.1103/PhysRevC.102.024914)

I. INTRODUCTION

Lattice QCD calculations sustain that, at vanishing baryochemical potential μ_B and a temperature of order $T = 156$ MeV, the boundary between hadron matter and a plasma of deconfined quarks and gluons is a smooth crossover [1,2], whereas at finite μ_b and small T , various models based on chiral dynamics clearly favor a first-order phase transition [3], suggesting the existence of a critical endpoint (CEP). Although the QCD critical endpoint is a very distinct feature of the phase diagram, it cannot presently be located from first-principle calculations, and experimental observations are needed to constrain its position. Mapping the QCD phase diagram is therefore one of the fundamental goals of present-day heavy-ion collision experiments.

Observables expected to be sensitive to the CEP are fluctuations of overall conserved quantities—like the net electric charge, the net baryon number, or the net strangeness—measured within a limited part of phase space [4–6]. Phase space has to be restricted to allow for fluctuations in the first place, yet remain large enough to avoid the regime of small-number Poisson statistics [7]. Tallying the baryon number event by event is very challenging experimentally, as, e.g., neutrons are typically not reconstructed in the large multipurpose charged-particle detectors in operation. It has been argued, however, that net-proton fluctuations too should be sensitive to the proximity of the CEP: first, on principal grounds because of the overall isospin blindness of the sigma field [4] and, second, because of the expected equilibration of isospin in the bath of copiously produced pions in relativistic heavy-ion collisions [8]. Using the net proton number as a proxy of net-baryon fluctuations and by studying its μ_B dependence, one may therefore hope to constrain the location of the CEP in the phase diagram. This is best achieved with a beam-energy scan, the characteristic signature being a nonmonotonic evolution as a function of $\sqrt{s_{NN}}$ of any experimental observable sensitive to critical behavior.

Ultimately, the characteristic feature of a CEP is an increase and even divergence of spatial fluctuations of the order parameter. Most fluctuation measures originally proposed were related to variances of event-by-event observables such as particle multiplicities (net electric charge, baryon number, strangeness), particle ratios, or mean transverse momentum. Typically, the critical contribution to variances, i.e., second-order cumulants, is approximately proportional to ξ^2 , where ξ is the spatial correlation length which would ideally diverge at the CEP. The magnitude of ξ is limited trivially by the system size but much more so by finite-time effects, due to critical slowing down, to an estimated 2–3 fm [9–11]. In addition, the fluctuating quantities are obtained at the chemical freeze-out

point only which may be situated some distance away from the actual endpoint. This makes discovering a nonmonotonic behavior of any critical contribution to fluctuation observables a challenging task, particularly if those measures depend on ξ too weakly. To increase sensitivity, it was therefore proposed [5,6,12] to exploit the higher, i.e., non-Gaussian moments or cumulants of the multiplicity distribution as the latter are expected to scale like $K_n \sim \xi^{5n/2-3}$. In particular, K_4 is considered [13] to be universally negative when approaching the CEP from the low- μ_B region, i.e., by lowering $\sqrt{s_{NN}}$. For a more complete review of this theoretical background, see, e.g., Refs. [14–16].

It is also important to keep in mind that other sources can produce non-Gaussian moments: remnants of initial-state fluctuations, reaction volume fluctuations, flow, etc. A quantitative study of such effects is necessary to unambiguously identify the critical signal. It is clear that an energy scan of the QCD phase diagram is mandatory to understand and separate such nondynamical contributions from the genuine CEP effect, the latter being a nonmonotonic function of the initial collision energy $\sqrt{s_{NN}}$ as the CEP is approached and passed over. The fact that non-Gaussian moments have a stronger than quadratic dependence on ξ causes them to be much more sensitive signatures of the CEP. Because of the increased sensitivity, they are, however, also more strongly affected by the nuisance effects mentioned above and this must be investigated very carefully.

Various fluctuation observables have been scrutinized in heavy-ion collisions from Super Proton Synchrotron (SPS) to Large Hadron Collider (LHC) energies: at the SPS in particular, balance functions and scaled variances of charged particles [17,18], dynamical fluctuations of particle ratios [19,20], as well as proton intermittencies [21–24]; at the Relativistic Heavy Ion Collider (RHIC) and LHC, net-proton-number fluctuations [25–28], net-charge fluctuations [29–31], and net-kaon fluctuations [32]. In this context, the first RHIC beam-energy scan, covering center-of-mass energies of $\sqrt{s_{NN}} = 7.7$ –200 GeV, provided indications of a nonmonotonic trend with decreasing energy of the net-proton fluctuations [27,33]. Unfortunately, the limited statistical accuracy of these data as well as their low-energy cutoff do not yet allow for firm conclusions. A second approved scan aims, however, at greatly improving the statistical quality and at extending the measurements down to $\sqrt{s_{NN}} = 3$ GeV by complementing the standard collider mode with a fixed-target arrangement [34].

Here we present results from a high-statistics measurement of proton-number fluctuations in the reaction system $^{197}\text{Au} + ^{197}\text{Au}$ at $\sqrt{s_{NN}} = 2.4$ GeV done with the charged-particle spectrometer HADES

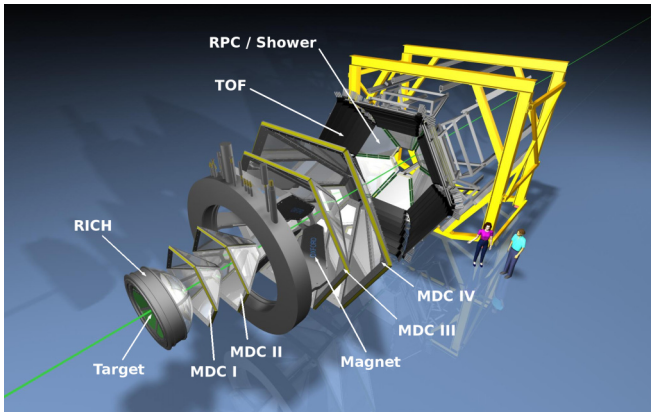


FIG. 1. Schematic explosion view of the HADES experiment. The forward wall hodoscope (FWALL) used for centrality selection (see text) is not shown on this picture.

at the SIS18 heavy-ion accelerator. In Sec. II of this article, a brief description of the experiment, as well as of the analysis procedures, is given. In Sec. III, the reconstructed proton multiplicity distributions are presented and their relevant features in terms of moments, cumulants, and factorial cumulants are discussed. In Sec. IV, we show and discuss the centrality and acceptance dependencies of (net-)proton-number fluctuations. Finally, Sec. V summarizes and concludes the paper.

II. THE Au + Au EXPERIMENT

A. The HADES setup

The six-sector high-acceptance spectrometer HADES operates at the heavy-ion synchrotron SIS18 of GSI Helmholtzzentrum für Schwerionenforschung in Darmstadt, Germany. Although its original design was optimized for dielectron spectroscopy, HADES is in fact a versatile charged-particle detector with large efficiency, good momentum resolution, and high trigger rate capability. The HADES setup consists of an ironless, six-coil toroidal magnet centered on the beam axis and six identical detector sectors located between the coils. With a nearly complete azimuthal coverage and spanning polar angles $\theta = 18\text{--}85^\circ$, this geometry results in a laboratory rapidity acceptance for protons of $y \simeq 0.1\text{--}1.8$. In the configuration used to measure the data discussed here, each sector was equipped with a central hadron-blind ring-imaging Cherenkov (RICH) detector, four layers of multiwire drift chambers (MDC) used for tracking (two in front of and two behind) the magnetic field volume, a time-of-flight detector made of plastic scintillator bars (TOF) at angles $\theta > 44^\circ$ and of resistive-plate chambers (RPC) for $\theta < 45^\circ$, and a preshower detector. Figure 1 shows a schematic view of the setup; more detailed technical information can be found in Ref. [35]. Hadron identification in HADES is based mainly on particle velocity, obtained from the measured time of flight, and on momentum, reconstructed by tracking the particle through the magnetic field using the position data from the MDC. Energy-loss information from the TOF as well as from the MDC tracking chambers can be used to augment

the overall particle identification power. The RICH detector, specifically designed for electron and positron candidate identification, was not used in the present analysis.

The event timing was provided by a $60\text{-}\mu\text{m}$ -thick monocrystalline diamond detector (START) positioned in the beam pipe 25 mm upstream of the first target segment. The diamond detector material [36] is radiation hard and has high count rate capability, large efficiency ($\epsilon \geq 0.9$), and very good time resolution ($\sigma_t \simeq 60$ ps). Through a 16-fold segmentation in x direction (horizontal) and in y direction (vertical) of its double-sided metallization, START also provided position information on the incoming beam particles, essential for beam focusing and position monitoring during the experiment. Combined with a multihit-capable time-to-digital converter (TDC), the fast START signal can be used to recognize and largely suppress event pileup within a time slice of ± 0.5 μs centered on an event of interest. Furthermore, as discussed below, the easily identifiable $^{197}\text{Au} + ^{12}\text{C}$ reactions in the diamond material of the START can be used to set a limit on background from Au reactions on light nuclei (H, C, N, and O) in the target holder material.

A forward hodoscope (FWALL), positioned 6.9 m downstream of the target and covering polar angles of $\theta = 0.33\text{--}7.2^\circ$ was used to determine the reaction plane angle and the event centrality. This device comprises 288 square tiles made of 25.4-mm-thick plastic scintillator and each read out with a photomultiplier tube. The FWALL has limited particle identification capability based on the measured time of flight and energy loss in the scintillator.

The $^{197}\text{Au} + ^{197}\text{Au}$ reactions investigated took place in a stack of 15 gold pellets of 25 μm thickness, adding up to 0.375 mm and corresponding to a nuclear interaction probability of 1.35%. Each of the 2.2-mm-diameter gold pellets was glued onto the central 1.7-mm eyelet of a $7\text{-}\mu\text{m}$ -thick Kapton holding strip. These strips were in turn supported by a carbon fiber tube of inner diameter 19 mm and wall thickness 0.5 mm, realizing an inter-pellet spacing (pitch) of 3.7 mm. All target holder parts were laser cut with a tolerance of 0.1 mm in all dimensions (see Ref. [37] for more details). The total length of the segmented target assembly was 55 mm. This design (target segmentation, low- Z and low-thickness holder) was optimized to minimize both multiple scattering of charged particles and conversion of photons into e^+e^- pairs in the target. It also helped to minimize production of spallation protons, that is emission of protons from any material in the target region through secondary knockout reactions induced by primary particles.

B. Online trigger and event selection

In the present experiment, a gold beam with a kinetic energy of $E_{\text{kin}} = 1.23A$ GeV and an average intensity of $1\text{--}2 \times 10^6$ particles per second impinged onto the segmented gold target. Several physics triggers (PT) were implemented to start the data readout based on hardware thresholds set on the analog multiplicity signal corresponding to at least 5 (PT2) or 20 (PT3) hits in the TOF detector, and coincident with a signal in the in-beam diamond START detector. The PT2 trigger was downscaled ($\div 8$) and PT3 was the main event

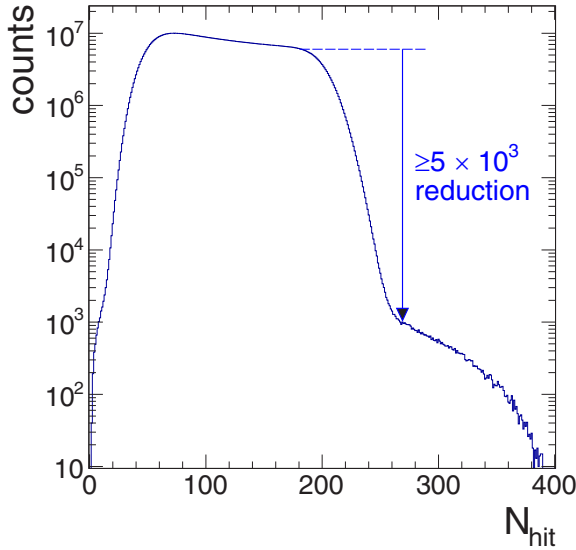


FIG. 2. Distribution of the total number of hits in the HADES time-of-flight detectors TOF and RPC in the 43% most central Au + Au events accepted by the PT3 trigger. The tiny contribution of order $\leq 2 \times 10^{-4}$, visible for $N_{\text{hit}} > 260$, is attributed to event pileup.

trigger covering the 43% most central collisions.¹ In total, 2.1×10^9 high-quality PT3 events were recorded of which, for performance reasons mostly, we used only a subset of 1.6×10^8 events in the current analysis.

C. Event pileup

Running the HADES experiment with high beam currents bears the danger of event pileup, that means of having a sizable chance that two or even more consecutive (minimum bias) beam-target interactions take place within the readout window opened by a trigger. Such events appear to have higher than average track multiplicity and, if their fraction becomes sufficiently large, they will have a noticeable impact on the observed event-by-event particle-number fluctuations. The multihit TDC of the START detector provided, however, the possibility to reject piled up events by counting the number of registered incident beam particles within a $\pm 0.5 \mu\text{s}$ time window centered on any accepted trigger. However, because of the finite efficiency of the START (determined to be $\geq 90\%$), a remaining small contribution of pileup events is still visible in Fig. 2 as a shoulder at large N_{hit} values. From the size of the resulting “step,” one can estimate the overall pileup probability in our event sample to be $\leq 2 \times 10^{-4}$.

In fact, the contamination of identified proton yields by pileup turns out to be even much smaller. Because of its excellent timing properties, the START allowed us to continuously monitor the instantaneous beam rate, typically of order 4–8 ions/ μs , i.e., a factor of 4 larger than the rate averaged over beam spills. With this rate and a total beam interaction probability of 1.7% (on START, gold targets,

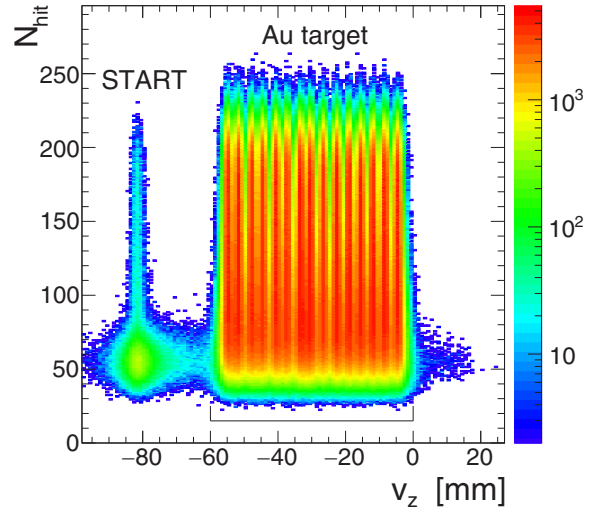


FIG. 3. Total number of charged hits in the time-of-flight detectors (TOF and RPC) as a function of the reconstructed event vertex v_z along the beam axis z . The 15 gold target segments are clearly separated from the diamond START detector as well as from one another; the horizontal solid line indicates the vertex cut used to select reactions in the targets. Note that the faint high- N_{hit} tail ($N_{\text{hit}} > 100$) visible for the START detector is due to Au + Au reactions in its thin gold platings.

and Kapton combined), and realizing that particle identification via momentum-velocity correlation implicitly puts a tight constraint on the flight time of tracks (with $|\Delta t| < 1.5 \text{ ns}$) for them to fulfill the required $p - \beta$ congruence, one can estimate the pileup effect on identified particles to be $\leq 3 \times 10^{-5}$. As discussed further below, this value is low enough for pileup to be of no concern to our fluctuation analysis.

D. Offline event selection and centrality definition

Offline, events were selected by requiring that the global event vertex, determined from reconstructed tracks with a resolution of $\sigma_x = \sigma_y \simeq 0.7 \text{ mm}$ and $\sigma_z \simeq 0.9 \text{ mm}$, was within the $\approx 60 \text{ mm}$ extension of the segmented target. Figure 3 shows the combined number of hits observed in the RPC and TOF as a function of the reconstructed event vertex v_z along the beam axis. The diamond START detector and the segmented gold targets are clearly distinguishable along z , and the difference in hit multiplicity between Au + Au reactions on the target pellets and Au + C reactions on the diamond detector is very evident as well. The amount of reactions on the START detector accepted by the PT3 trigger can furthermore be used to put an upper limit on a possible contamination from reactions on the Kapton holding strips (containing H, C, N, and O) by comparing the effective thickness and resulting interaction probability in Kapton and START, respectively. Considering the intricate crisscross geometry of those strips [37], the diameter of their central eyelet, and the tight focus of the gold beam, we estimate that reactions on Kapton can contaminate the recorded rate of semicentral Au + Au events at most on the level of 10^{-4} . This is also supported by control

¹The centrality range selected by the HADES trigger was determined with Glauber–Monte Carlo calculations [38].

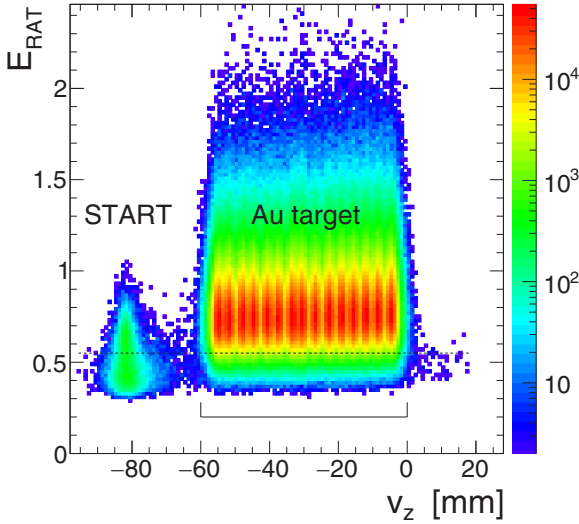


FIG. 4. Ratio of transverse to longitudinal energy E_{RAT} as a function of the reconstructed event vertex along the beam axis z . The horizontal dashed line indicates the $E_{RAT} > 0.55$ cut used to further suppress Au + C reactions in the Kapton strips of the target holder. The solid line delimits the vertex cut applied on the target region.

data taken with the Au beam vertically offset by 3.5 mm such as to miss the gold targets altogether and hit only Kapton. Note finally that the Au + C contamination affects mostly the peripheral event classes whereas central Au + Au events are basically free from it because of their much higher average hit multiplicity.

As the lateral event vertex resolution of $\sigma_{\perp} \simeq 1.1$ mm was not sufficient to fully avoid reactions on the Kapton strips, in the analysis, this background has been reduced further by applying a cut on the quantity E_{RAT} defined as the ratio of total detected transverse to total detected longitudinal energy in the laboratory,² namely

$$E_{RAT} = \frac{E_{\perp}^{\text{tot}}}{E_{\parallel}^{\text{tot}}} = \frac{\sum_i E_{\perp,i}}{\sum_i E_{\parallel,i}} = \frac{\sum_i E_i \sin \theta_i}{\sum_i E_i \cos \theta_i}, \quad (1)$$

where E_i and θ_i are the particle's total energy and polar angle, respectively, and the index i runs over all detected and identified particles. The $E_{RAT} > 0.55$ cut applied, shown in Fig. 4 as horizontal dashed line, suppresses Au + C reactions by an additional factor of 4, while losing less than 2% of the Au + Au events. The remaining Au + C contamination is thus at most 2.5×10^{-5} for all centralities. Our schematic simulations show that this level of contamination is of no concern for our proton cumulant analyses, in agreement also with conclusions resulting from similar investigations discussed in Refs. [40,41]. Finally, by monitoring the mean charged particle multiplicity per each HADES sector,³ we have made sure that in the data runs selected for the present

²Note that our definition of E_{RAT} differs from the one used for centrality determination in Ref. [39].

³Averaged over sets of 50 000–100 000 PT3 events, corresponding to about 2–3 min of run time.

TABLE I. Nuisance effects on the proton multiplicity measured in $\sqrt{s_{NN}} = 2.4$ GeV Au+Au collisions with HADES. Listed are the estimated maximum relative contributions of background events (top rows) and of background to the proton yield arising within the events of interest (bottom rows). For comparison, the expected antiproton yield, estimated from a thermal model fit to the various particle yields observed at freeze-out in the 10% most central events, is listed as well.

Nuisance effect	Relative contribution
Event pileup	$\leq 3 \times 10^{-5}$
Au+C reactions	$\leq 2.5 \times 10^{-5}$
PID impurities	$\leq 10^{-3}$
Knockout reactions	$\leq 3 \times 10^{-3}$
Hyperon decays	$\leq 6.5 \times 10^{-4}$
Antiprotons (model fit)	$\simeq 2 \times 10^{-8}/\text{evt}$

analysis no hardware conditions occurred that could have caused substantial drifts or even jumps of the proton yield. All estimates of various background contributions potentially affecting the proton multiplicities measured in our experiment are summarized in Table I.

In the HADES experiment, event centrality determination is usually done by putting a selection on either the total number of hits N_{hit} in the time-of-flight detectors TOF and RPC or on the total number of tracks N_{trk} reconstructed in the MDC [38]. It is, however, important to realize that in our investigation of particle-number fluctuations, correlations exist between the observable of interest, that is, the number of protons N_{prot} emitted into a given phase space and the N_{hit} or N_{trk} observable used to constrain the event centrality. At a bombarding energy of 1.23A GeV, protons constitute by far the most dominant particle species and, as every detected proton will produce at least one hit and also one reconstructed track, we expect indeed very strong autocorrelations when using N_{hit} or N_{trk} as centrality selectors. A systematic simulation study [42] done with UrQMD transport model events has already demonstrated the disturbing effect of autocorrelations on fluctuation observables. To avoid or, at least, minimize such effects, we have instead used for centrality determination the cumulated charge ΣQ_{FW} of all particles observed in the FWALL detector. Figure 5 shows this measured quantity as a function of the number of hits in the HADES time-of-flight detectors. The two observables anticorrelate, as expected, demonstrating that ΣQ_{FW} is also a useful measure of centrality. As discussed in more detail in Sec. V, a weak anticorrelation between N_{prot} and ΣQ_{FW} does exist as well, but its influence on the proton-fluctuation observables can be corrected for. The coverage of the FWALL being restricted to a range of 0.33–7.2° in polar angle results in the loss of the most peripheral events where the projectile fragment passes undetected through the central hole left open around the beam pipe. For such events, ΣQ_{FW} tends to decrease again, visible as a down-bending in Fig. 5, which contaminates the most central selections with peripheral events. This can be cured, i.e., the monotonicity of ΣQ_{FW} with centrality can be restored, by applying a rather loose 2D cut on ΣQ_{FW} vs N_{hit} . Centrality

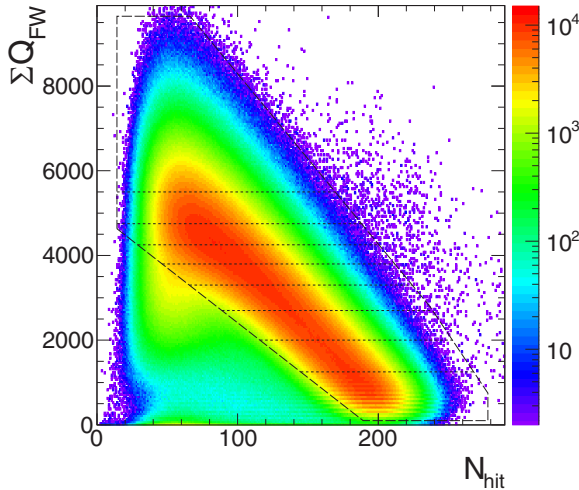


FIG. 5. Sum signal ΣQ_{FW} measured in the forward wall vs number of hits N_{hit} in the TOF and RPC. The black long-dashed line indicates a loose 2D cleaning cut applied to remove the contamination from peripheral events. Centrality selections, e.g., in steps of 5%, were done by applying additional, more restrictive cuts on ΣQ_{FW} as indicated by the set of short-dashed horizontal lines.

selections are realized, as indicated in Fig. 5, by additional dedicated cuts on ΣQ_{FW} .

From Glauber–Monte Carlo calculations and also a direct comparison with UrQMD model calculations (version 3.4) [43], we determined that the PT3 hardware trigger selected only the 43% most central events [38]. For the fluctuation analysis, a finer centrality binning was realized by applying on the measured ΣQ_{FW} signal a sequence of 5% cuts or, in some instances, 10% cuts. The behavior of the various cuts was studied in detailed detector simulations using the GEANT3 software package [44]. For that purpose, Au + Au events were generated with the Isospin Quantum Molecular Dynamics (IQMD) transport model (version c8) [45,46] supplemented with a minimum spanning tree (MST) clustering algorithm in coordinate space [47], which allowed us to obtain events including bound nuclear clusters like d , t , ${}^3\text{He}$, ${}^4\text{He}$, etc. At the bombarding energies where HADES takes data, the clusters contribute substantially to the track density; in our Au + Au data they correspond indeed to about 40% of the charged baryons detected [48].

E. Proton reconstruction and identification

Charged-particle trajectories in HADES were reconstructed using the MDC hit information [35,49]; in this procedure, the trajectories were constrained to start from the vicinity of the global event vertex. The resulting tracks were subjected to several quality selections provided by the hit matching and Runge-Kutta track fitting algorithms. Finally, the retained tracks were spatially correlated with time-of-flight information from TOF or RPC, and—for lepton candidates—also with ring patterns found in the RICH as well as electromagnetic shower signatures from the preshower detector.

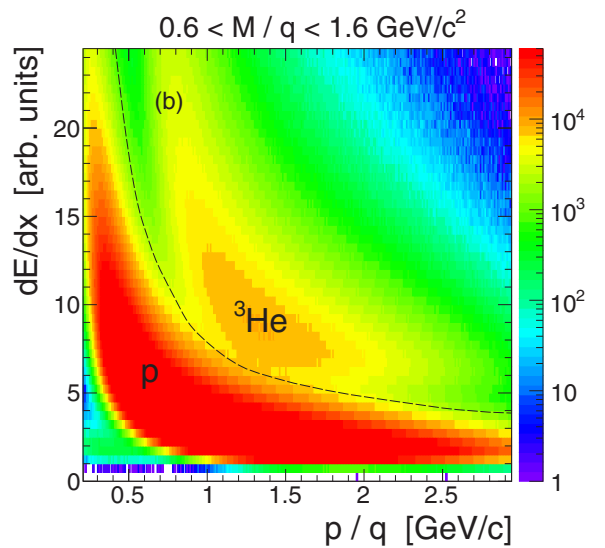
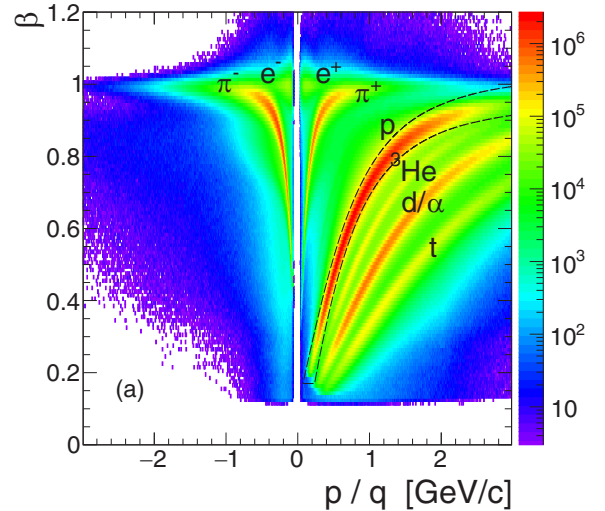


FIG. 6. Particle identification (PID) based on particle velocity vs momentum correlations as well as on energy loss vs momentum correlations. Shown in panel (a) is $\beta = v/c$ of the detected particle, with velocity v obtained from the time of flight, as a function of its p/q , where p is the particle momentum and q is its charge. Note that the weak branch lying between p and d/α are ${}^3\text{He}$ nuclei. The dashed curves delineate the condition used to select protons. The weak ${}^3\text{He}$ contamination remaining in this selection is suppressed by applying an additional condition on the energy-loss relation, dE/dx vs p/q , shown in panel (b) for the masses fulfilling $0.6 < M/q < 1.6 \text{ GeV}/c^2$.

Protons were identified by using their velocity versus momentum correlation as well as their characteristic energy loss in the MDC. As seen in Fig. 6(a), the proton branch is the most prominent one next to the charged pions and light nuclei (deuterons, tritons, and He isotopes). A $\pm 2\sigma$ -wide cut on this branch⁴ was used to select the protons. An additional condition on the energy-loss signal in the MDC, shown in Fig. 6(b),

⁴Applying a $\pm 2\sigma$ cut on velocity per 40 MeV/c momentum bin.

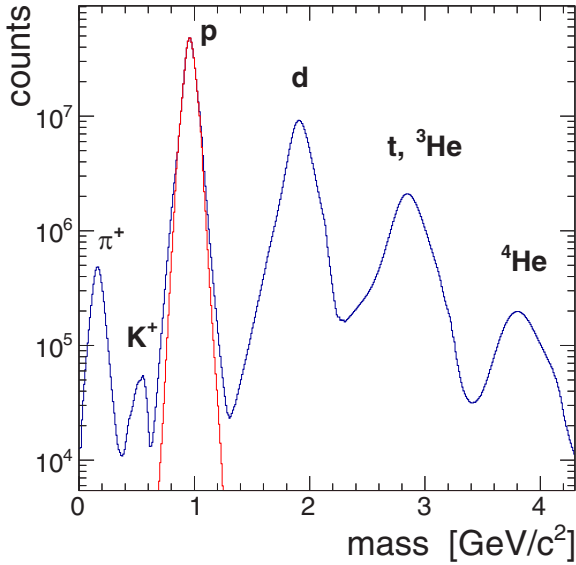


FIG. 7. Particle mass distribution of reconstructed tracks—as deduced from particle velocity, momentum, and energy loss—for positive particles within the phase-space bin of interest ($y = y_0 \pm 0.5$ and $0.4 < p_t < 1.6$ GeV/c). The masses selected by the proton cut (see Fig. 6) as well as the $Z = 1$ condition are shown in red. Contaminations from lower masses (π^+ , K^+) and higher masses (d , t , He) are below 0.1%, resulting in an overall proton purity > 0.999 .

was applied to further suppress a potential residual contamination caused by the adjacent ^3He branch, resulting in a proton purity of ≥ 0.999 for tracks with $0.4 < p_t < 1.6$ GeV/c and $y = y_0 \pm 0.5$, where $y_0 = 0.74$ is the Au + Au center-of-mass rapidity. This is plainly visible in the reconstructed particle mass spectrum, shown in Fig. 7 with and without the proton selection cuts: The about thousandfold weaker K^+ signal on the left side of the proton peak is evidently of no concern and the few-percent ^3He signal, visible as a weak branch in Fig. 6, is indeed efficiently relocated to its correct position when assigning the charge $Z = 2$ with help of the dE/dx information. Notice that, with the charge assignment, the ^4He hits are likewise moved to their proper position in the mass spectrum.

We have investigated the production of secondary protons, i.e., protons knocked out from target and near-target material by primary hadrons (mostly neutrons, protons, and pions), using our GEANT3 detector simulation with GCALOR as hadronic interaction package [50]. We found that their relative contribution to the proton yield in the phase space bin usable for the fluctuation analysis ($y \in y_0 \pm 0.5$ and $0.4 < p_t < 1.6$ GeV/c, see below) is of order $\leq 3 \times 10^{-3}$ (50% from p , 45% from n , and 5% from π reactions). Furthermore, the relative contribution to the total yield due to protons stemming from weak decays of Λ and Σ^0 hyperons produced in the collision can be estimated from data to be of order 6.5×10^{-4} only [51]. These contributions to the proton multiplicity are also listed in Table I and their implications on the fluctuation analysis are discussed in Sec. VII. Note finally that the production of antiprotons is far below threshold at our bombarding energy and does not contribute any observable hits in the detector.

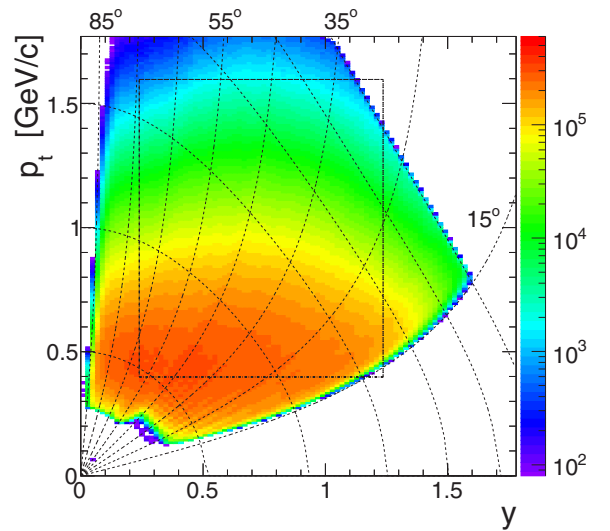


FIG. 8. Identified proton yield as a function of laboratory rapidity y and transverse momentum p_t . The acceptance is constrained by the geometry of HADES ($\theta = 15\text{--}85^\circ$) and by momentum cuts ($0.3 < p < 3$ GeV/c). Thin dashed curves indicate the polar angle, in steps of 10° , and proton momentum, in steps of 0.5 GeV/c. The dashed rectangle corresponds to the phase space selected for the fluctuation analysis: $y = y_0 \pm 0.5$ and $0.4 < p_t < 1.6$ GeV/c, where midrapidity $y_0 = 0.74$.

From a thermal model fit to the particle yields measured at freeze-out, we estimate the antiproton yield to be of order 2×10^{-8} /event in the 10% most central Au + Au collisions.

F. Proton acceptance

The yield of identified protons is shown in Fig. 8 as a function of laboratory rapidity y and transverse momentum p_t . The proton phase-space coverage is constrained by the polar angle acceptance of HADES ($\theta_{\text{lab}} = 15\text{--}85^\circ$) as well as by a low-momentum cut (≈ 0.3 GeV/c) due to energy loss in material and deflection in the magnetic field, and an explicit high-momentum cut (3 GeV/c) applied in the proton identification. This results in a useful rapidity coverage of about 0.1–1.5, which is quite well centered on the midrapidity $y_0 = 0.74$ of the 1.23A GeV fixed-target reaction. However, to guarantee a close to uniform and symmetric about midrapidity acceptance, we have restricted the proton-fluctuation analysis to the rapidity range $y = 0.24\text{--}1.24$ and transverse momentum range $p_t = 0.4\text{--}1.6$ GeV/c resulting in the dashed rectangle overlaid on Fig. 8. Notice that these selections leave two small open corners in the acceptance. In addition, the azimuthal acceptance of HADES is also not complete because of the six gaps occupied by the magnet cryostat [35]. All of these are taken into account in the efficiency corrections based on full detector simulations, as discussed in Sec. III.

G. Characterizing the proton multiplicity distributions

Before discussing corrections for detector inefficiency, we first take a look at the observed proton multiplicity distribution, that is the distribution of the number N_p of protons

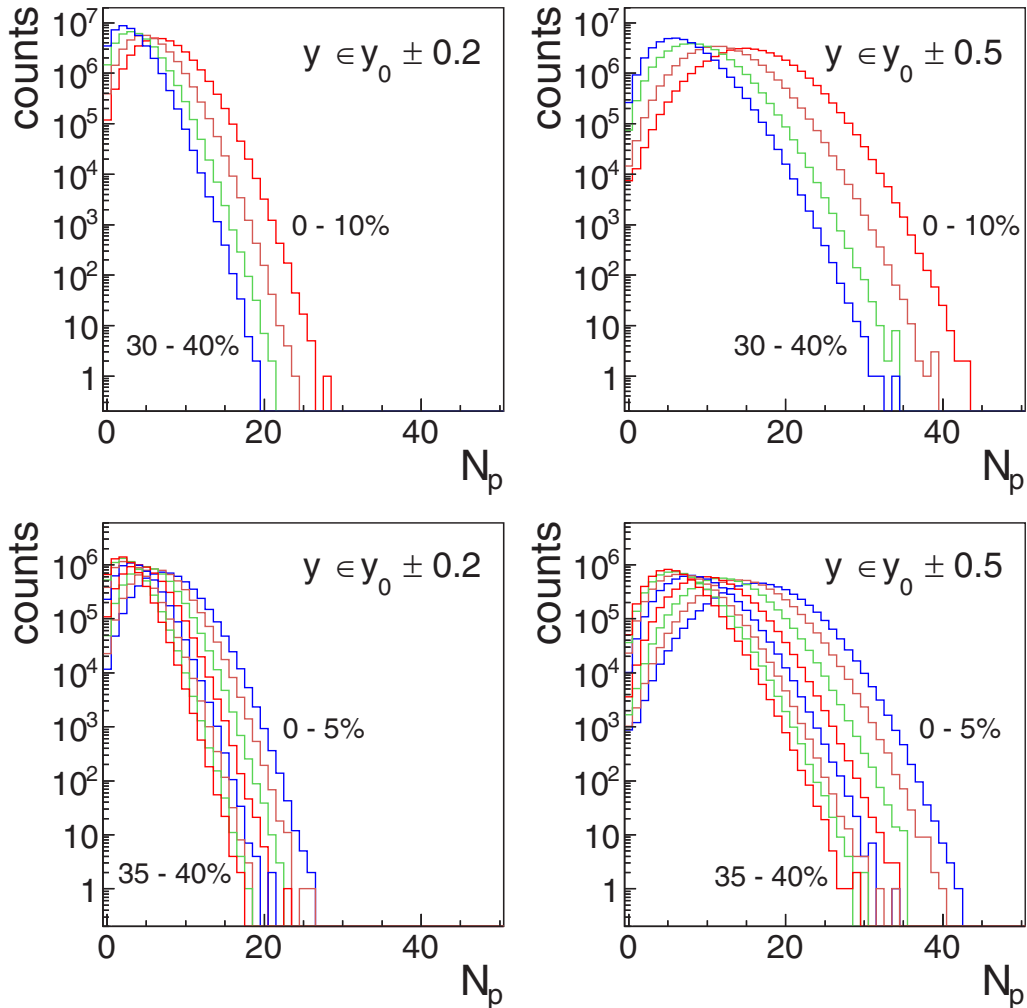


FIG. 9. Raw multiplicity distributions of fully reconstructed and identified protons in Au + Au collisions within a given phase-space bin ($y \in y_0 \pm \Delta y$ and $p_t = 0.4\text{--}1.6$ GeV/ c) and for different centrality selections based on the observable ΣQ_{FW} , using 10%-wide bins (top) or 5%-wide bins (bottom).

reconstructed and identified within the phase space delineated in Fig. 8. We have histogrammed this distribution for various centrality selections based on the FWALL ΣQ signal, as discussed before, and for various phase-space bins $y \in y_0 \pm \Delta y$ (with $\Delta y = 0.05\text{--}0.5$) and $p_t = 0.4\text{--}1.6$ GeV/ c . Figure 9 shows the proton multiplicity distributions obtained in 5% or 10% centrality bins, and for a rapidity bin of $\Delta y = 0.2$ or $\Delta y = 0.5$, respectively. The basic idea of the fluctuation analysis is to remove from these “raw” distributions any distorting nuisance effects, namely detector inefficiencies and reaction volume fluctuations, and then to systematically characterize their shape in terms of higher order moments and/or cumulants. Procedures to achieve this are discussed in the following two sections. Because of the comfortably large size of our proton sample, resulting in $\simeq 2 \times 10^7$ and $\simeq 4 \times 10^7$ events per centrality selection for the 5% and 10% bins respectively, the shape of the proton distributions can be followed in Fig. 9 over more than six orders of magnitude. From this, one may expect [52,53] that their cumulants can be extracted up to fourth order at least with sufficient statistical accuracy (i.e., $<5\text{--}10\%$) to quantify significant deviations

from a simple Poisson or binomial baseline. In fact, in case of large deviations from such a baseline, much smaller statistics may be needed, as has been argued in Ref. [54].

As already stated in the introduction, conserved quantities like baryon number, electric charge, or strangeness within a restricted phase space and, in particular, their critical or pseudo-critical behavior are usually characterized by the higher order cumulants of the observed particle number distribution. In an experiment, it is often convenient to first determine the moments $\langle N^n \rangle$ or the central moments $\langle (N - \langle N \rangle)^n \rangle$ about the first moment. Then, from the moments, all other quantities like factorial moments $\langle N(N-1)(N-2)\cdots \rangle$, cumulants, or factorial cumulants can be computed with ease (see, e.g., Ref. [58]). In the literature [15,55,56] various notations⁵ for all of those quantities are in use and we do not want to propose

⁵Asakawa and Kitazawa use, e.g., $\langle N^n \rangle$ for moments, $\langle N^n \rangle_f$ for factorial moments, $\langle N^n \rangle_c$ for cumulants, and $\langle N^n \rangle_{fc}$ for factorial cumulants [15].

yet another one here. We just follow Bzdak and Koch [55]: M_n stands for moments of order n , K_n for cumulants, F_n for factorial moments, and C_n for factorial cumulants. For the acceptance and efficiency affected experimentally observed quantities, we use the corresponding lowercase letters, m_n , f_n , and k_n . Note also that deviations of a distribution from normality are usually characterized by nonzero values of the dimensionless quantities named skewness, $\gamma_1 = K_3/K_2^{3/2}$, and excess kurtosis, $\gamma_2 = K_4/K_2^2$. Yet other quantities referred to later in the text will be defined as needed.

The various moments and cumulants characterize a distribution in equivalent ways and a particular choice may just result from convenience of use in a given situation. Let us recall that moments M_n and factorial moments F_n transform into each other via the following relationships [57,58]:

$$\begin{aligned} M_n &= \sum_{l=1}^n s_2(n, l) F_l, \\ F_n &= \sum_{l=1}^n s_1(n, l) M_l, \end{aligned} \quad (2)$$

where $s_1(n, l)$ and $s_2(n, l)$ are the Stirling numbers of first and second kinds, respectively. Note that these relationships also hold between cumulants K_n and factorial cumulants C_n . Cumulants and moments, that is, K_n and M_n or C_n and F_n , can be related via recursion [59,60]:

$$\begin{aligned} K_n &= M_n - \sum_{l=1}^{n-1} \binom{n-1}{l-1} K_l M_{n-l}, \\ C_n &= F_n - \sum_{l=1}^{n-1} \binom{n-1}{l-1} C_l F_{n-l}, \end{aligned} \quad (3)$$

with the $\binom{n-1}{l-1}$ being binomial coefficients.

III. EFFICIENCY CORRECTIONS

The measured proton number distributions were obtained within the geometric acceptance of HADES, which is constrained in polar and azimuthal angles, as well as in a limited momentum range only. Furthermore, the proton yields are affected by inefficiencies of the detector itself and of the hit finding, hit matching, track fitting, and particle identification algorithms used in the reconstruction. Geometric acceptance losses are minimized in our analysis by restricting the proton phase space to the region indicated in Fig. 8. Note also that, in the following, we do not explicitly distinguish between losses due to finite acceptance and losses caused by hardware or analysis inefficiencies; we subsume all effects into one number which we just call detection efficiency ϵ_{det} .

With the HADES setup fully implemented in the detector modeling package GEANT3 [44] and with appropriate digitizing algorithms emulating the physical behavior of all detector components, we have performed realistic simulations of its

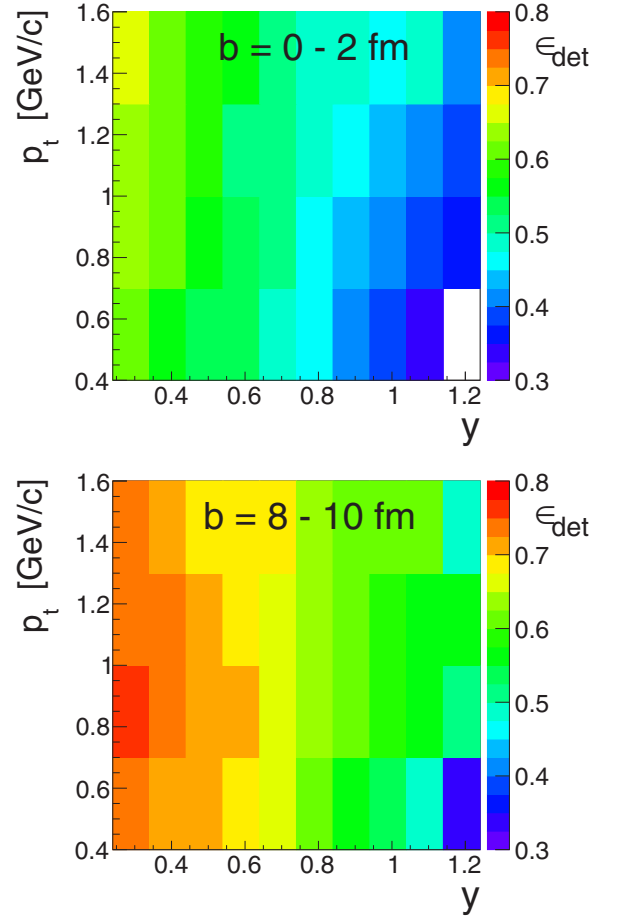


FIG. 10. Simulated proton detection efficiency ϵ_{det} in one sector of HADES as a function of rapidity y and transverse momentum p_t , and for two impact parameter ranges (left, $b = 8 - 10$ fm and right, $b = 0 - 2$ fm).

response to Au + Au collisions. In particular, using IQMD⁶ generated events, these simulations allowed us to systematically investigate the proton detection efficiency throughout the covered phase space. Figure 10 displays the calculated efficiency ϵ_{det} as a function of rapidity y and transverse momentum p_t for two centralities corresponding to narrow ranges of the collision impact parameter b . It appears clearly from these plots that the detection efficiency in HADES depends not only on phase-space bin (more strongly on y than on p_t) but also on the event centrality: Overall, the efficiency is considerably reduced in central events with respect to the more peripheral ones. This reduction can be connected to an increase of the hit and track densities in the detector with increasing particle multiplicity. In other words, larger occupancy in the detector lead to some deterioration of the reconstruction procedures. As both detection and reconstruction in HADES operate on one sector at a time, it is sufficient to investigate the efficiency on a per-sector basis. We illustrate this in Fig. 11 by plotting

⁶In this paper, a reference to IQMD always implies that a MST algorithm was used to add nuclear clusters to the event.

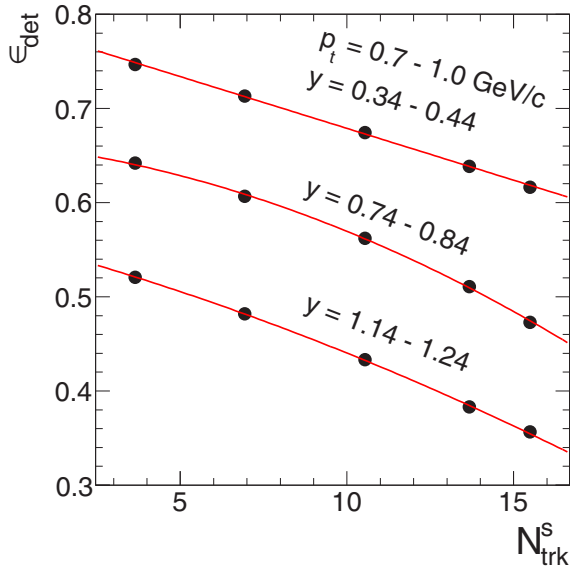


FIG. 11. Simulated proton detection efficiency ϵ_{det} as a function of the number of reconstructed tracks per sector N_{trk}^s , shown here for three out of the 40 narrow phase-space bins used in our analysis. Efficiency points correspond to 2-fm-wide impact-parameter slices centered at $b = 9, 7, 5, 3$, and 1 fm, respectively; curves are the polynomials adjusted to model the occupancy dependence of the efficiency.

for a few narrow phase-space bins the simulated detection efficiency ϵ_{det} in one HADES sector as a function of the number of particle tracks N_{trk}^s reconstructed in this sector, obtained by selecting events within a sequence of narrow b bins. Low-order polynomials have been fitted to the efficiency, as also shown in the figure. Such fits were done in all sectors and for 40 phase-space bins, using tenfold segmentation in y and fourfold in p_t . In fact, in most cases, a linear function turned out to be sufficient to model the observed behavior of $\epsilon = \epsilon(N_{\text{trk}}^s)$. Next, we discuss how these modeled efficiencies can be used to correct the measured proton number moments and cumulants.

Efficiency corrections of particle number cumulants have been extensively discussed in the literature [53,55,61–63]. They usually rely on the premise of a binomial efficiency model, that is, on the assumption that the detection processes of many particles in a detector are independent of each other. This implies that each particle has the same probability of being detected, irrespective of the actual number of particles hitting the detector in a given event. In such a case, the resulting multiplicity distribution of detected particles is a binomial distribution. A convenient property of the binomial efficiency model is that it leads to a particularly simple relationship⁷ for any order n between the factorial moments f_n of the distribution of detected particles and the factorial moments F_n

of the true particle distribution [55,62,64,65]:

$$f_n = \epsilon^n F_n, \quad (4)$$

where ϵ is the detection efficiency of a particle.

If ϵ is known, the true F_n can be calculated easily from the measured f_n , and all other true moments and cumulants can be obtained with the help of Eqs. (2) and (3). We have to handle, however, two more problems: First, as the efficiency depends on phase-space bin (see Fig. 10), we have to do efficiency corrections bin by bin and merge the corrected values into one global result. Second, we also have to take into account that the efficiencies depend on the number of particles actually hitting the detector (see Fig. 11) and therefore change from event to event. However, ways to pass both hurdles have been found and are discussed next.

The need to handle more than one efficiency value, ϵ , depending, e.g., on particle species or on the $y - p_t$ bin, had been recognized before and is discussed in Refs. [53,61,62]. In particular, in Ref. [61] so-called local factorial moments were introduced, i.e., factorial moments of particles in a given phase-space bin and obeying Eq. (4) individually, so that efficiency corrections can be done bin-wise. In addition, based on a multinomial expansion of the full factorial moments F_n in terms of the corrected local moments, a prescription of how to sum over all phase-space bins was presented. Although formally correct, the procedure is rather awkward to implement, and it quickly turns prohibitively memory and CPU time intensive if applied to big event samples and/or a large number N_b of phase-space bins.

A much more efficient scheme based on factorial cumulants has been proposed in Refs. [62,63,66]. It omits the full multinomial expansion in terms of local factorial cumulants (or factorial moments), leading to a vast reduction in memory needs and computing time.⁸ We have implemented this scheme in our analysis, using factorial moments, however, and applied it directly to the efficiency correction of the proton moments. In doing so, we have partitioned the phase space covered by HADES (see Fig. 8) into 240 bins in total, namely 6 sectors \times 10 rapidity bins \times 4 p_t bins.

We have investigated two ways to overcome the second complication, that is, the dependence of the efficiency on the number of tracks: either by introducing an event-by-event recalculation of the efficiency correction or by using an unfolding procedure to directly retrieve the true particle distribution from the measured one.

A. Occupancy-dependent efficiency correction

The dependence of the detection and reconstruction efficiencies on track number leads evidently to an event-by-event change of ϵ_{det} . On condition that the binomial efficiency model remains valid or at least a good approximation, one can consider grouping the events into classes of identical

⁷This has also been extended to net particle numbers $N - \bar{N}$, where N and \bar{N} refer to the particles and antiparticles, respectively. However, at our beam energy we have to deal with protons only.

⁸E.g., the number of terms to be evaluated and stored at fourth order for N_b bins decreases from $[(N_b + 3)(N_b + 2)(N_b + 1)N_b]/24$ to a mere 13 terms, independent of N_b [63].

efficiency and apply the efficiency correction of Eq. (4) individually to each one of these classes. As has indeed been shown in Ref. [65], the efficiency-corrected factorial moments F_n of a superposition of particle distributions, stemming, e.g., from different event classes, can be obtained from the weighted means of the observed class factorial moments $f_n^{(i)}$ as

$$F_n = \sum_{i=0}^k a_i \frac{f_n^{(i)}}{\epsilon_i^n}, \quad (5)$$

where ϵ_i are the individual class efficiencies, a_i are the class weights normalized such that $\sum a_i = 1$, and the index i runs over all classes. Note that this is a generalization of Eq. (4) and it is also applicable to factorial cumulants, but not to moments and cumulants in general [65]. In particular, when the efficiency changes from event to event, each event of the sample analyzed can be considered as a class of its own and the relation still remains valid. This provides therefore a convenient way to apply efficiency corrections within the event analysis loop by, first, recalculating the efficiencies on the fly for all phase-space bins of interest as a function of the number of reconstructed tracks per sector as discussed in Sec. III and, second, computing the average factorial moments (using, e.g., Eq. (17) of Ref. [61]) or factorial cumulants (using, e.g., Eq. (61) of Ref. [63]). We have investigated this procedure in GEANT3 detector simulations using Au + Au events calculated with the IQMD transport model and we found good agreement of the corrected and true proton moments. This also supports the underlying assumption of eventwise binomial efficiencies in the HADES detector.

Note for completeness that nonbinomial efficiencies based on the hypergeometric or β -binomial distributions have been discussed in Ref. [67]. Although the properties of these somewhat *ad hoc* models are well known, they lack an obvious connection to physical phenomena playing a role in the actual detection process. In Appendix A, we propose yet another model, known as the urn occupancy model [68], that in fact possesses such an intuitive connection. It is, however, specifically tailored for detectors with a well-defined hardware segmentation like tiled hodoscopes, pixel telescopes, modular calorimeters, etc. The HADES setup, as a whole, does not fall into either category but we can still define for it a virtual subdivision and treat the number of virtual segments N_{seg} as a free parameter that, together with the single-hit efficiency ϵ_0 , can be adjusted to simulated proton distributions. Further below, we show and discuss the result of such a fit.

B. Response matrix and unfolding

Figure 12 shows simulated distributions of the number of detected protons N_{det} in HADES as a function of the number N_{in} of protons emitted into the phase space of interest for IQMD events with 0–10% (30–40%) centrality. These two-dimensional histograms represent the response of the detector for proton production in Au + Au collisions at a given centrality. Their shape is not only determined by the multiproton detection and reconstruction efficiency, but also by the shape

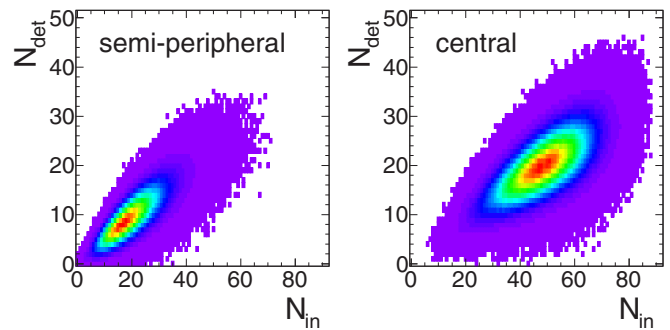


FIG. 12. Proton response matrices of the HADES detector simulated with IQMD clustering for two centrality selections, semiperipheral (30–40%) and central (0–10%). These matrices encode the distribution of the number N_{det} of reconstructed proton tracks—within the phase-space bin of interest (here $y \in y_0 \pm 0.5$)—for any given number N_{in} of protons emitted into this bin.

of the true proton multiplicity distribution presented as input.⁹ These response matrices have been obtained from the same simulation used to extract the efficiency per phase-space bin and centrality bin, discussed in the occupancy-dependent correction scheme, which basically assumes binomial efficiencies. On the other hand, any deviation from the binomial efficiency model would also be encoded in this response matrix. It is therefore appropriate to investigate whether unfolding of the measured proton distributions with the help of such response matrices is a useful approach to efficiency correction. In the context of particle-number-fluctuation analyses, a proof-of-principle simulation study of Bayesian unfolding has indeed been presented in Ref. [69]. On our side, we have investigated this approach by making use of those unfolding procedures implemented in the object-oriented ROOT analysis framework [70]. It is well known that unfolding by straightforward inversion of the detector response matrix is mostly not successful, in particular if the matrix is generated by Monte Carlo and is hence affected by limited event statistics. The simulated proton response matrices shown in Fig. 12 clearly display the inevitable signs of resulting inaccuracies. Such a matrix is generally ill conditioned and its quasisingularity leads to unstable or even plainly unphysical results. Various techniques to solve ill-behaved equation sets have been proposed and are widely discussed in the literature: for example, Bayesian unfolding [71], singular value decomposition (SVD) [72], matrix regularization schemes [73], and Wiener filtering [74].

In our simulation study, we have investigated Tikhonov-Miller regularization and, for comparison, also unfolding with SVD. In both cases, the aim is to solve an overdetermined system of equations $\mathbf{A} \cdot \mathbf{x} = \mathbf{y}$ with a robust least-squares procedure, where \mathbf{A} is the response matrix, \mathbf{x} is the unknown input vector, and \mathbf{y} is the measured output vector. In our context, \mathbf{x} corresponds to the true particle number distribution and \mathbf{y}

⁹Note that the finite momentum resolution of the detector also leads to small cross-boundary effects, visible, e.g., in Fig. 12 for peripheral collisions: $N_{\text{det}} > 0$ although $N_{\text{in}} = 0$.

to the actually measured distribution. In an overdetermined system, the dimension of \mathbf{y} is larger than the dimension of \mathbf{x} and the solution will only be approximate. Solving such a system in a least-squares sense is then equivalent to finding the minimum of the functional $\chi^2 = |\mathbf{A} \cdot \mathbf{x} - \mathbf{y}|^2$. To achieve a more robust solution, a Tikhonov regularization term [73] can be added to this functional: $\chi^2 = |\mathbf{A} \cdot \mathbf{x} - \mathbf{y}|^2 + \lambda \mathbf{x} \cdot \mathbf{H} \cdot \mathbf{x}$, where λ is a Lagrange multiplier controlling the strength of the regularization and \mathbf{H} is a square matrix built from first-order or higher order finite differences of \mathbf{x} . The basic idea of Tikhonov is that the additional quadratic term serves as a constraint that dampens instabilities in the solution \mathbf{x} . A typical choice for \mathbf{H} is to use second-order finite differences in x which favors minimum overall curvature of the vector \mathbf{x} and suppresses higher order oscillations. The optimal regularization strength is usually found by a λ scan and the ROOT implementation¹⁰ provides two different methods to do so: the L -curve scan and the minimization of global correlation coefficients.

We have furthermore explored an unfolding method based on singular value decomposition [72], made available as well in ROOT.¹¹ The starting point of SVD unfolding is to write the response matrix \mathbf{A} as a product $\mathbf{A} = \mathbf{U} \cdot \mathbf{S} \cdot \mathbf{V}^T$, where \mathbf{U} and \mathbf{V} are orthonormal matrices, and \mathbf{S} is a diagonal matrix the elements s_i of which are the singular values of matrix \mathbf{A} . All $s_i \geq 0$ and, no matter how ill conditioned \mathbf{A} is, this decomposition can always be done. For one, SVD gives us a clear diagnosis of the degree of singularity of the response matrix and, arranging the singular values in decreasing order, it allows us to cure instabilities by truncation, that is by removing all terms with s_i smaller than a given threshold value s_{thr} . The solution \mathbf{x} of the least-squares problem can be written as a linear combination of columns of matrix \mathbf{V}

$$\mathbf{x} = \sum_i \left(\frac{\mathbf{U}^{(i)} \cdot \mathbf{y}}{s_i} \right) \mathbf{V}^{(i)},$$

with the summation going over all i for which $s_i \geq s_{\text{thr}}$. The threshold value s_{thr} can be determined using statistical significance arguments (details are given in Ref. [72]). Note that SVD can also be combined with a regularization, enforcing, e.g., positiveness of the solution or minimum curvature. Further below we show how well these unfolding methods fare in our simulations.

C. Moment expansion method

For completeness, we would like to mention yet another approach to the efficiency correction of distribution moments, namely the recently proposed method of moment expansion based on the detector response matrix [75]. Arguing that in most cases the true particle number distributions are not really needed but typically only their cumulants, the authors of Ref. [75] proposed to bypass the unfolding altogether and instead establish a direct formal relation between the measured moments m_n (or cumulants k_n) and the true moments

M_n (or cumulants K_n). Indeed, the relevant information to do so is encoded in the response matrix \mathbf{A} , more specifically in its column-wise moments which can be used to expand the observed m_n in terms of the true M_n . Depending on the efficiency model used (e.g., binomial, hypergeometric, β -binomial), this expansion is closed and, by solving the resulting system of equations $\mathbf{m} = \mathcal{A} \cdot \mathbf{M}$, the M_n are expressed in terms of the m_n . Note that the moment matrix \mathcal{A} has a much lower dimension than the response matrix \mathbf{A} itself, typically 5^2 – 10^2 versus 50^2 – 100^2 , which greatly eases its inversion. For efficiency models that do not lead to a closed form, for example, models where the efficiency depends in a nontrivial way on particle multiplicity, the expansion must be truncated at some order n_{max} to be amenable to a solution. In that case, one must study the inversion as a function of n_{max} to control the stability of the result obtained. The effect of the truncation on the moments retrieved with the expansion method is exemplified in Fig. 13 for the first four moments of a simulated proton distribution. The solution stabilizes on a plateau at $n_{\text{max}} \simeq 10$, meaning that the expansion can be safely truncated at this value of n . However, note that in this analysis based on the simulated proton response matrix (the one used also in the unfolding investigations) numerical instabilities start to set in for $n_{\text{max}} > 20$.

Unfolding and expansion methods use as input a response matrix typically produced by Monte Carlo with the help of a given event generator. However, as often pointed out (see, e.g., Refs. [75,76]), sufficiently large statistics and a proper choice of the simulation input are of importance. The input model can have an influence on the resulting response and it is therefore mandatory to carefully check its validity, not only in the region of phase space covered by the detector acceptance, but also beyond because of the inherent migration of yield from the latter to the former.

D. Validation with IQMD transport events

In an extensive Monte Carlo investigation, we have validated and compared the various presented efficiency correction schemes. As stated above, we have implemented the full HADES setup in GEANT3 and have run high-statistics simulations with as input 10^8 IQMD + MST clustered Au + Au events in the impact parameter range $b = 0$ – 10 fm. This range covered roughly the centralities accepted by the PT3 trigger,¹² namely the 0–43% most central events (see Ref. [38] for details). With reconstructed and identified proton tracks, we histogrammed the multiplicity of detected protons for various centrality and phase-space bins. Applying efficiency corrections to these distributions, we obtained the corresponding corrected proton multiplicity distributions as well as their corrected moments. Finally, making use of the event generator information, we also have the truth, i.e., the *a priori* proton distributions. Results obtained with the different correction procedures are compared in Fig. 14, which displays

¹⁰ROOT class TUnfold.

¹¹Implemented in ROOT class TSVDUnfold.

¹²Already in the model calculation, a given impact parameter leads to a distribution of participant nucleons and further smearing in the actual centrality observable.

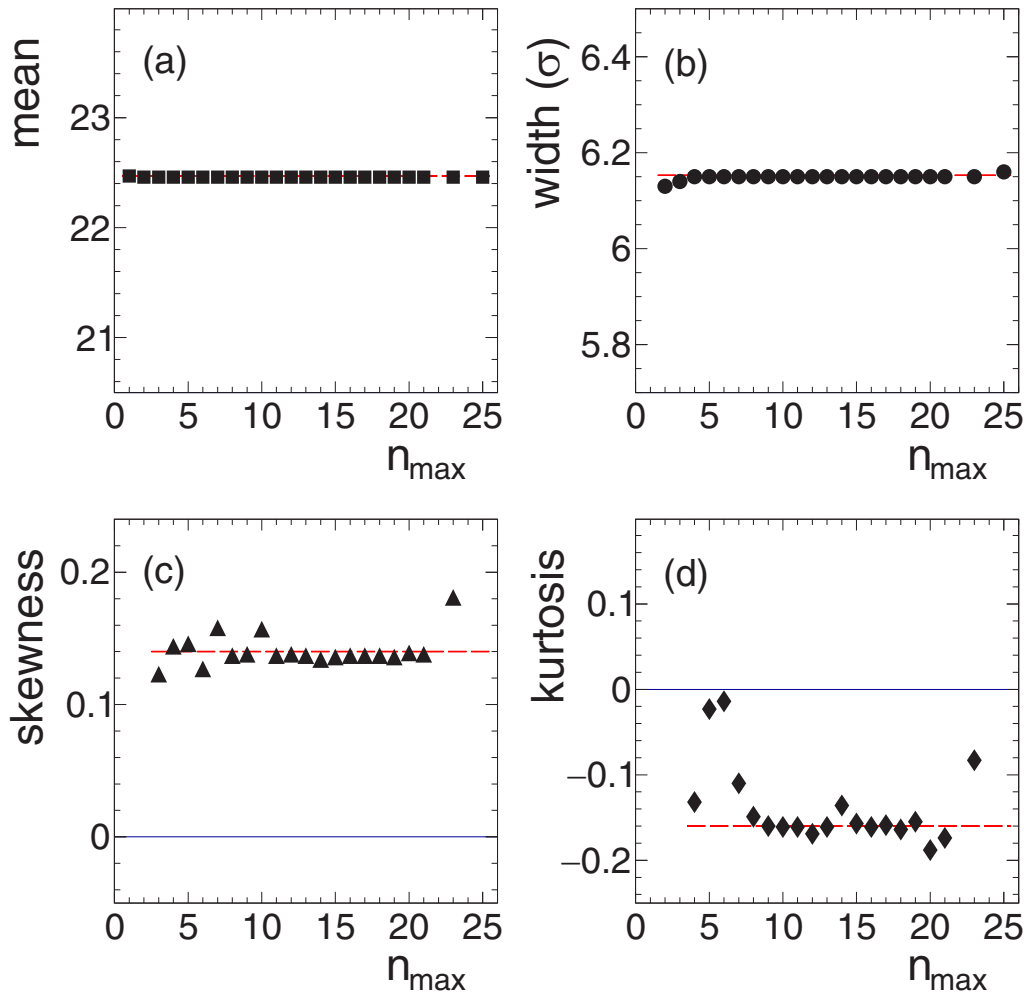


FIG. 13. Moment expansion technique applied to proton distributions from IQMD events (0–10% most central, $y \in y_0 \pm 0.2$). Shown is the dependence of the corrected moments on the truncation order n_{\max} of the moment matrix \mathcal{A} . The plateau region ($n_{\max} \geq 10$), corresponding to stable behavior, is close to the true IQMD values, namely $\langle N_p \rangle = 22.5$ (a), $\sigma = 6.15$ (b), skewness $\equiv \gamma_1 = 0.14$ (c), and kurtosis $\equiv \gamma_2 = -0.16$ (d), indicated by red dashed lines.

the respective efficiency-corrected mean, width (σ), skewness (γ_1), and kurtosis (γ_2) for protons emitted into the $y \in y_0 \pm 0.2$ and $0.4 \leq p_t \leq 1.6$ GeV/ c phase space, as a function of the mean number of participant nucleons $\langle N_{\text{part}} \rangle$.¹³ Shown are the true IQMD moments (dashed lines) and results from various correction schemes: constant efficiency, occupancy-dependent efficiency, unfolding, moment expansion, and, for comparison, also the “occupancy” model (see Appendix A) directly adjusted to the IQMD truth. It is clearly visible that by using a constant efficiency (green full circles), i.e., an efficiency independent of track density, the correct moments are not retrieved. The occupancy model (pink triangles), while giving at least a fair description for the most peripheral centralities, is overall not satisfying. On the other hand, the three correction methods discussed in detail above—either

applying an event-by-event correction or unfolding¹⁴ the measured proton distribution or using a moment expansion—all succeed in producing a result that agrees with the truth within given error bars. Besides the statistical errors due to the finite event samples simulated, also systematic uncertainties occur caused, for example, by different choices of the fit function used to model the effect of occupancy on the efficiency or of the optimal regularization applied in the unfolding; these systematic errors are indicated in Fig. 14 as shaded bands ($\pm 1\%$ for the mean, $\pm 2\%$ for the width, ± 0.02 for γ_1 , and ± 0.03 for γ_2). Figure 15 shows the same investigation done for protons emitted into a larger phase-space bin, namely $y \in y_0 \pm 0.5$. Again, the agreement with IQMD truth of the three favored methods is very satisfactory. The constant efficiency correction and the occupancy model fail, however, and are therefore omitted from the figure. From these simulation studies, we conclude that small point-to-point deviations between

¹³ N_{part} is defined as the number of nucleons in the overlap volume of the two colliding nuclei.

¹⁴SVD and Tikhonov regularized unfolding give comparable results within statistical errors.

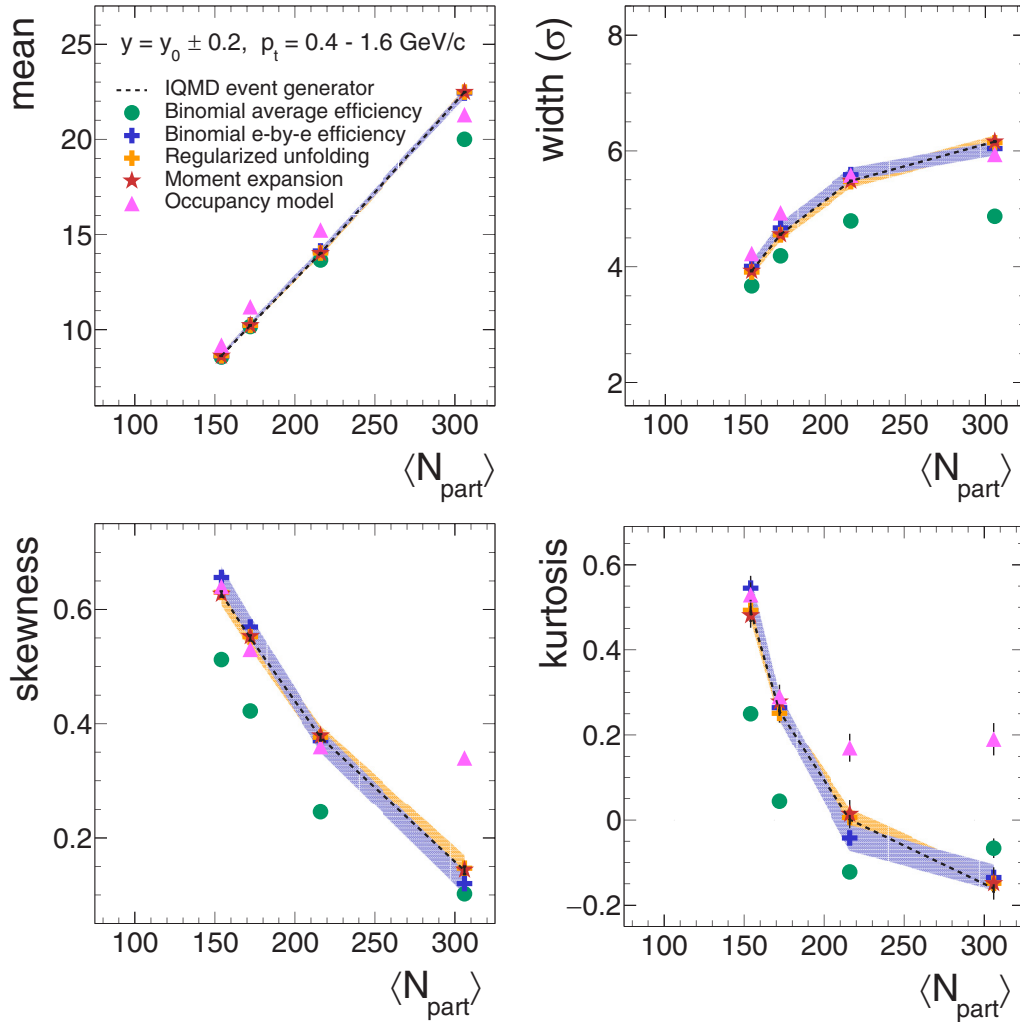


FIG. 14. Comparison of various efficiency correction methods applied to a simulation using IQMD events and selecting protons within $y \in y_0 \pm 0.2$. Plotted are the corrected proton number mean (a), width (b), skewness (c), and kurtosis (d) as a function of $\langle N_{\text{part}} \rangle$. Error bars are statistical and colored shaded bands correspond to systematic errors of the correction technique: blue for the binomial event-by-event correction, and orange for unfolding, respectively. The IQMD truth is shown as black dashed lines.

methods do exist but no evident systematic trend is apparent and no clear preference for either of the three correction schemes emerges. However, applying the efficiency corrections to our Au + Au data, the occupancy-dependent scheme turned out to become our favorite: This was motivated, first, by its ease of implementation within the event analysis loop and, second, by the fact that both unfolding and moment expansion are more sensitive to the particular choice of event generator used to produce the response matrices. In the end, we treated differences between the correction methods as a contribution to our total systematic error (see Sec. VI).

IV. VOLUME CORRECTIONS

In heavy-ion collision experiments, the centrality determination can be based on various observable quantities, like the number of hits or tracks in the detector, the total energy measured or the ratio of transverse to longitudinal energies, or the sum of charges at forward angles. The only requirement for any such observable to serve as proxy for centrality is that

it be a monotonic function of the impact parameter b , which itself is not directly measurable. In addition, as observed quantities are obtained with finite resolution only, any cut meant to restrict centrality to a particular value can do so only with a limited selectivity. This means that in all cases a finite range of impact parameters will be selected, resulting in a distribution of the reaction volume and of the corresponding number of participant nucleons N_{part} . As particle yields typically scale with some power of N_{part} , their number distributions will be affected as well and will therefore depend on the volume (or N_{part}) fluctuations of a given centrality cut. This effect has been recognized and discussed in Ref. [42], where also centrality bin width corrections (CBWC) have been proposed as a possible remedy. The idea of CBWC is to compute yield-weighted averages of distribution moments over a number of narrow subdivisions of the given wider centrality selection. This way the larger statistics of a wide selection could be benefited while palliating the noxious effects of its increased volume fluctuations. This procedure is indeed useful, but only when the centrality resolution of the observable is narrower

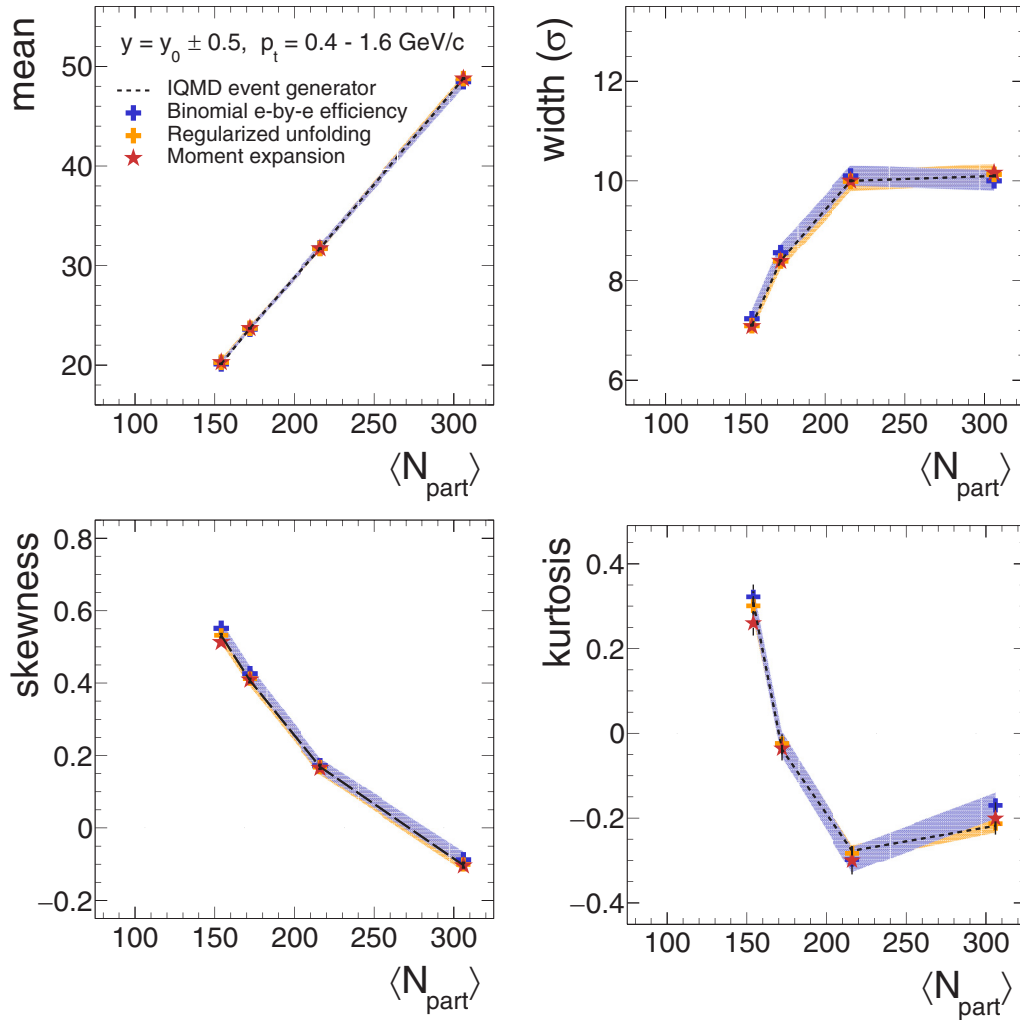


FIG. 15. Same as Fig. 14 but for protons within a rapidity bin of $y \in y_0 \pm 0.5$. Note that only the most promising techniques are shown here (see text).

than the width of the selection cut. At low beam energies, where the hit and particle multiplicities tend to be small, the achievable centrality resolution is often quite limited such that the CBWC method fails.

A more formal study of the effect of volume fluctuations on the particle number cumulants has been done in Ref. [77] and, more recently, in Ref. [78] where also a simulation study of the situation at the ALICE and STAR experiments is presented. In both publications, the authors start from the assumption that particle production scales with the reaction volume V [77], that is, the number of wounded nucleons N_w [78], such that all particle number cumulants K_n are proportional to V (or N_w); this behavior corresponds to independent particle production. Introducing reduced particle number cumulants $\kappa_n = K_n/V$ and characterizing the volume fluctuations by volume cumulants V_l , they arrived at a general expression for the volume-affected reduced cumulants

$$\tilde{\kappa}_n = \sum_{l=1}^n v_l B_{n,l}(\kappa_1, \kappa_2, \dots, \kappa_{n-l+1}), \quad (6)$$

where $v_l = V_l/V$ are reduced volume cumulants¹⁵ and $B_{n,l}$ are Bell polynomials [79]. Then, if all volume cumulants up to order n are known, the κ_n can be retrieved from the $\tilde{\kappa}_n$ by solving the system of Eqs. (6) recursively. Up to fourth order, this gives

$$\begin{aligned} \kappa_1 &= \tilde{\kappa}_1, \\ \kappa_2 &= \tilde{\kappa}_2 - \kappa_1^2 v_2, \\ \kappa_3 &= \tilde{\kappa}_3 - 3\kappa_1 \kappa_2 v_2 - \kappa_1^3 v_3, \\ \kappa_4 &= \tilde{\kappa}_4 - (4\kappa_1 \kappa_3 + 3\kappa_2^2) v_2 - 6\kappa_1^2 \kappa_2 v_3 - \kappa_1^4 v_4. \end{aligned} \quad (7)$$

With these equations, the observed cumulants can be corrected for the volume contributions resulting from the spread of the applied centrality selection. The corresponding volume distribution must be known, of course, either from a model calculation or, with the help of a procedure to be defined, from the data itself. As proposed in Ref. [78], for a more practical measure of volume one could use the number of wounded nucleons N_w or, at low bombarding energy, rather

¹⁵With $V_1 = V$ and $v_1 = 1$.

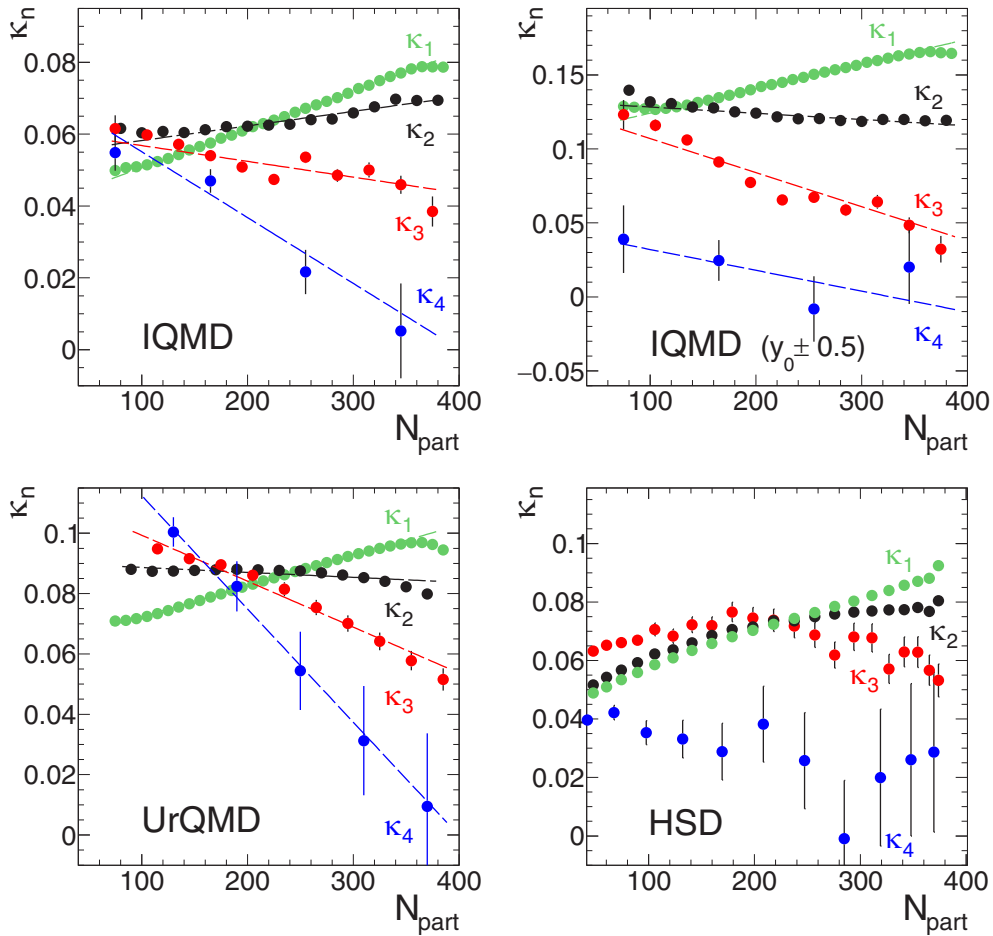


FIG. 16. Reduced proton cumulants κ_n as a function of N_{part} in four different transport calculations done with the IQMD, UrQMD, and HSD models respectively. The phase space chosen here was $y \in y_0 \pm 0.2$ (or $y \in y_0 \pm 0.5$) and $0.4 \leq p_t \leq 1.6$ GeV/c for IQMD, respectively $y \in y_0 \pm 0.2$ and $0.4 \leq p_t \leq 1.6$ GeV/c for UrQMD and HSD. Dashed lines are linear fits of function $\kappa(N_{\text{part}}) = \kappa_0 + \kappa' N_{\text{part}}$ to some of the presented reduced cumulants.

the number of participating nucleons N_{part} . The open question, however, is to what extent the assumed scaling with volume of the cumulants, which is at the basis of Eq (6), can be considered valid. The authors of Ref. [77] argued that, while this is indeed a reasonable approximation in ultrarelativistic heavy-ion collisions probing the low- μ_B , high- T region of the phase diagram, caution should be applied in the high- μ_B regime relevant for CEP searches. To find some guidance, we have investigated the respective behavior of transport codes, namely IQMD, UrQMD, and also HSD (version 711n) [80] run for the $\sqrt{s_{NN}} = 2.4$ GeV Au + Au reaction; i.e., we have analyzed their true proton number cumulants as a function of N_{part} within various phase-space bins. Figure 16 shows examples of such calculations together with fits of the linear function $\kappa(N_{\text{part}}) = \kappa_0 + \kappa' N_{\text{part}}$ to some of the simulation points.¹⁶ It is obvious from these plots that all three transport models strongly violate the assumption of constancy of κ_n

versus N_{part} by revealing a linear and, in some cases (e.g., for HSD), even a quadratic dependence on N_{part} . A systematic study also reveals a high degree of variability with respect to the particular bin chosen in $y - p_t$ phase space. The models differ, however, in the details of their rendering of the complex dependency of κ_n on centrality.

Evidently, the assumption of constancy of κ_n has to be abandoned and at least a linear term or, better, linear plus quadratic terms have to be taken into account when calculating the contributions of volume fluctuations. Along the lines presented in Ref. [77], we have extended the derivation of Eq. (6) by replacing the constant ansatz $\kappa_n(V) = \kappa_n$ with a second-order Taylor expansion of $\kappa_n(V)$ around the mean $\langle V \rangle$ of the volume distribution

$$\kappa_n(V) = \kappa_n + \kappa'_n (V - \langle V \rangle) + \kappa''_n (V - \langle V \rangle)^2, \quad (8)$$

where the κ_n are the leading constant terms, κ'_n are slopes, and κ''_n are curvatures, all of which can depend on rapidity and transverse momentum. With this ansatz, a more complete set of volume terms contributing to the reduced cumulants $\tilde{\kappa}_n$ has been derived. Using slopes only (i.e., $\kappa''_n = 0$), the following

¹⁶The N_{part} bin width used in these calculations (10 for IQMD and UrQMD, 20 for HSD) was fine enough to keep volume-fluctuation effects small.

TABLE II. Number of volume-fluctuation terms contributing to the observed reduced cumulants $\tilde{\kappa}_n$. Column L (leading terms) corresponds to Eq. (6), L + NL (including slopes of the N_{part} dependence) corresponds to Eq. (9), and L + NL + N2L (with slopes and curvatures) corresponds to Eq. (10).

$\tilde{\kappa}$	L	L + NL	L + NL + N2L
$\tilde{\kappa}_1$	0	1	3
$\tilde{\kappa}_2$	1	8	26
$\tilde{\kappa}_3$	2	28	128
$\tilde{\kappa}_4$	4	84	527

relations were found for $n = 1, 2, 3$, and 4:

$$\begin{aligned}
 \tilde{\kappa}_1 &= \kappa_1 + v_2 \kappa'_1, \\
 \tilde{\kappa}_2 &= \kappa_2 + \kappa_1^2 v_2 + \kappa_2' v_2 + 2\kappa_1 \kappa_1' V_2 + 2\kappa_1 \kappa_1' v_3 \\
 &\quad + 2\kappa_1'^2 v_2 V_2 + \kappa_1'^2 V_1 V_2 + 2\kappa_1'^2 V_3 + \kappa_1'^2 v_4, \\
 \tilde{\kappa}_3 &= \kappa_3 + \kappa_1^3 v_3 + 3\kappa_1 \kappa_2 v_2 + 3(\kappa_1 \kappa_2' + \kappa_1' \kappa_2) v_3 \\
 &\quad + 6\kappa_1' (\kappa_1^2 + \kappa_2') v_2 V_2 + 3\kappa_1' (\kappa_1^2 + 2\kappa_2') V_3 \\
 &\quad + 3\kappa_1' (\kappa_1^2 + \kappa_2') v_4 + 12\kappa_1 \kappa_1'^2 V_2^2 + 3\kappa_1 \kappa_1'^2 V_1 V_3 \\
 &\quad + 24\kappa_1 \kappa_1'^2 v_2 V_3 + 6\kappa_1 \kappa_1'^2 V_4 + 3\kappa_1 \kappa_1'^2 v_5 + \kappa_3' v_2 \\
 &\quad + 3(\kappa_1 \kappa_2' + \kappa_1' \kappa_2) V_2 + 8\kappa_1^3 v_2 V_2^2 + 6\kappa_1^3 V_1 V_2^2 \\
 &\quad + 10\kappa_1^3 v_3 V_3 + \kappa_1^3 V_1^2 V_3 + 24V_2 V_3 \kappa_1^3 + 3\kappa_1^3 V_1 V_4 \\
 &\quad + 12\kappa_1^3 v_2 V_4 + 3\kappa_1^3 V_5 + \kappa_1^3 v_6 + 3\kappa_1' \kappa_2' V_1 V_2, \\
 \tilde{\kappa}_4 &= \kappa_4 + \kappa_1^4 v_4 + 6\kappa_1^2 \kappa_2 v_3 + (4\kappa_1 \kappa_3 + 3\kappa_2^2) v_2 \dots \dots \quad (9)
 \end{aligned}$$

Because of its length, the cumulant of order $n = 4$ is fully listed in Appendix B, Eq. (B4). Compared to Eq. (6), many additional terms that all depend on the slopes appear, including terms involving volume cumulants up to order $2n$, that is, for $\tilde{\kappa}_4$ up to order 8. In a somewhat colloquial manner, we designate the slope-related corrections by NLO, i.e., next to leading order, and the curvature affected terms (see below) by N2LO, i.e., next to next to leading order. For the higher orders, the number of terms quickly rises and the formulas become cumbersome to derive by hand; we have instead used a symbolic computation program¹⁷ to generate them as well as the corresponding C code needed for their numerical evaluation. Evidently, the relations derived with all slopes and curvatures included are even lengthier (see Table II) and they require volume cumulants up to order $3n$. The C code can be provided on request and, for illustration only, we list here the first two N2LO cumulants:

$$\begin{aligned}
 \tilde{\kappa}_1 &= \kappa_1 + v_2 \kappa'_1 + (V_2 + v_3) \kappa_1'', \\
 \tilde{\kappa}_2 &= \kappa_2 + \kappa_1^2 v_2 + \kappa_2' v_2 + 2\kappa_1 \kappa_1' V_2 + 2\kappa_1 \kappa_1' v_3 \\
 &\quad + 2\kappa_1'^2 v_2 V_2 + \kappa_1'^2 V_1 V_2 + 2\kappa_1'^2 V_3 + \kappa_1'^2 v_4 \\
 &\quad + 6\kappa_1 \kappa_1'' v_2 V_2 + 2\kappa_1 \kappa_1'' (V_3 + v_4) + \kappa_2'' (V_2 + v_3) \\
 &\quad + 10\kappa_1' \kappa_1'' V_2^2 + 18\kappa_1' \kappa_1'' v_3 V_2 + 2\kappa_1' \kappa_1'' V_1 V_3
 \end{aligned}$$

$$\begin{aligned}
 &+ 4\kappa_1' \kappa_1'' V_4 + 2\kappa_1' \kappa_1'' v_5 + 15\kappa_1'^2 v_2 V_2^2 \\
 &+ 2\kappa_1'^2 V_1 V_2^2 + 18\kappa_1'^2 V_2 V_3 + 15\kappa_1'^2 v_4 V_2 \\
 &+ 9\kappa_1'^2 v_3 V_3 + \kappa_1'^2 V_1 V_4 + 2\kappa_1'^2 V_5 + \kappa_1'^2 v_6. \quad (10)
 \end{aligned}$$

Despite the large number of contributing terms, one has to keep in mind that these expressions are just polynomials which can be easily evaluated for given values of κ_n , κ_n' , κ_n'' , and v_l , and they can be adjusted to simulated or real data to extract the cumulants of interest. Doing such fits to proton cumulants obtained with transport models, we find that typically $\kappa_n \gg \kappa_n' \gg \kappa_n''$ and consequently most of the higher order volume terms turn out to be very small. This is also confirmed by fits of Eq. (10) to our data, as exemplified in Fig. 17 which shows the rapid drop over nearly seven orders of magnitude of the contributing volume terms with increasing order of v_l . We conclude that in practice it is sufficient to consider terms with v_l up to order $l = 5$ or 6 at most, i.e., the full gamut of the v_l up to $l = 8$ (NLO) or even $l = 12$ (N2LO) will most likely never be required.

V. CENTRALITY SELECTION AND N_{part} DISTRIBUTIONS

In order to apply volume corrections to particle-number cumulants measured within a given centrality selection, it is mandatory to know the corresponding N_{part} distribution or at least its cumulants up to sufficiently high order. In simulations, the impact parameter b is known event by event and the corresponding number of participants can be determined from the geometric overlap or, better, with the help of a more involved Glauber model. In the data, however, b and N_{part} are not directly observable; we must find a proxy for N_{part} , e.g., the number of observed hits N_{hit} or of reconstructed tracks N_{trk} , to quantify the volume effects. The very strong and nearly linear correlation between N_{hit} and the underlying N_{part} is illustrated in Fig. 18 which shows a simulation done with the IQMD transport model. Hence, a first approach to arrive at the volume cumulants V_l , required by Eqs. (6), (9), and (10), could be to just use the cumulants of the observed N_{hit} distribution. Yet, the two quantities do not trivially relate to each other: First, particle production per participant nucleon is a random process; and second, finite detector acceptance and efficiency make the observation process random too. Consequently, any given N_{part} results in a spread of the observed number of hits, where the relation $N_{\text{hit}}(N_{\text{part}})$ can be approximated by a negative binomial distribution [38]. Because of this spread, simply using N_{hit} as a direct proxy for N_{part} will lead to an overestimation of V_2 and will generally result in wrong higher order cumulants. Of course, the same arguments also speak against using N_{trk} as proxy for N_{part} .

There is in fact yet another, more subtle effect that needs to be taken into account in the determination of the V_l , namely the correlations between N_{prot} and the centrality measure used, N_{hit} , N_{trk} , or ΣQ_{FW} . A recent simulation study [81] done with $\sqrt{s_{NN}} = 200$ GeV UrQMD events concluded that the correlations between the proton number and the centrality defining multiplicities do affect the volume-fluctuation correction. A qualitative argument for this phenomenon is the following: A

¹⁷Wolfram MATHEMATICA.

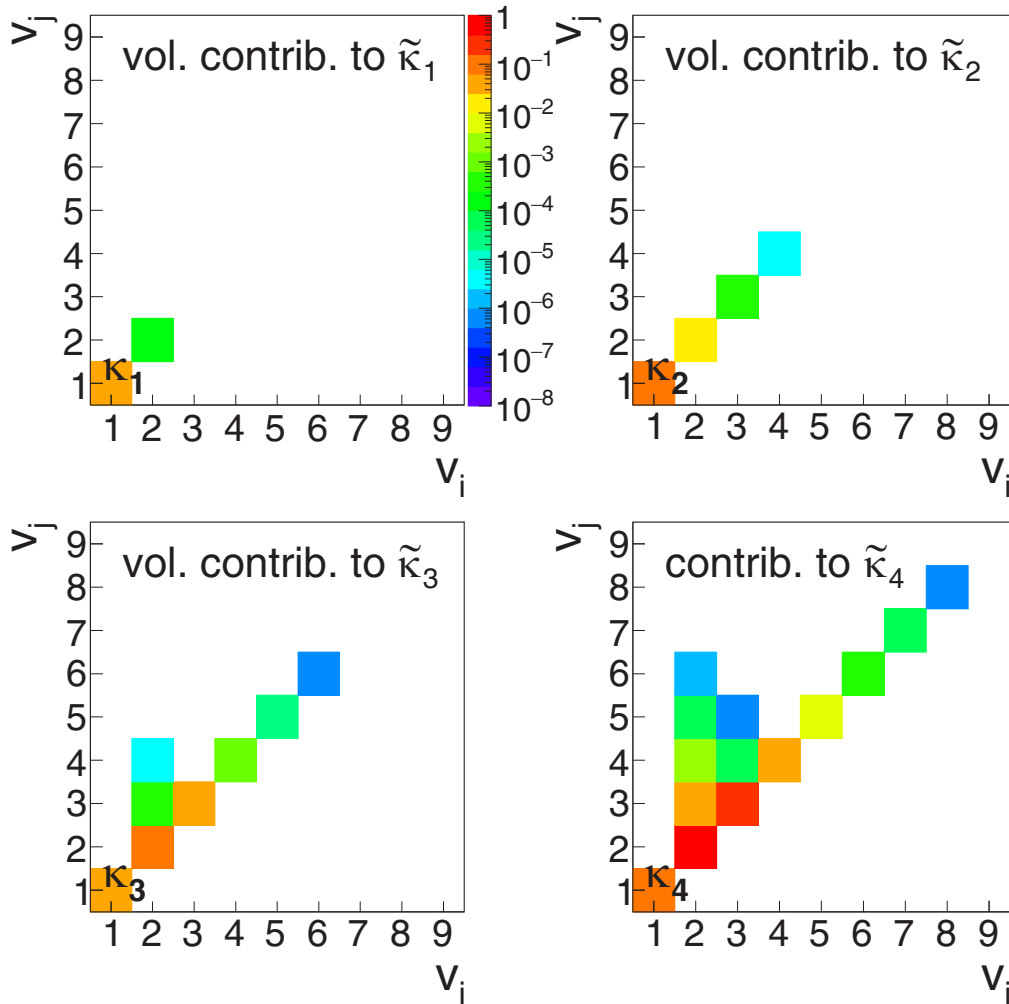


FIG. 17. Illustration of the magnitude of NLO + N2LO volume-fluctuation terms contributing to the observed reduced proton number cumulants $\tilde{\kappa}_n$ with $n = 1, 2, 3,$ and 4 . The magnitude of the terms decreases quickly with increasing order of v_i ; low-order diagonal terms are dominant and off-diagonal terms, depending on a product $v_i \cdot v_j$, fall off even faster. The corrections shown were determined for a selection of the 0–10% most central Au + Au collisions measured in HADES (see Sec. V below).

centrality selection realized by applying cuts on the number of observed hits, $N_{\min} \leq N_{\text{hit}} \leq N_{\max}$, constrains not only the mean number of hits $\langle N_{\text{hit}} \rangle$ but, because N_{hit} and N_{prot} are strongly correlated, also the corresponding mean number of protons. This cut will therefore tend to curtail large excursions of N_{prot} from its mean value $\langle N_{\text{prot}} \rangle$, leading to a reduction of its variance and generally affecting the higher order proton number cumulants in a nontrivial way. At the low bombarding energies where HADES operates, protons are the dominant particle species and they contribute most of the hits and tracks, causing correlations to be particularly pronounced. This appears also from the transport model simulations (IQMD and UrQMD) displayed in Fig. 19, where the linear correlation coefficients ρ between N_{prot} and, respectively, N_{hit} , N_{trk} , and ΣQ_{FW} are plotted against impact parameter b . Both models show strong positive correlations for N_{hit} and N_{trk} , and negative, but much weaker correlations for ΣQ_{FW} . Ideally, one would want to incorporate correlations between the proton number and the centrality-defining observable into a more comprehensive volume-fluctuation formalism expressed, if

possible, as a function of the experimentally accessible relevant correlation coefficient $\rho(N_{\text{prot}}, N_{\text{hit}})$, $\rho(N_{\text{prot}}, N_{\text{trk}})$, or $\rho(N_{\text{prot}}, \Sigma Q_{\text{FW}})$. Unfortunately, such a complete model is not yet at hand, and we have hence taken the pragmatic approach to (1) use the centrality selector with lowest correlations and (2) modify the volume cumulants based on the resulting N_{hit} distributions such as to express the correlation-affected N_{part} distributions.

In the Au + Au data presented here, the observed correlation coefficient $\rho(N_{\text{prot}}, \Sigma Q_{\text{FW}})$ was found to be negative as in the transport simulations but of somewhat larger magnitude, 0.15–0.25. However, these values also include a part caused by the global volume fluctuations within the finite experimental centrality bins and the intrinsic correlations of the two observables might in fact be weaker. All matters considered, the observable ΣQ_{FW} displays the smallest correlations with N_{prot} and we have hence used it as centrality selector for the proton-fluctuation analysis. We developed an *ad hoc* scheme to handle in one swipe both the blurring of the $N_{\text{part}} \rightarrow N_{\text{hit}}$ mapping and the correlation-induced modifications of

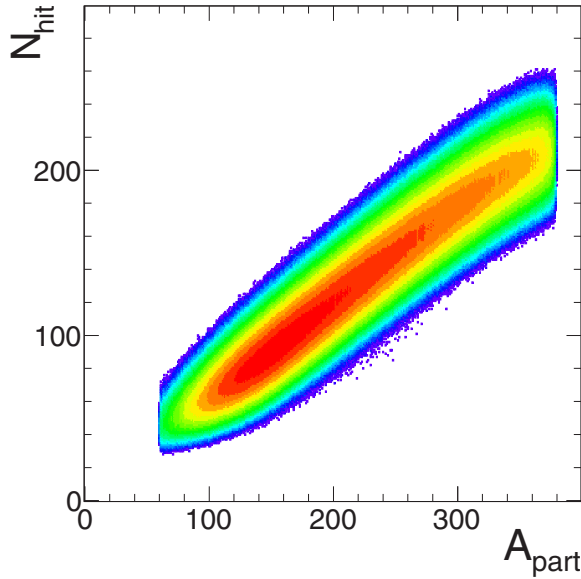


FIG. 18. Correlation between the total number of hits N_{hit} in the HADES time-of-flight detectors and the number of participants N_{part} in 1.23A GeV Au + Au events simulated with the IQMD transport code for impact parameters in the range of 0–10 fm.

the volume cumulants v_l . The core idea is to introduce at every order ($l = 2, 3, \dots, l_{\text{max}}$) a pair of modifiers, f_l and d_l , and substitute v_l in the cumulant expressions, i.e., Eqs. (9) and (10), with $v_l^{\text{mod}} = f_l \times v_l + d_l$; each volume cumulant is eventually adjusted by applying an appropriate scaling factor f_l as well as a modifying cumulant d_l . This transformation yields modified volume cumulants once the f_l and d_l are properly fixed. For our analysis, we have determined these parameters in a multiorder fit of Eq. (10) to the reconstructed proton cumulants $\bar{\kappa}_n$ of a high-statistics sample of IQMD events run through the HADES detector simulation and analysis pipeline, i.e., in a situation where the true κ_n , as well as their slopes κ'_n and curvatures κ''_n were all fully known. In this procedure, the reduced volume cumulants v_l were taken from the N_{hit} distribution, with its abscissas rescaled by the factor $\langle N_{\text{part}} \rangle / \langle N_{\text{hit}} \rangle$, and using N_{part} as a proxy for the source volume, i.e., $V \equiv N_{\text{part}}$. Note that the $N_{\text{hit}} - N_{\text{prot}}$ correlations do not preclude us from using the scaled N_{hit} distribution as a proxy for the volume distribution because, in the determination of the v_l , only event-averaged quantities enter.

With the adjusted set of parameters f_l and d_l , the modified volume cumulants can be obtained and used to generate an approximation (up to some order l_{max}) of the effective, i.e., correlation-affected N_{part} distributions (see Appendix C for details). Figure 20 illustrates the procedure with simulated IQMD N_{part} distributions corresponding to four different centrality bins selected with cuts on the ΣQ_{FW} observable. The true distributions from the model (red histograms) are compared with a reconstruction (dot-dashed curves) based on their first four reduced volume cumulants v_l ($l = 1, 2, 3, 4$) and plotted as four-parameter β distributions; likewise, the approximation based on the modified reduced volume cumulants v_l^{mod} is plotted (solid curves). Although all volume cumulants

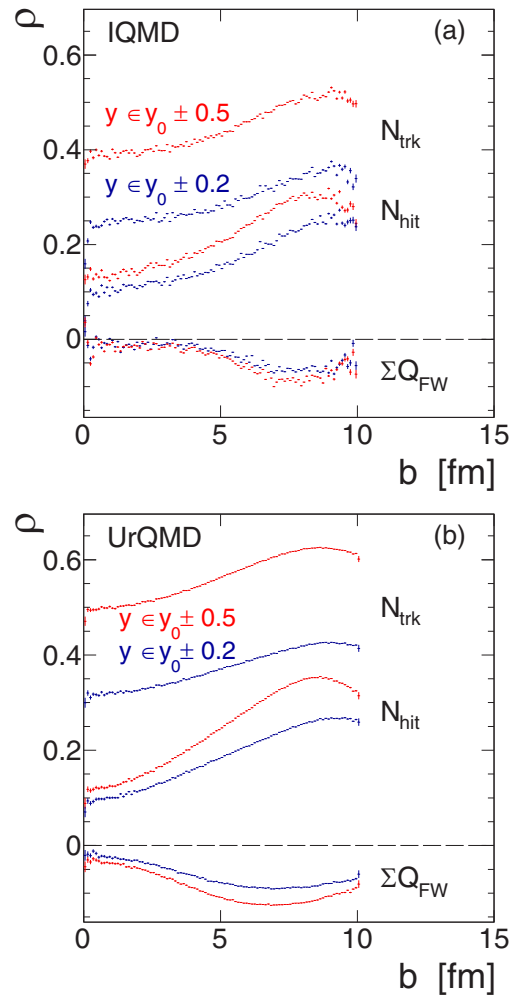


FIG. 19. Transport simulations of Au + Au events with the IQMD (a) and UrQMD (b) models showing correlations between the number of identified protons N_{prot} and the centrality defining observable $N_{\text{cen}} = N_{\text{hit}}, N_{\text{trk}}$, and ΣQ_{FW} , respectively. Pearson's linear correlation coefficient $\rho(N_{\text{prot}}, N_{\text{cen}})$ is displayed for two rapidity ranges, $y \in y_0 \pm 0.2$ (dark blue) and $y \in y_0 \pm 0.5$ (red), as a function of the impact parameter b .

up to sixth order were included in the parameter fit, the reconstructed N_{part} is plotted as a four-parameter distribution. This approximation—used here for display only—evidently misses some of the more wobbly features of the true distribution, which are best visible in the 0–10% and 10–20% centrality bins. Most notable, however, are the changes caused by correlations, leading to a consistent reduction in width of the effective N_{part} distributions as compared to the model truth.

In the data, the true event-by-event number of participating nucleons is not known; however, as explained above, we can reconstruct the event-averaged N_{part} distribution from its cumulants by using a volume-cumulant transformation of the observed N_{hit} distribution. This transformation is done by applying the modifiers f_l^{sim} and d_l^{sim} , determined previously in a simulation, to the cumulants v_l of the rescaled N_{hit} distribution, namely $v_l^{\text{mod}} = f_l^{\text{sim}} \times v_l + d_l^{\text{sim}}$. To do the $N_{\text{hit}} \rightarrow N_{\text{part}}$ scaling, the mean number of participants $\langle N_{\text{part}} \rangle$

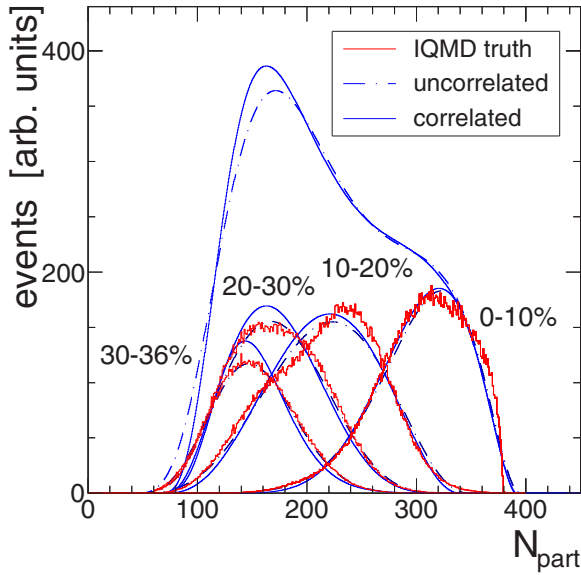


FIG. 20. N_{part} distributions of simulated IQMD events shown for four centrality selections based on the ΣQ_{FW} signal in the FWALL. IQMD truth (red histograms) is compared to reconstructions based on their first four volume cumulants, displayed as four-parameter β functions, without correlation effects (dot-dashed curves) and with correlations (solid curves). The sum curves correspond to the 0–36% most central events.

underlying the mean number of hits $\langle N_{\text{hit}} \rangle$ in a given centrality bin was taken from a Glauber fit to the experimental hit distribution [38]. As discussed above, with the modified reduced cumulants v_l^{mod} , the effective N_{part} distribution can be reconstructed up to a given order. The result of this procedure is displayed in Fig. 21 for eight 5% centrality selections based on the ΣQ_{FW} observable; the measured N_{hit} distributions are shown in Fig. 21(a) and the corresponding reconstructed N_{part} distributions in Fig. 21(b), where the latter plotted as four-parameter β functions based on either the v_l^{mod} (solid curves) or, for comparison, the plain v_l (dot-dashed curves). Note again that, in all centrality selections, using modified cumulants leads to a substantial narrowing of the reconstructed N_{part} distributions.

After having determined the reduced volume cumulants v_l^{mod} by scaling and transforming the measured N_{hit} distributions, we are finally in a position to fully remove volume-fluctuation effects from the efficiency-corrected reduced proton number cumulants $\tilde{\kappa}_n$. This is done in a combined multi-order fit of Eq. (10) to the set of measured $\tilde{\kappa}_n$ values, thereby adjusting all κ_n , κ'_n , and κ''_n at once while keeping the v_l^{mod} fixed to their simulated values. Errors arising from the correction procedure are discussed in Sec. VI, while final results obtained with the full analysis chain are presented in Sec. VII.

VI. ERROR TREATMENT

A. Statistical errors

As discussed in the previous sections, fluctuation observables must be subjected to sophisticated analysis procedures

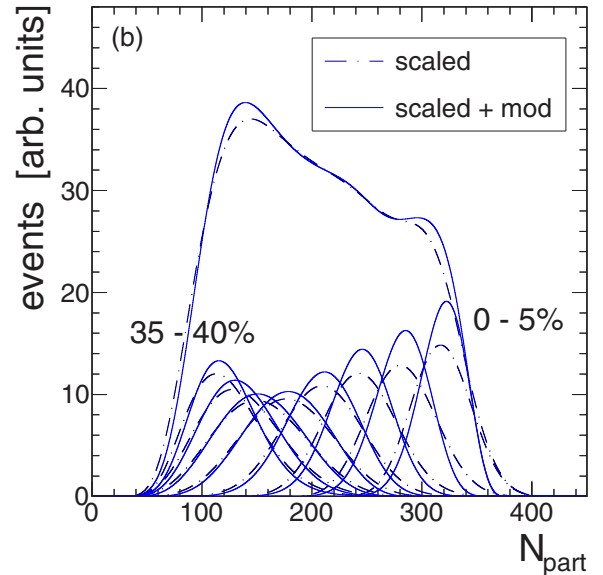
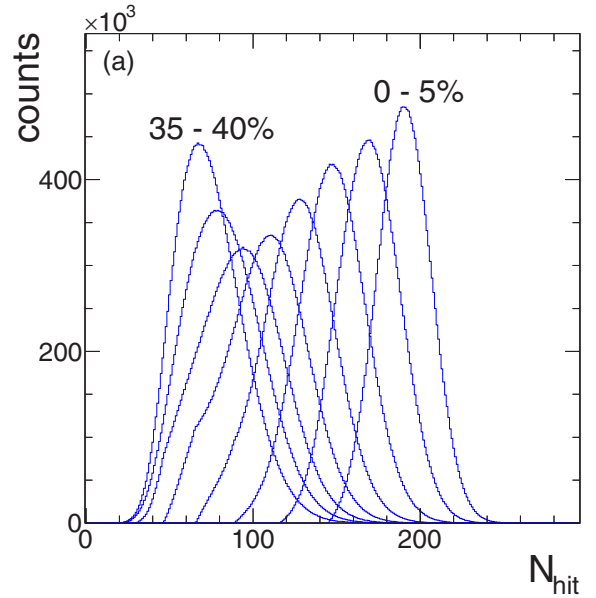


FIG. 21. (a) Measured Au + Au N_{hit} distributions of eight 5% centrality selections based on the ΣQ_{FW} signal. The latter is constrained by the 2D cut shown in Fig. 5, causing also the barely visible “knee” in the 15–20% distribution. (b) Corresponding reconstructed N_{part} distributions—plotted as four-parameter β functions—when using the rescaled and modified volume cumulants v_l^{mod} (solid curve) or the just rescaled ones v_l (dot-dashed curve). The sum curves correspond to the 40% most central events.

like efficiency correction and volume effect removal. Unfortunately, the explicit propagation of the corresponding statistical errors throughout this complex reconstruction pipeline is awkward at best [53] and, in our case, not practical at all. Instead, we have used the resampling method known as the bootstrap [57,82,83] as well as event subsampling [84] to determine statistical error bars.

The main idea of the bootstrap method is to repeatedly re-sample events with replacement from the total set of N_{ev} measured events which, by definition, are considered independent

and identically distributed (iid). For large N_{ev} , this procedure reuses on average a fraction $1 - e^{-1} \simeq 0.632$ of all events in the set. Each of our 5% centrality selections comprises $N_{ev} \approx 20$ million events and a huge number¹⁸ of nonidentical event sets can be resampled; as our main goal is to get an error estimate, a few hundred resamplings are considered sufficient in practice [57]. Every one of the resampled event sets is processed through the full analysis pipeline, allowing us to construct the distribution of each observable of interest. The histogrammed observables provide in turn estimates of their respective mean and standard deviation, that is the statistical error bar aimed for.

An alternative method to determine statistical errors is provided by subsampling. In that approach, the full set of observed events is divided into a number of equal-sized subsets which are analyzed one by one, again producing distributions of all observables with corresponding estimates of mean and standard deviation. Subsampling is much faster than resampling as it operates on smaller event sets with, however, a correspondingly larger error. In order to use the subsampling standard deviation as an estimator of the error on an observable obtained from the full data set, it has hence to be scaled by $1/\sqrt{N_{sub}}$, where N_{sub} is the number of subsamples [84]. Another important difference to resampling is that subsampling can be sensitive to long-term changes in the data properties, resulting, e.g., from instabilities of the experimental conditions affecting the detector and/or beam during the data taking. Indeed, if the subsamples correspond to consecutive time periods, the resulting error bars will not only represent fluctuations due to counting statistics but also incorporate a measure of mid- and long-term experimental changes. It is then a matter of discussion how to label these additional contributions: while random, mostly short-term instabilities may be presented as part of the statistical fluctuations, long-term drifts may be considered more akin to systematic errors. In our case, we have corrected the measured proton yields for long-term, i.e., day-by-day changes by rescaling the average number of reconstructed tracks per event to a reference value. Comparing next the standard deviations from subsampling, based on a splitting into 2-h-long data-collection periods, with the ones from resampling of the full set of events, we observe an overall increase resulting in about a doubling of the error on fourth-order moments and cumulants. As systematic effects ultimately dominate the total error on our measurements (see Sec. VII), we decided to accommodate the remaining short-term random variations in our statistical errors by using the subsampling standard deviations instead of the resampling ones.

B. Systematic uncertainties

As already argued in Sec. II, various nuisance effects can potentially influence the measured proton multiplicity distribution. They result either from a contamination by other event classes, namely pileup events or Au + C reactions, or

from background processes within valid Au + Au events, like misidentified particles, decay protons, or knockout protons. We determined upper limits on this background (listed in Table I) and simulated how the proton cumulants are affected. As within-event contributions just add particles to the event, their effect on the cumulants is of similar magnitude as the background itself, i.e., well below the 1% level. Assuming purely Poissonian processes [54] in our simulation, the estimated contributions of event classes with either larger average multiplicity (pileup) or lower (Au + C reactions) were found to induce changes of maximally 5%. And their influence would become even smaller if the relevant physics signal turned out to be of non-Poissonian nature. We conclude that in the present analysis both nuisance effect classes are inconsequential.

Systematic errors also arise at various stages of the analysis. We classify those into three types:

- (1) Type A errors are caused by a global uncertainty on the proton efficiency, arising in the track reconstruction and particle identification procedures. The estimated efficiency error of 4–5% in the phase-space bin of interest [48] results typically in about $n \times (4-5)\%$ errors on cumulants and reduced cumulants of order n .
- (2) Type B errors arise from imperfections of the cumulant correction schemes, i.e., event-by-event correction, unfolding, or moment expansion. From a systematic comparison of these methods in both simulation (see discussion of Figs. 14 and 15) and data, we find typical errors of 1.5% on K_1 , 3% on K_2 , 7.5% on K_3 , and 15% on K_4 .
- (3) Type C errors are due to an overall inaccuracy of about 8–9% on the N_{part} calibration of our centrality determination (caused by model dependencies and the limited experimental resolution [38]). This impacts the cumulants indirectly through the applied volume correction, resulting in uncertainties of order $\leq 2\%$ for K_2 , 3–6% for K_3 , and 10–30% for K_4 . Reduced cumulants are, however, affected more directly through their normalization to $\langle N_{part} \rangle$.

The factorial cumulants C_n and, to some extent, also the cumulant ratios turn out to be more robust than the K_n , showing generally a factor 2–3 smaller relative systematic error. In the results section below, we present the total systematic error, obtained as a combination of the three types A, B, and C. This was achieved by applying the efficiency and volume corrections to the respective observable of interest, K_n or C_n , while varying the detection efficiency and the volume proxy, i.e., $\langle N_{part} \rangle$, within the ranges specified above. The resulting total spread of the corrected observable was then assigned as a systematic error, thus complementing the statistical one.

VII. RESULTS

A. Cumulants and moments

Here we present the efficiency and volume-corrected proton multiplicity moments and cumulants obtained in 1.23 A GeV Au + Au collisions ($\sqrt{s_{NN}} = 2.4$ GeV). To start,

¹⁸In fact, $\binom{2N_{ev} - 1}{N_{ev}}$, i.e., approximately an astounding $10^{12000000}$.

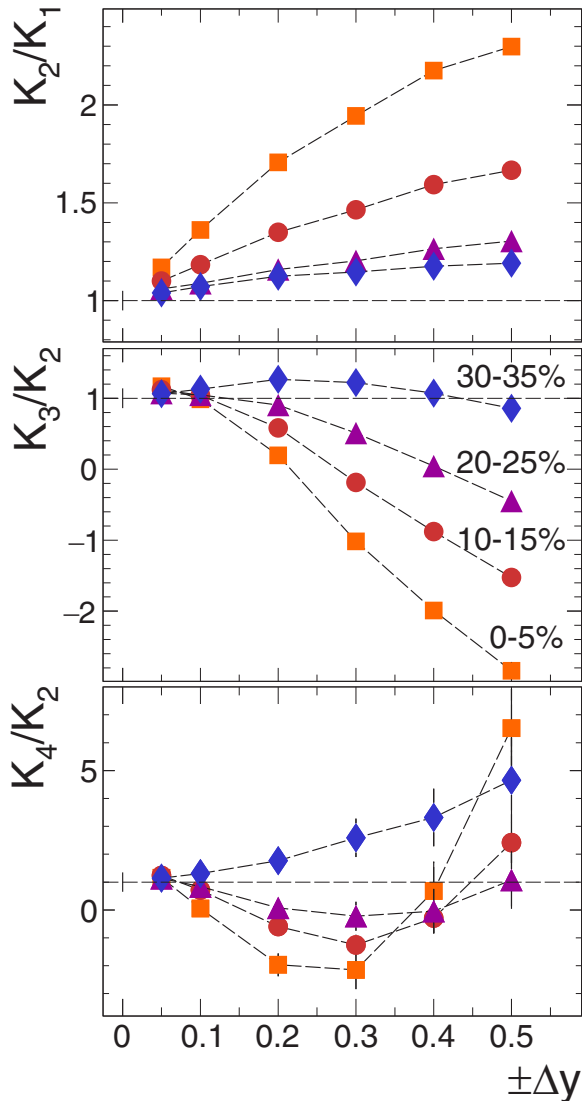


FIG. 22. Au + Au data: Efficiency and N2LO volume-corrected proton cumulant ratios plotted as a function of the width of the rapidity bin defined by $y \in y_0 \pm \Delta y$ and $0.4 \leq p_t \leq 1.6$ GeV/c. Shown are $\omega = K_2/K_1$ (top), $\gamma_1 \times \sigma = K_3/K_2$ (middle), and $\gamma_2 \times \sigma^2 = K_4/K_2$ (bottom) for various 5% centrality selections. Error bars are statistical only, and dashed lines connect the data points belonging to a given centrality. With decreasing Δy , all ratios tend toward unity (indicated also by a horizontal line); i.e., they approach the Poisson limit where $K_1 = K_2 = K_3 = K_4$.

we show in Fig. 22 for a few centrality selections the ratios of fully corrected cumulants ($\omega = K_2/K_1$, $\gamma_1 \times \sigma = K_3/K_2$, $\gamma_2 \times \sigma^2 = K_4/K_2$, where K_n are cumulants) as a function of the width of the rapidity bin, namely $y \in y_0 \pm \Delta y$, centered at midrapidity $y_0 = 0.74$ and with $0.4 \leq p_t \leq 1.6$ GeV/c. These ratios were derived from the reduced cumulant expansions obtained by fitting one of Eqs. (9) or (10) to the efficiency-corrected and centrality-selected data points.¹⁹ In

¹⁹For very narrow phase space, the NLO and N2LO fits give very similar results.

this procedure, the modified volume cumulants V_n obtained from the experimental N_{hit} distributions, as laid out in Sec. V, were inserted while the values of the κ_n , κ'_n , and κ''_n were adjusted. Error bars shown in Fig. 22 are statistical; they were obtained with the sampling techniques discussed in Sec. VI. As phase space closes more, ever fewer correlated particles contribute and one expects their distribution to approach the Poisson limit [7] where the K_n converge, i.e., $K_n = \langle N_{\text{prot}} \rangle$ for all n . From the figure, it is apparent that the data follow indeed in all centrality selections such a behavior, with the cumulant ratios approaching unity within their statistical errors.

Turning to rapidity bites substantially larger than ± 0.1 , we found that NLO volume effects do not suffice anymore to give a good description of the observed proton cumulants, meaning that N2LO volume terms must be included. This is demonstrated in Fig. 23, which, for $y \in y_0 \pm 0.2$, compares the effect of the volume correction at successive levels of sophistication. Shown are the reduced cumulants κ_1 , κ_2 , κ_3 , and κ_4 as a function of N_{part} when using 5% centrality bins: either not volume corrected (open triangles), or with only the leading order (LO) correction of Eq. (7) applied (open circles), or with the full N2LO correction applied (full squares). To not clutter the pictures too much, the NLO corrected points are not displayed explicitly but both fit curves are shown: NLO (dashed curve) done with Eq. (9) and N2LO (solid curve) done with Eq. (10). The corresponding statistical and systematic errors were obtained with the procedures described in Sec. VI. Figure 23 illustrates that the LO scheme proposed in Refs. [77,78] removes in our case only about 50–70% of the volume fluctuations. While using instead NLO corrections does improve the description, it still does not lead to a fully satisfactory fit of the cumulants. One can see that the linear fit of κ_2 , in particular, misses the data points which definitely display a substantial curvature. When enlarging the accepted phase space further, curvature terms become even more important, as shown in Fig. 24, which compares volume-corrected reduced proton cumulants and fits in the two rapidity bins, $y \in y_0 \pm 0.2$ and $y \in y_0 \pm 0.4$. Consequently, all results presented in the following were obtained by consistently applying the full N2LO volume corrections.

Comparing furthermore the measured reduced proton cumulants of Fig. 24 with their transport calculation counterparts, as shown in Fig. 16, one can notice a qualitative agreement for the $y \in y_0 \pm 0.2$ rapidity bite. In particular, the IQMD model seems to capture the basic trends of κ_n with N_{part} , including the presence of a curvature in κ_2 . However, in our simulations, all three codes used (IQMD, UrQMD, and HSD) generally miss the absolute magnitudes of κ_n , κ'_n , and κ''_n . In the present study, we refrained, however, from a more detailed comparison of our data with model calculations.

From the reduced cumulants κ_n , the full proton cumulants $K_n = N_{\text{part}} \kappa_n$ as well as their ratios are readily obtained. Cumulant ratios are shown as a function of N_{part} in Fig. 25 for rapidity bites $y \in y_0 \pm 0.2$ and $y \in y_0 \pm 0.4$. In contrast to the narrow midrapidity bin $y \in y_0 \pm 0.05$ (cf. Fig. 22), the deviation from the Poisson limit—where all K_n would be equal—is blatantly apparent: Except for the notable region around $N_{\text{part}} = 150$, cumulant ratios at all orders differ strongly from unity and they display, overall, a highly non-

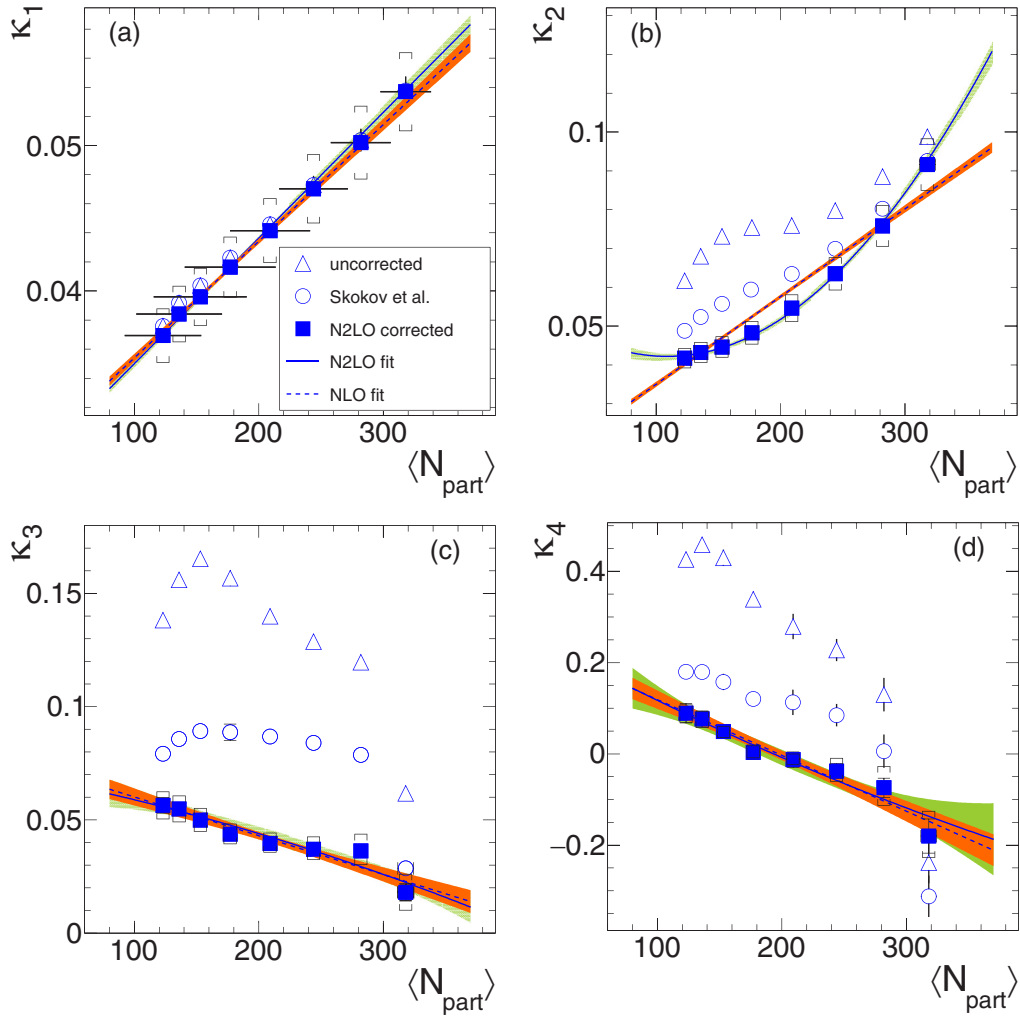


FIG. 23. Au + Au data: Efficiency and volume-corrected reduced proton cumulants κ_n for the phase-space bin $y \in y_0 \pm 0.2$ and $0.4 \leq p_t \leq 1.6$ GeV/ c as a function of mean N_{part} , using 5% centrality bins. Shown are the data without volume correction (open triangles), with Skokov *et al.* [77] correction (open circles), and with N2LO correction (solid squares). Vertical bars are statistical errors, cups delimit full systematic errors (shown on the N2LO corrected points only), and horizontal bars shown in panel (a) correspond to the width (± 1 s.d.) of the N_{part} distribution in the given centrality bin. Solid curves are N2LO fits, dashed curves are NLO fits (for comparison), and shaded bands are the ± 1 s.d. statistical errors of the fits (orange for NLO, olive for N2LO).

trivial N_{part} dependence. Ratios of cumulants are intensive (although not strongly intensive) quantities, meaning that they do not depend on the mean source volume. They are therefore often favored when directly comparing data from different experiments, where, e.g., the selected centralities may differ.

B. Correlators

As pointed out in Refs. [85–87], the essential information contained in particle number cumulants is related to the physics of multiparticle correlations, the underlying mechanism of which we hope to unravel. Indeed, the cumulants of a given order n contain contributions from multiparticle correlations of all orders up to n . The n -particle correlators C_n —also called factorial cumulants or connected cumulants or sometimes correlation functions—can be obtained straightforwardly from the cumulants K_n via Eq. (2). Making use of this general expression, we explicitly write down the correlators

up to the fourth order:

$$\begin{aligned}
 C_1 &= K_1, \\
 C_2 &= K_2 - K_1, \\
 C_3 &= K_3 - 3K_2 + 2K_1, \\
 C_4 &= K_4 - 6K_3 + 11K_2 - 6K_1.
 \end{aligned} \tag{11}$$

To illustrate their differences, Fig. 26 displays side by side the full set of measured proton cumulants (left column) and correlators (right column) as a function of the selected rapidity bin width Δy . Also, in Fig. 27 the dependence of the correlators C_n on the upper transverse momentum cut p_t^{max} is shown, demonstrating the saturation of C_n for a maximum momentum of $p_t \simeq 1.5$ GeV/ c ; this is likely due to the proton yield fading quickly with increasing p_t .

General arguments regarding the nature of multiparticle correlations have been discussed in Refs. [85,87]. In partic-

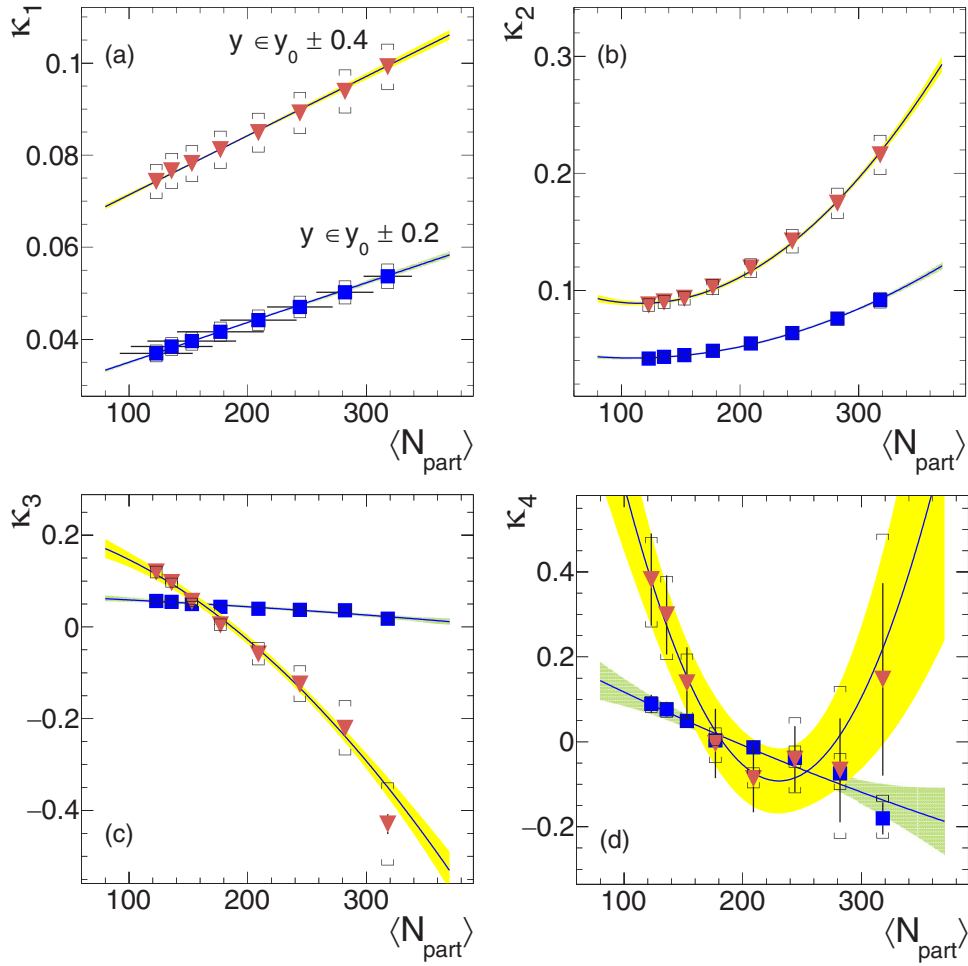


FIG. 24. Au + Au data: Efficiency and N2LO volume-corrected reduced proton cumulants as a function of mean N_{part} , using 5% centrality bins. Data from two phase-space selections are shown: $y \in y_0 \pm 0.2$ (blue squares) and $y \in y_0 \pm 0.4$ (red inverted triangles), both with $0.4 \leq p_t \leq 1.6$ GeV/c. Vertical bars are statistical errors on data, cups delimit full systematic errors; horizontal bars, shown in panel (a) only, correspond to the width (± 1 s.d.) of the N_{part} distribution in the given centrality bin. Solid curves are N2LO fits to the data and shaded bands are the ± 1 s.d. statistical fit errors.

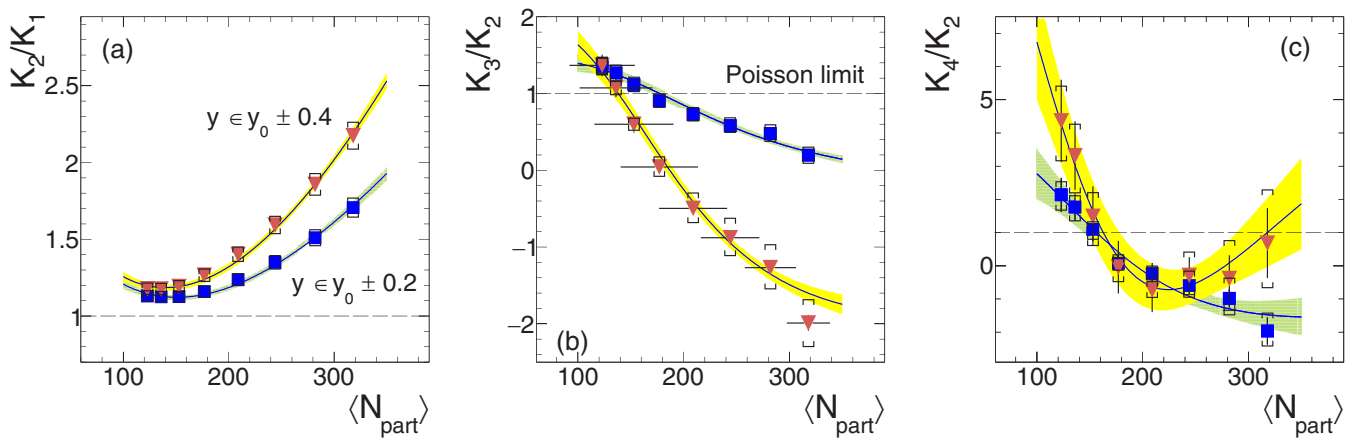


FIG. 25. Au + Au data: Efficiency and N2LO volume-corrected proton cumulant ratios as a function of mean N_{part} , using 5% centrality bins. Two selections are shown: $y \in y_0 \pm 0.2$ (blue squares) and $y \in y_0 \pm 0.4$ (red inverted triangles), both with $0.4 \leq p_t \leq 1.6$ GeV/c. Vertical error bars are statistical, cups demarcate full systematic errors; horizontal bars, shown in panel (b) only, depict the width (± 1 s.d.) of the N_{part} distribution within the given centrality bin. Solid curves are N2LO fits, shaded bands represent the corresponding ± 1 s.d. statistical fit errors. The horizontal dashed lines correspond to the Poisson limit where $K_1 = K_2 = K_3 = K_4$.

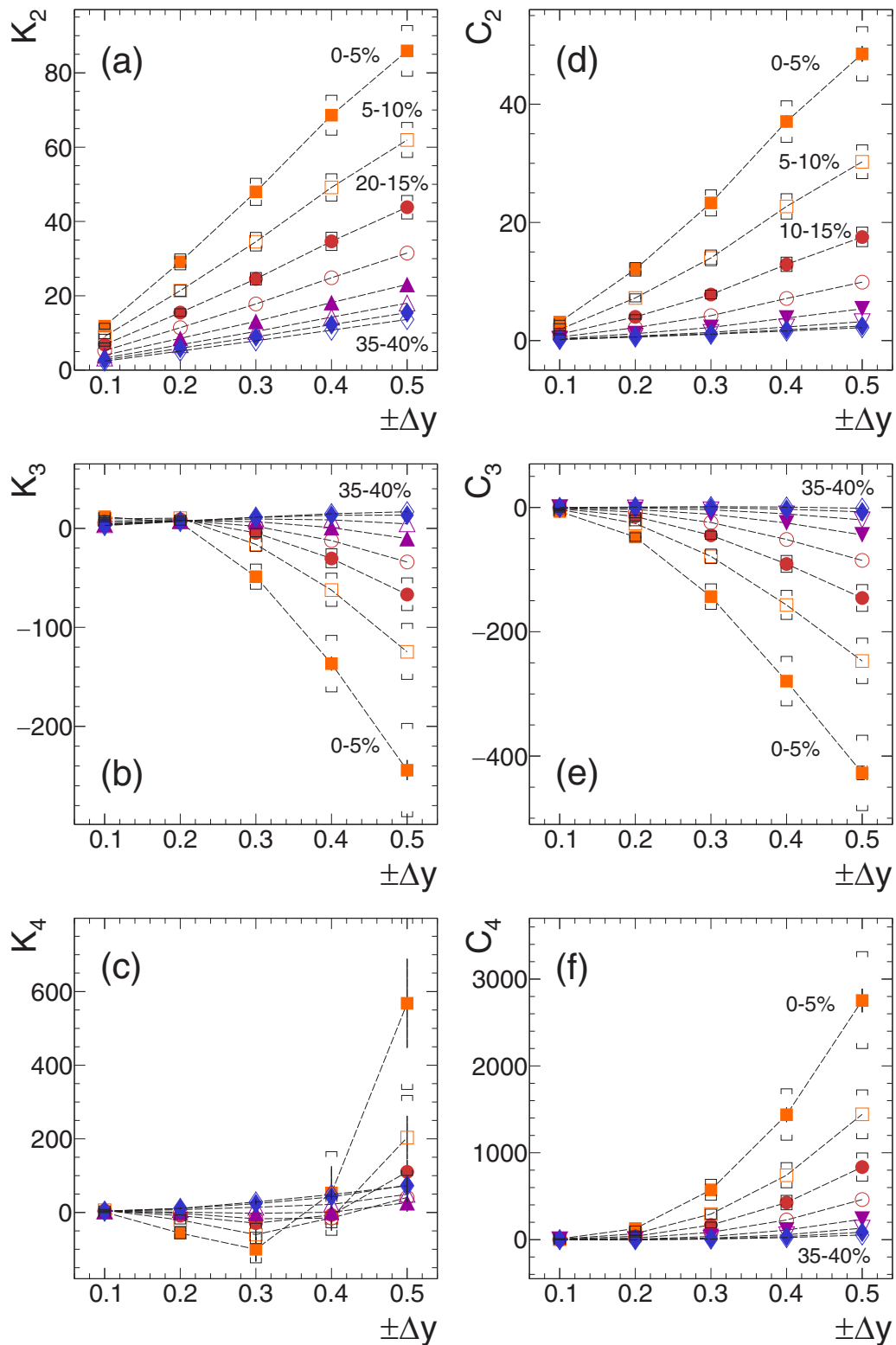


FIG. 26. Au + Au data: Efficiency and N2LO volume-corrected proton cumulants K_n [(a)–(c)] and correlators C_n [(d)–(f)], shown as a function of the rapidity bin $\pm\Delta y$, i.e., a phase space $y \in y_0 \pm \Delta y$ and $0.4 \leq p_t \leq 1.6$ GeV/c. Dashed lines connect data points for guidance only, bars are statistical errors, and cups indicate full systematic errors. To not clutter the graphs, the latter are shown only for a few of the centrality selections, i.e., 0–5%, 5–10%, and 10–15%.

ular, in Ref. [85] it was argued that the scaling of C_n with the mean number of particles emitted into a given phase-space bin Δy depends on the range Δy_{corr} in momentum space of these multiparticle correlations. Two regimes were considered: First, when very short-range correlations dominate, i.e., $\Delta y_{\text{corr}} \ll \Delta y$, one expects a linear scaling $C_n \propto \Delta y$; second, when long-range correlations are important, that is, $\Delta y_{\text{corr}} \gg \Delta y$, one expects a $C_n \propto (\Delta y)^n$ scaling of the correlators. However, the rationale underlying these considerations is given by the regime of heavy-ion collisions at RHIC and LHC where the number of detected particles is proportional to Δy . At low bombarding energies, the dN/dy distribution is typically bell shaped and it is better to discuss the C_n scalings directly in terms of the number of particles emitted into Δy . Hence, the two scaling regimes become $C_n \propto N$ for short-range correlations and $C_n \propto N^n$ for long-range correlations. This more adequate representation of the proton correlators as a function of mean number of protons $\langle N_p \rangle$ is shown in Fig. 28, together with power-law fits $C_n(N) = C_0 N^\alpha$, where the exponent α and the normalization constant C_0 are fit parameters. The exponents resulting from these fits are listed with their error²⁰ for all 5% centrality selections in Table III. One can see that, for the most central events, the values of α are approaching n for all C_n . This suggests that a setting close to the second scenario seems to be realized, that is, long-range correlations dominate the correlators in Au + Au collisions at $\sqrt{s_{NN}} = 2.4$ GeV. In other words, Δy_{corr} is of the same order or larger than the accepted rapidity range of $y_0 \pm 0.5$, that is $\Delta y_{\text{corr}} \geq 1$. It is also interesting to note that C_2 , unlike the higher orders, displays a somewhat more intricate scaling with $\langle N \rangle$, i.e., a drop of the exponent with the centrality of the collision. The meaning of this behavior remains presently unclear to us.

The reason for these unexpectedly strong long-range correlations is not obvious. We can only speculate that they could be caused by collective phenomena (e.g., flow fluctuations) or, if they are of truly critical nature, they might signal the close-by liquid-gas phase transition [88,89]. Indeed, in a recent model study using a hadron resonance gas with minimal van der Waals interactions [90–92], the fluctuation signal characterizing the liquid-gas endpoint was found to persist over a surprisingly large part of the phase diagram. A dynamic description is, however, still missing and it remains open how exactly the correlations observed at freeze-out in momentum space do relate to the spatial correlations build up in the initial state of the collision and/or during the expansion of the resulting fireball. Note that some of these issues have also been addressed by the authors of Refs. [15,85] when discussing the observable signals of critical fluctuations. The authors of Ref. [54] have recently demonstrated in more general terms that the observed behavior of the correlators C_n emerges naturally when the measured particle distribution results from the superposition of two event classes, both uncorrelated—Poisson or binomial—but with distinct mean multiplicities. Even a small contamination of order 10^{-3} of the main event

²⁰This error is mostly statistical as α was found to be very robust against systematic effects of types A, B, and C.

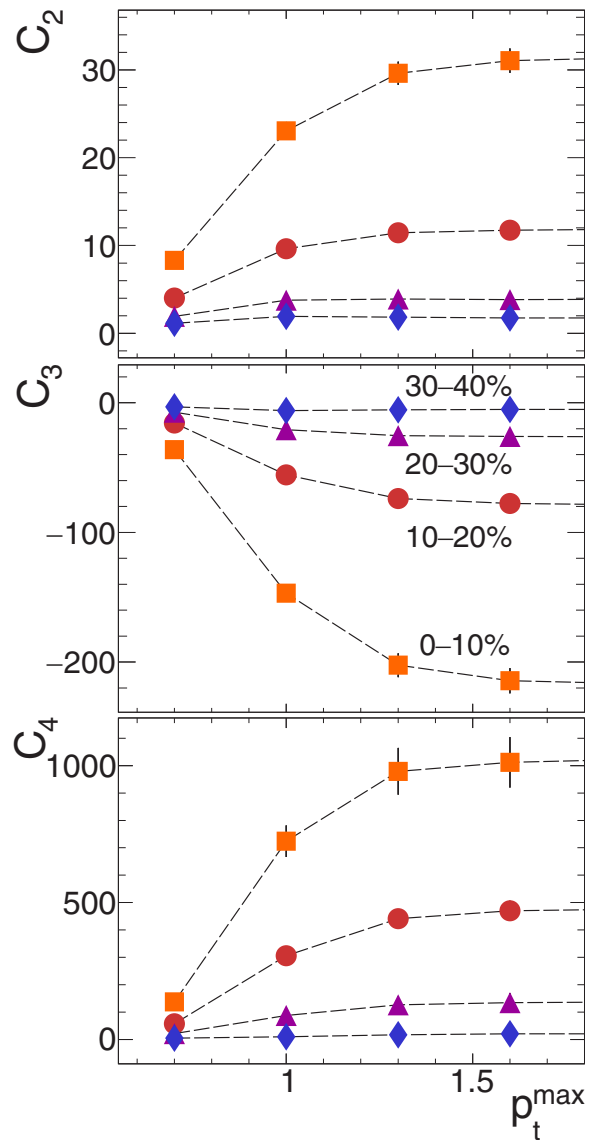


FIG. 27. Au + Au data: Efficiency and N2LO volume corrected proton number correlators C_n in the rapidity bin $y \in y_0 \pm 0.4$ as a function of the upper cut on transverse momentum p_t^{max} , shown here for 10% centrality bins. Error bars are statistical only. Saturation of the correlators is reached for $p_t^{\text{max}} \cong 1.5$ GeV/c.

class would lead to large values of the combined C_n . It is therefore very important to put limits on possible instrumental origins of such a contaminant, as we have discussed in Sec. II (see, in particular, Table I).

Note also that the proton number cumulants as well as their ratios are expected to be affected by baryon-number conservation effects [93–95]. Such effects have indeed been observed in LHC data [78,94] as deviations from the Skellam distribution expected in the grand canonical limit. Introducing an acceptance factor $a = \langle N_p \rangle / \langle N_B \rangle$ as the ratio of the mean number of protons accepted in a given phase-space bin and the corresponding total number of baryons, the authors of Ref. [94] could express the constraint of baryon-number conservation on the particle cumulants as function of a . In

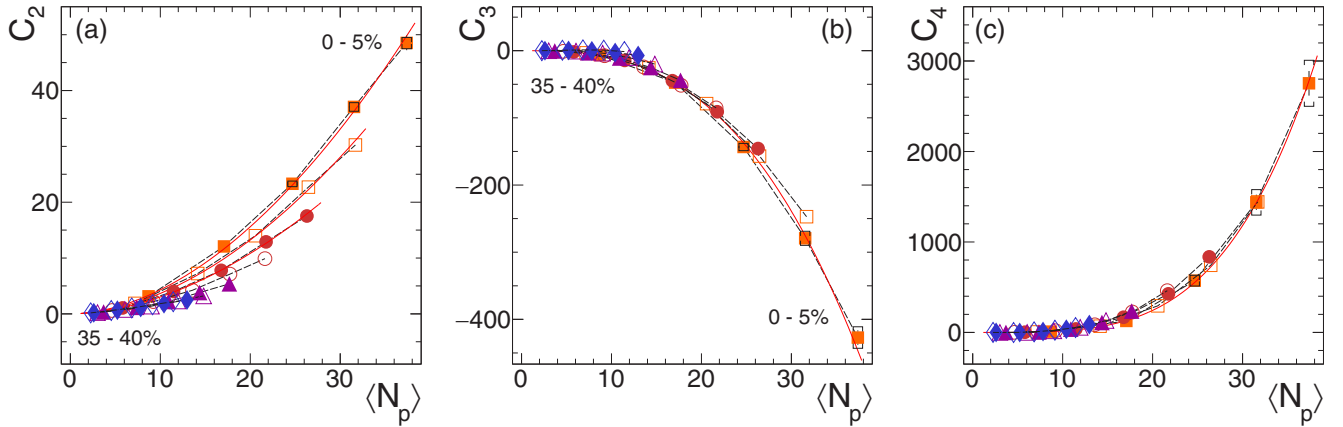


FIG. 28. Au + Au data: Efficiency and N2LO volume-corrected proton correlators C_n as a function of the mean number of protons $\langle N_p \rangle$ within the selected phase-space bin, $y \in y_0 \pm \Delta y$ ($\Delta y = 0.1, \dots, 0.5$) and $0.4 \leq p_t \leq 1.6$ GeV/ c , and for eight centrality selections. Error bars on data are statistical, cups delimit systematic uncertainties (shown, for clarity, only on the 0–5% selection). Black dashed lines connect the data points in a given centrality selection and red solid curves are power-law fits $C_n \propto \langle N_p \rangle^\alpha$. Only a few of the fit curves are actually presented; however, all adjusted values of parameter α are listed in Table III.

the low-energy regime, where the number of antibaryons drops to zero, the expected deviations of the cumulant ratios from the pure Poisson baseline, due to global baryon-number conservation, are then given by

$$\begin{aligned} K_2/K_1 &= 1 - a, \\ K_3/K_2 &= 1 - 2a, \\ K_4/K_2 &= 1 - 6a(1 - a). \end{aligned}$$

All three ratios are reduced by canonical suppression and our proton data, where a before efficiency correction is in the most central bin between 0.023 (for $y \in y_0 \pm 0.2$) and 0.051 (for $y \in y_0 \pm 0.5$), may be affected accordingly. Although a turns out to be rather small in our case, baryon-number conservation as well as similar constraints due to electric charge conservation will have to be accounted for in future model calculations. The direct effect on the particle correlators C_n has been discussed in Ref. [86] where it was found to display a scaling behavior very different from the one observed in Fig. 28.

At higher energies a beam energy scan has been conducted by the STAR Collaboration at RHIC for $\sqrt{s_{NN}} = 7.7$ –200 GeV and net-proton-number fluctuations have been analyzed and published [25–27,30,33]. In Fig. 29, we extend the STAR systematics of net-proton cumulant ratios $\gamma_1 \times \sigma$ and $\gamma_2 \times \sigma^2$ with our low-energy point at $\sqrt{s_{NN}} = 2.4$ GeV. The STAR analysis was done for all beam energies in the rapidity range covered by their TPC and time-of-flight detector, i.e., $y \in y_0 \pm 0.5$. It is not at all clear how the interplay between fluctuation signals from the central fireball and from spectator matter changes with energy, and how this affects the measurements in rapidity intervals of a given size, in particular at low beam energies where the proton rapidity distribution is more bell shaped and much narrower than at RHIC energies. Therefore, we present the comparison with HADES data for two choices of the rapidity bite: $y \in y_0 \pm$

0.2 and $y \in y_0 \pm 0.4$. We prefer ± 0.4 over the ± 0.5 choice because of justified fears that the latter, larger range contains sizable contributions from the abraded spectator matter. A naive estimate, based on a Fermi gas nucleon momentum of $p_F = 0.27$ GeV/ c , leads indeed to a safe rapidity region of about 0.28–1.20 (or $y_0 \pm 0.46$) for our bombarding energy; this is also born out by transport calculations done with the IQMD, UrQMD, and HSD models. As shown in Fig. 29, for both presented choices of the rapidity interval and for both centralities, the HADES data smoothly extend the K_3/K_2 trend observed by STAR toward lower $\sqrt{s_{NN}}$. This seems to be true as well for the K_4/K_2 trend in semiperipheral events, whereas in the most central events, the HADES data suggest a sharp decrease of the fourth-order ratio with respect to its value at the lowest STAR energy. One has to keep in mind, however, that the sizable gap remaining in the excitation function between $\sqrt{s_{NN}} = 2.4$ and 7.7 GeV will have to be covered by experiments before firm conclusions can be drawn.

TABLE III. Results of the power-law fits to the proton correlators shown in Fig. 28 using $C_n \propto \langle N_p \rangle^\alpha$. The fit parameter α and its statistical error are listed for 5% centrality selections. The few instances where the fit did not converge to a meaningful result are indicated by a dash. Systematic errors on α are small, typically smaller than the statistical error listed.

Centrality	$\alpha[C_2]$	$\alpha[C_3]$	$\alpha[C_4]$
0–5%	1.86 ± 0.04	2.84 ± 0.05	3.89 ± 0.14
5–10%	1.85 ± 0.04	2.85 ± 0.05	3.75 ± 0.13
10–15%	1.84 ± 0.05	2.80 ± 0.06	3.66 ± 0.14
15–20%	1.82 ± 0.07	2.83 ± 0.09	3.72 ± 0.22
20–25%	1.78 ± 0.09	2.95 ± 0.15	4.11 ± 0.44
25–30%	1.67 ± 0.10	3.44 ± 0.40	4.46 ± 0.82
30–35%	1.59 ± 0.10		4.76 ± 1.36
35–40%	1.55 ± 0.11		

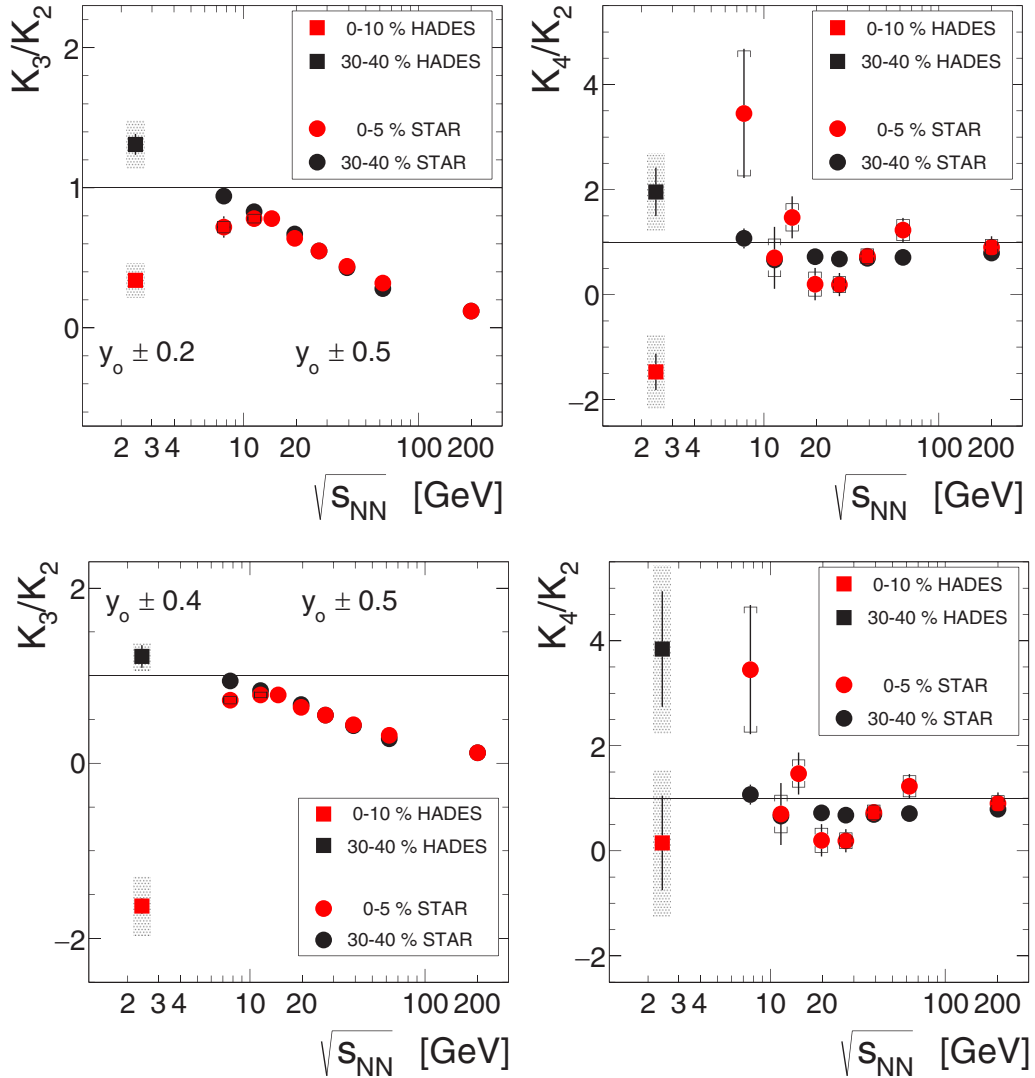


FIG. 29. Au + Au data: Evolution of the scaled cumulants K_n/K_2 as a function of center-of-mass energy $\sqrt{s_{NN}}$ for two centrality bins (0–10% or 0–5%, red symbols, and 30–40%, black symbols) and shown as $\gamma_1 \times \sigma$ (left column) and $\gamma_2 \times \sigma^2$ (right column). STAR data [27,33] is shown for a $y_0 \pm 0.5$ phase-space bite, and HADES data for $y_0 \pm 0.2$ (top row) and $y_0 \pm 0.4$ (bottom row), respectively. Vertical bars are statistical errors; full systematic errors are shown for the HADES data as shaded bars and for the STAR data points as caps.

VIII. SUMMARY AND OUTLOOK

To summarize, we have investigated with HADES proton multiplicity fluctuations in $\sqrt{s_{NN}} = 2.4$ GeV Au + Au collisions up to fourth order. In this context, we have done an in-depth investigation and comparison of various efficiency correction schemes, and we have in the end opted to apply a highly granular event-by-event correction to the measured proton cumulants to account for both phase-space interval dependent and track-density related efficiency changes. Furthermore, guided by transport model calculations, we have extended the procedure proposed in the literature for stripping off volume fluctuations by including the higher order correction terms required in the low-energy regime where HADES operates. The resulting fully corrected proton cumulants and correlators are presented and discussed as a function of centrality and phase-space acceptance. When only a very narrow rapidity bin is selected, we find that the observed proton

distributions are, as expected, close to Poisson. However, this behavior changes dramatically when the acceptance opens up and multiparticle correlations set in. In particular, from the dependence of the correlators on the number of emitted protons, we conclude that our results are dominated by rather long-range ($\Delta y_{\text{corr}} \geq 1$) correlations, strongly positive in second and fourth orders but negative in third order. Why and how these correlations in momentum space at freeze-out build up from spatial correlations in the initial state and/or expansion phase of the fireball remains to be investigated by theory. When joined with the STAR results [27,33] obtained in the first RHIC beam-energy scan, our data allow us to extend the excitation function of net-proton cumulants in central Au + Au collisions to low energies. While the present data show a rather smooth trend for K_3/K_2 with $\sqrt{s_{NN}}$, they indicate a distinctive change of sign of K_4/K_2 when moving from RHIC to SIS18 energies. Again, the interpretation of

these observations requires input from advanced quantitative calculations, e.g., hydro or transport models including phase boundaries.

An interesting avenue to follow next is to evaluate fluctuations of bound protons by including nuclear cluster production—foremost, deuteron, triton, and He isotopes—into the analysis. Indeed, in order to elucidate the origin of long-range correlations observed for free protons, the role played by protons bound in clusters might turn out to be decisive, as the latter represent at $\sqrt{s_{NN}} = 2.4$ GeV about 40% of the total number of protons emitted from the fireball [48]. Also, the HADES Collaboration has recently done a high-statistics measurement in $^{107}\text{Ag} + \text{Ag}$ collisions at the two bombarding energies of 1.23 and 1.58A GeV. These data provide the opportunity to study both the system size and, to some extent, the energy dependence of various fluctuation signals. We are furthermore looking forward to see results from the second beam-energy scan at RHIC [34], which will provide data at energies reaching down to $\sqrt{s_{NN}} = 3$ GeV. These, when combined with our measurements, will allow us to map fluctuation signals across the QCD phase diagram. Also, a dedicated beam-energy scan in the $\sqrt{s_{NN}} = 2\text{--}2.5$ GeV region, to be done at SIS18, could add vital information with regard to the liquid-gas phase transition. Further in the future, the heavy-ion experiments CBM at FAIR and MPD at NICA will produce comprehensive data sets of extremely large statistics and will thus extend the present studies to much higher precision and to higher orders.

ACKNOWLEDGMENTS

The HADES Collaboration thanks Adam Bzdak, Xiaofeng Luo, Mazakiyo Kitazawa, Volker Koch, and Nu Xu for elucidating discussions. We also thank Yvonne Leifels for providing the clusterized IQMD events to us. We gratefully acknowledge support by the following grants: SIP JUC Cracow, Cracow (Poland), National Science Center, Grants No. 2016/23/P/ST2/040 POLONEZ, No. 2017/25/N/ST2/00580, and No. 2017/26/M/ST2/00600; TU Darmstadt, Darmstadt (Germany), Grants No. VH-NG-823, No. DFG GRK 2128, No. DFG CRC-TR 211, and No. BMBF:05P18RDFC1; Goethe-University, Frankfurt (Germany), HIC for FAIR (LOEWE), Grants No. BMBF:06FY9100I, No. BMBF:05P12RFGHJ, and No. GSI F&E; Goethe-University, Frankfurt (Germany) and TU Darmstadt, Darmstadt (Germany), ExtreMe Matter Institute EMMI at GSI Darmstadt; TU München, Garching (Germany), MLL München, Grants No. DFG EClust 153, No. GSI TMLRG1316F, No. BMBF 05P15WOFCA, No. SFB 1258, and No. DFG FAB898/2-2; NRNU MEPhI Moscow, Moscow (Russia), in the framework of Russian Academic Excellence Project No. 02.a03.21.0005 (27.08.2013), RFBR No. 18-02-00086, and MSHE of Russia No. 0723-2020-0041; JLU Giessen, Giessen (Germany), Grant No. BMBF:05P12RGGHM; IPN Orsay, Orsay Cedex (France), Grant No. CNRS/IN2P3; and NPI CAS, Rez, Rez (Czech Republic), Grants No. MSMT LM2015049, No. OP VVV CZ.02.1.01/0.0/0.0/16 013/0001677, and No. LTT17003.

APPENDIX A: NONBINOMIAL EFFICIENCIES: THE OCCUPANCY MODEL

As discussed in Sec. III, efficiency corrections to particle number cumulants are usually done [61] assuming the efficiency to be binomial, i.e., assuming that the detection processes of multiple particles in any given event are independent. This can be described best with the help of a dichromatic urn model, where successive draws from the urn stand for particle detection processes: A white ball drawn is taken as “particle detected” and a black one as “particle not detected.” The initial state of the urn, i.e., the initial content of white and black balls, is chosen such that the ratio of the number of white balls to the total number of balls corresponds to the single-particle detection efficiency. How the state of the urn evolves with successive draws depends on the chosen addition rule. In the binomial case, the balls are drawn with replacement, meaning that every drawn ball is placed back into the urn which thus does not change its state. Successive draws are hence independent from each other; i.e., the urn does not have memory. The probability of obtaining p white balls in m draws or, equivalently, of detecting p out of m emitted particles in an event is described by

$$P(p; m) = \binom{m}{p} \epsilon^p (1 - \epsilon)^{m-p}, \quad (\text{A1})$$

where ϵ is the probability to detect a given particle and $\binom{m}{p}$ are binomial coefficients. By expanding the $(1 - \epsilon)$ term in Eq. (A1) and averaging $P(p; m)$ over the distribution of emitted particles, one finds a relationship between the average probability $P(p)$ to observe p particles in the detector and the factorial moments F_n of the true particle distribution [96]:

$$P(p) = \sum_{m=p}^{\infty} (-1)^{m-p} \frac{F_m}{m!} \binom{m}{p} \epsilon^m. \quad (\text{A2})$$

Using the definition of the observed factorial moments,

$$f_n = \sum_{p=n}^{\infty} P(p) p(p-1)\dots(p-n+1)$$

and inserting $P(p)$ from Eq. (A2), one retrieves for the binomial efficiency model the well-known relation between the measured f_n and the true F_n factorial moments [55,64,65]

$$f_n = \epsilon^n F_n. \quad (\text{A3})$$

Real-life detectors are commonly designed with a finite occupancy; they can register only a limited number of particles per given event and consequently their detection efficiency eventually decreases with ever increasing particle number. This effect can be studied in simulations, and for HADES the efficiency drop was found to be of order 10–15% (see Sec. III). Deviations from the binomial assumption have been discussed in Refs. [67,97] and the authors of Ref. [67] considered in particular the hypergeometric and β -binomial distributions. Like the binomial distribution, these two distributions can also be derived from a dichromatic urn model. In the hypergeometric model, balls are drawn without replacement, i.e., they are not put back, and the urn state changes while it gets

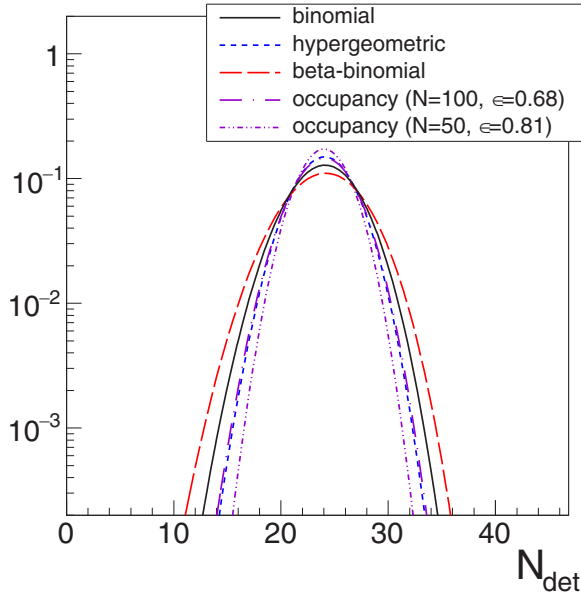


FIG. 30. Comparison of the normalized distribution of detected particles N_{det} resulting from different efficiency models: binomial, hypergeometric, β -binomial, and our occupancy model (see text). In all cases, the input number of particles is $N_{\text{in}} = 40$ and the parameters of the models are adjusted to realize an average efficiency of $\langle \epsilon \rangle = 0.6$, resulting in $\langle N_{\text{det}} \rangle = 24$. Calculations done with the occupancy model are shown for two segmentations: $N = 100$, with a single-hit efficiency of $\epsilon = 0.68$, and $N = 50$, with $\epsilon = 0.81$.

successively emptied of balls. The resulting hypergeometric distribution of white balls obtained per given number of draws is narrower than the binomial distribution (see Fig. 30). For the β -binomial model, on the other hand, balls are drawn with double replacement, meaning that for a white draw, two white balls are put back and for a black draw, two black balls. Again, the state of the urn changes, but the resulting β -binomial distribution is now broader than the binomial distribution (cf. Fig. 30). Although the properties of both of these *ad hoc* models are well known, their connection to physical phenomena playing a role in the actual detection process is not obvious.

Here we propose another urn model, known as the occupancy model [68], that offers a more intuitive connection with the behavior of detectors under particle bombardment. In the occupancy model, balls are drawn with the following replacement rule: A drawn black ball (“not detected”) is just put back into the urn, but a drawn white ball (“detected”) is not put back; instead it is replaced by a black ball put to the urn. The state of the urn changes as the number of white balls gets depleted, realizing a decrease in efficiency. In this picture, each white ball represents one active detector module that turns inert or busy when hit by a particle and thus has to be replaced by a black ball to keep constant the total solid angle covered by the device. The occupancy model naturally applies to detectors segmented into a finite number N of modules of solid angle Ω each such that the total active solid angle covered is $\epsilon = N\Omega$. Any given module can fire when hit by a particle, but only once; i.e., multiple hits of a module are

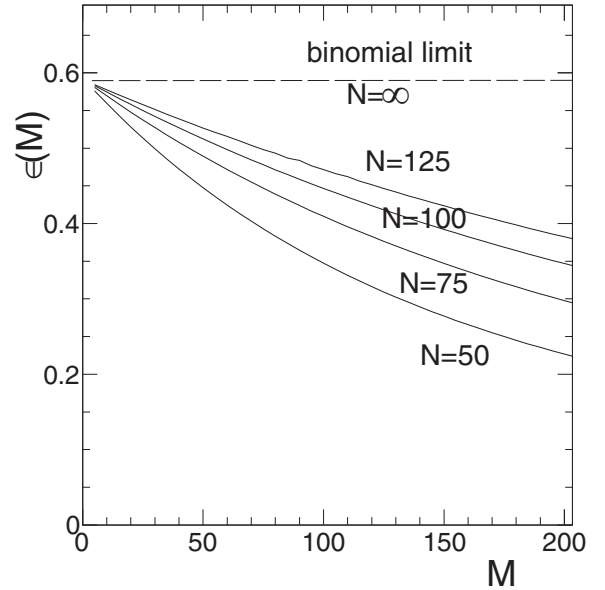


FIG. 31. Nonbinomial efficiencies of the occupancy model as a function of the particle multiplicity m for $\epsilon \equiv N\Omega = 0.59$ and different values of N .

not distinguishable from single hits. Following the approach presented in Refs. [96,98], the binomial multihit detection probability of Eq. (A1) transforms into

$$P(p; m, N) = \binom{N}{p} \sum_{l=0}^p (-1)^{p-l} \binom{p}{l} \left(1 - \frac{N-l}{N} \epsilon\right)^m. \quad (\text{A4})$$

The resulting distribution of detected particles, shown in Fig. 30, is wider than binomial. Note that, for a given ϵ , the average number of detected particles decreases with respect to the binomial case; i.e., the average efficiency is smaller than ϵ . In addition, the relation between factorial moments changes from Eq. (A3) into

$$f_n = \sum_{m=n}^N \frac{(-1)^m}{m!} F_m \sum_{p=n}^m (-1)^p \binom{N}{p} p(p-1) \dots (p-n+1) \sum_{l=0}^p (-1)^l \binom{p}{l} \left(\frac{N-l}{N} \epsilon\right)^m. \quad (\text{A5})$$

Unlike Eq. (A3), Eq. (A5) is not diagonal anymore; i.e., an observed factorial moment of order n depends on all true factorial moments F_m of orders $n \leq m \leq N$. Solving this system of equations for large N requires eventually a truncation at some sufficiently high order. We found, furthermore, that calculations with Eq. (A5) need to be done with high numerical precision (at least 64-bit, if not 128-bit floating-point arithmetic) in order to produce reliable results. This had already been pointed out in Ref. [99] where also a faster converging expansion of the hit probabilities in terms of cumulants was proposed.

Figure 31 illustrates the drop of the effective efficiency $\epsilon_{\text{eff}} = \epsilon(m)$ with particle multiplicity m and its dependence on the segmentation N of the detector; for $N = \infty$, the binomial

case is recovered. For a “continuous” detector like HADES, a strict hardware segmentation into N distinct modules is not realized, but an effective segmentation \tilde{N} can still be introduced, with \tilde{N} and Ω adjusted to describe the observed (or simulated) average efficiency behavior $\langle \epsilon_{\text{eff}} \rangle = \epsilon(\tilde{N}, \Omega)$. Such an adjustment to IQMD simulated proton moments is also shown in Fig. 14.

APPENDIX B: NLO VOLUME-FLUCTUATION CORRECTIONS

Here we list once more the reduced particle number cumulants $\tilde{\kappa}_n$ with all slope-related terms, i.e., NLO volume-fluctuation terms, including order $n = 4$ (see Sec. IV for details):

$$\tilde{\kappa}_1 = \kappa_1 + v_2 \kappa'_1, \quad (\text{B1})$$

$$\tilde{\kappa}_2 = \kappa_2 + \kappa_1^2 v_2 + \kappa_2' v_2 + 2\kappa_1 \kappa_1' v_2 + 2\kappa_1 \kappa_1' v_3 + 2\kappa_1^2 v_2 v_2 + \kappa_1^2 V_1 V_2 + 2\kappa_1^2 V_3 + \kappa_1^2 v_4, \quad (\text{B2})$$

$$\begin{aligned} \tilde{\kappa}_3 = & \kappa_3 + \kappa_1^3 v_3 + 3\kappa_1 \kappa_2 v_2 + 3(\kappa_1 \kappa_2' + \kappa_1' \kappa_2) v_3 + 6\kappa_1' (\kappa_1^2 + \kappa_2') v_2 v_2 + 3\kappa_1' (\kappa_1^2 + 2\kappa_2') V_3 \\ & + 3\kappa_1' (\kappa_1^2 + \kappa_2') v_4 + 12\kappa_1 \kappa_1^2 V_2^2 + 3\kappa_1 \kappa_1^2 V_1 V_3 + 24\kappa_1 \kappa_1^2 v_2 v_3 + 6\kappa_1 \kappa_1^2 V_4 + 3\kappa_1 \kappa_1^2 v_5 + \kappa_3' v_2 \\ & + 3(\kappa_1 \kappa_2' + \kappa_1' \kappa_2) V_2 + 8\kappa_1^3 v_2 v_2^2 + 6\kappa_1^3 V_1 V_2^2 + 10\kappa_1^3 v_3 v_3 + \kappa_1^3 V_1^2 V_3 + 24V_2 v_3 \kappa_1^3 \\ & + 3\kappa_1^3 V_1 V_4 + 12\kappa_1^3 v_2 v_4 + 3\kappa_1^3 v_5 + \kappa_1^3 v_6 + 3\kappa_1' \kappa_2' V_1 V_2, \end{aligned} \quad (\text{B3})$$

$$\begin{aligned} \tilde{\kappa}_4 = & \kappa_4 + \kappa_1^4 v_4 + 6\kappa_1^2 \kappa_2 v_3 + (4\kappa_1 \kappa_3 + 3\kappa_2^2) v_2 + 24(\kappa_1^3 \kappa_1' + 4\kappa_1 \kappa_1' \kappa_2' + 2\kappa_1^2 \kappa_2) v_2 v_3 \\ & + 4(\kappa_1^3 \kappa_1' + 6\kappa_1 \kappa_1' \kappa_2' + 3\kappa_1^2 \kappa_2) V_4 + 2(2\kappa_1^3 \kappa_1' + 6\kappa_1 \kappa_1' \kappa_2' + 3\kappa_1^2 \kappa_2) v_5 \\ & + 48(\kappa_1^2 \kappa_1^2 + \kappa_1^2 \kappa_2') v_2 v_2^2 + 12(4\kappa_1^2 \kappa_1^2 + 5\kappa_1^2 \kappa_2') v_3 v_3 + 72(\kappa_1^2 \kappa_1^2 + 2\kappa_1^2 \kappa_2') V_2 V_3 \\ & + 6(\kappa_1^2 \kappa_1^2 + 3\kappa_1^2 \kappa_2') V_1 V_4 + 72(\kappa_1^2 \kappa_1^2 + \kappa_1^2 \kappa_2') v_2 v_4 + 6(2\kappa_1^2 \kappa_1^2 + 3\kappa_1^2 \kappa_2') V_5 \\ & + 6(\kappa_1^2 \kappa_1^2 + \kappa_1^2 \kappa_2') v_6 + 2(6\kappa_1^2 \kappa_2' + 12\kappa_1 \kappa_1' \kappa_2 + 4\kappa_1' \kappa_3 + 3\kappa_2^2) v_2 v_2 \\ & + 2(3\kappa_1^2 \kappa_2' + 6\kappa_1 \kappa_1' \kappa_2 + 4\kappa_1' \kappa_3 + 3\kappa_2^2) V_3 + 2(3\kappa_1^2 \kappa_2 + 2\kappa_1 \kappa_3 + 2\kappa_1' \kappa_3 + 3\kappa_2 \kappa_2') v_3 \\ & + (6\kappa_1^2 \kappa_2' + 12\kappa_1 \kappa_1' \kappa_2 + 4\kappa_1' \kappa_3 + 3\kappa_2^2) v_4 + 96\kappa_1 \kappa_1^3 v_2^3 + 96\kappa_1 \kappa_1^3 v_3^2 + 288\kappa_1 \kappa_1^3 v_3 v_2^2 \\ & + 72\kappa_1 \kappa_1^3 V_1 V_2 V_3 + 4\kappa_1 \kappa_1^3 V_1^2 V_4 + 144\kappa_1 \kappa_1^3 v_2 v_4 + 128\kappa_1 \kappa_1^3 v_3 v_4 + 12\kappa_1 \kappa_1^3 V_1 V_5 \\ & + 72\kappa_1 \kappa_1^3 v_2 v_5 + 12\kappa_1 \kappa_1^3 v_6 + 4\kappa_1 \kappa_1^3 v_7 + 24(2\kappa_1 \kappa_1' \kappa_2' + \kappa_1^2 \kappa_2) v_2^2 + 6(2\kappa_1 \kappa_1' \kappa_2' + \kappa_1^2 \kappa_2) V_1 V_3 \\ & + 2(2\kappa_1 \kappa_3 + 2\kappa_1' \kappa_3 + 3\kappa_2 \kappa_2') v_2 + 48\kappa_1^4 v_2 v_3^2 + 48\kappa_1^4 v_1 v_2^3 + 48\kappa_1^4 v_1 v_3^2 + 240\kappa_1^4 v_2 v_3^2 \\ & + 32\kappa_1^4 v_4 v_4 + 288\kappa_1^4 v_2^2 v_3 + 24\kappa_1^4 v_1^2 v_2 v_3 + \kappa_1^4 v_1^3 v_4 + 144\kappa_1^4 v_4 v_2^2 + 72\kappa_1^4 v_1 v_2 v_4 \\ & + 128\kappa_1^4 v_3 v_4 + 4\kappa_1^4 v_1^2 v_5 + 72\kappa_1^4 v_2 v_5 + 56\kappa_1^4 v_3 v_5 + 6\kappa_1^4 v_1 v_6 + 24V_2 v_6 \kappa_1^4 v_2 v_6 + 4\kappa_1^4 v_7 \\ & + \kappa_1^4 v_8 + 36\kappa_1^2 \kappa_2' v_1 v_2^2 + 6\kappa_1^2 \kappa_2' v_1^2 v_3 + 4\kappa_1' \kappa_3 v_1 v_2 + 3\kappa_2^2 v_1 v_2 + \kappa_4' v_2. \end{aligned} \quad (\text{B4})$$

APPENDIX C: THE FOUR-PARAMETER β DISTRIBUTION

The scheme proposed in Sec. IV for volume-fluctuation corrections of the observed particle-number cumulants, namely by subtraction of all volume terms, requires the N_{part} distribution of the applied centrality selection. While a distribution is in principle fully characterized by its moments or cumulants, a straightforward Taylor expansion requires knowledge of all moments or at least of a sufficiently large number of them to keep the truncation error small. More efficient schemes have however been proposed, for example, the Poisson-Charlier expansion, which approximates a given distribution on the basis of its factorial cumulants by a sum of forward difference operators applied to the Poisson distribution [40,100]. In Ref. [40], such an expansion has been used to model the STAR proton distributions but, as also pointed out by the authors, the method can lead to unphysical results, e.g., a negative yield. This is also our observation, since typically only the first few moments of a distribution are

reliably known. Hence we took a different, more pragmatic approach based on the four-parameter β distribution [57] which is always positive and, in all cases of interest to our analysis, is unimodal.

Starting from the usual definition of the β probability distribution on the support interval $[0,1]$, one arrives at

$$f(x; p, q) = \frac{x^{p-1} (1-x)^{q-1}}{B(p, q)}, \quad (\text{C1})$$

where p and q are dimensionless shape parameters fulfilling $p, q > 0$ and $B(p, q)$ is the β function. The latter one provides proper normalization to unity and it is defined with help of the Γ function $\Gamma(z)$:

$$B(p, q) = \frac{\Gamma(p)\Gamma(q)}{\Gamma(p+q)}.$$

The mean, variance, skewness γ_1 , and excess kurtosis γ_2 of the β distribution are given by [57]

$$E[X] = \frac{p}{p+q},$$

$$\text{Var}[X] = \frac{pq}{(p+q)^2(p+q+1)},$$

$$\gamma_1[X] = \frac{2(p-q)\sqrt{p+q+1}}{(p+q+2)\sqrt{pq}},$$

$$\gamma_2[X] = \frac{6[(p-q)^2(p+q+1) - pq(p+q+2)]}{pq(p+q+2)(p+q+3)}. \quad (\text{C2})$$

Note that all moments are determined by the two shape parameters p and q which can be mapped unambiguously onto skewness and excess kurtosis, with the restriction that $2 < \gamma_2 < \frac{3}{2}\gamma_1^2$. This also implies that γ_1 and γ_2 cannot both be zero.

In order to extend the range of the β distribution beyond $[0,1]$, we introduce two additional parameters, a scaling r and a shift s , via the linear transformation

$$x \mapsto x' = rx + s.$$

With this, Eq. (C1) becomes

$$f(x'; p, q, r, s) = \frac{\left(\frac{x'-s}{r}\right)^{p-1} \left(1 - \frac{x'-s}{r}\right)^{q-1}}{rB(p, q)}, \quad (\text{C3})$$

now defined on the support interval $[s, s+r]$. The resulting extended four-parameter β distribution $f(x'; p, q, r, s)$ can be used to approximate unimodal distributions for which the first four moments are given: p and q are obtained directly from the dimensionless skewness and kurtosis, the scaling r is determined by the variance (or width $\sigma' = r\sigma$), and lastly, the shift parameter s is fixed by the mean ($\langle x' \rangle = r\langle x \rangle + s$). Indeed, introducing the variable v as

$$v = p + q = \frac{3(\gamma_2 - \gamma_1^2 + 2)}{\frac{3}{2}\gamma_1^2 - \gamma_2},$$

parameters p and q can be obtained from skewness and kurtosis with

$$\gamma_1 = 0: \quad p = q = \frac{v}{2} = \frac{\frac{3}{2}\gamma_2 + 3}{-\gamma_2},$$

$$\gamma_1 \neq 0: \quad p, q = \frac{v}{2} \left\{ 1 \pm \left[1 + \frac{16(v+1)}{(v+2)^2 \gamma_1^2} \right]^{-1} \right\}.$$

Next, the scaling parameter r follows from the width

$$r = \frac{\sigma}{2} \sqrt{(v+2)^2 \gamma_1^2 + 16(v+1)}.$$

And last, from the mean, the shift parameter s is obtained with

$$s = \langle x' \rangle - \frac{pr}{v}.$$

The ability of Eq. (C3) to render various unimodal function shapes is illustrated in Fig. 32 with a set of distributions having same mean and width, but different values of the higher order shape parameters γ_1 and γ_2 .

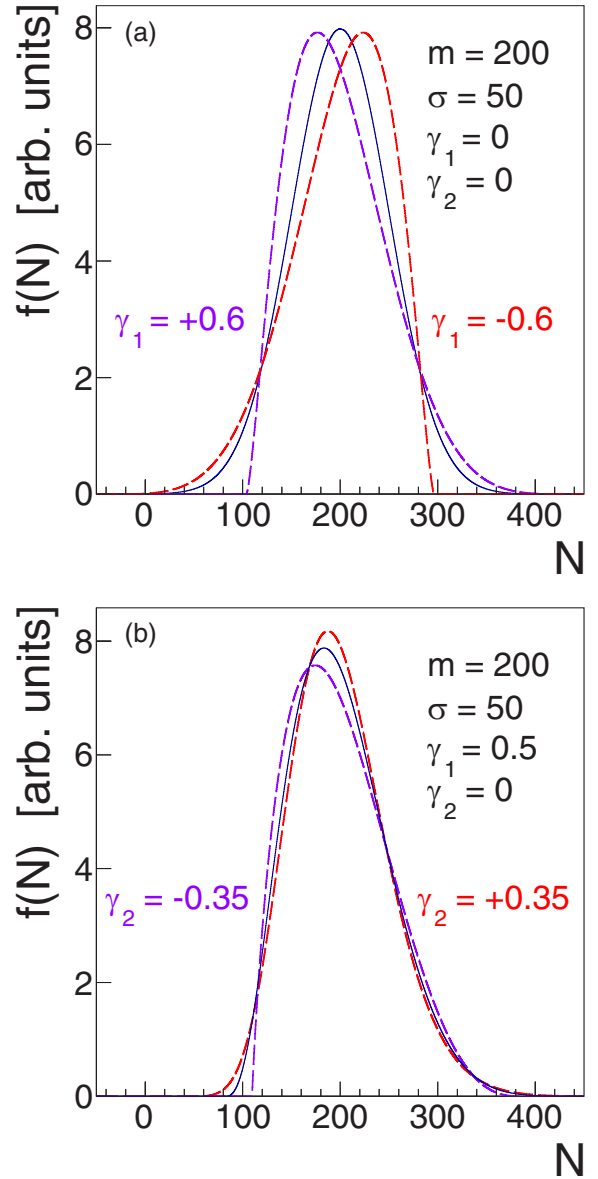


FIG. 32. Illustration of the four-parameter β distribution [Eq. (C3), not normalized]. The effect of nonzero skewness (a) and nonzero kurtosis (b) on the distribution shape is shown. Note that the limits $\gamma_1 \simeq 0$ and $\gamma_2 \simeq 0$ approximate the $N(200, 50)$ normal distribution also plotted in panel (a).

The extent to which unimodal distributions can be approximated by Eq. (C3) is demonstrated in Fig. 33, where the four-parameter β distribution is compared to N_{part} distributions obtained from IQMD transport model calculations. These were done for different centrality selections on the HADES forward wall sum of charges signal, as discussed in Sec. V (see also Fig. 20). In all cases, the first four moments agree by construction and any visible residual deviations are caused by moments of order higher than 4. In the fluctuation analysis of our Au + Au data, we have also used Eq. (C3) to visualize the experimental N_{part} distributions (see Fig. 21). To improve

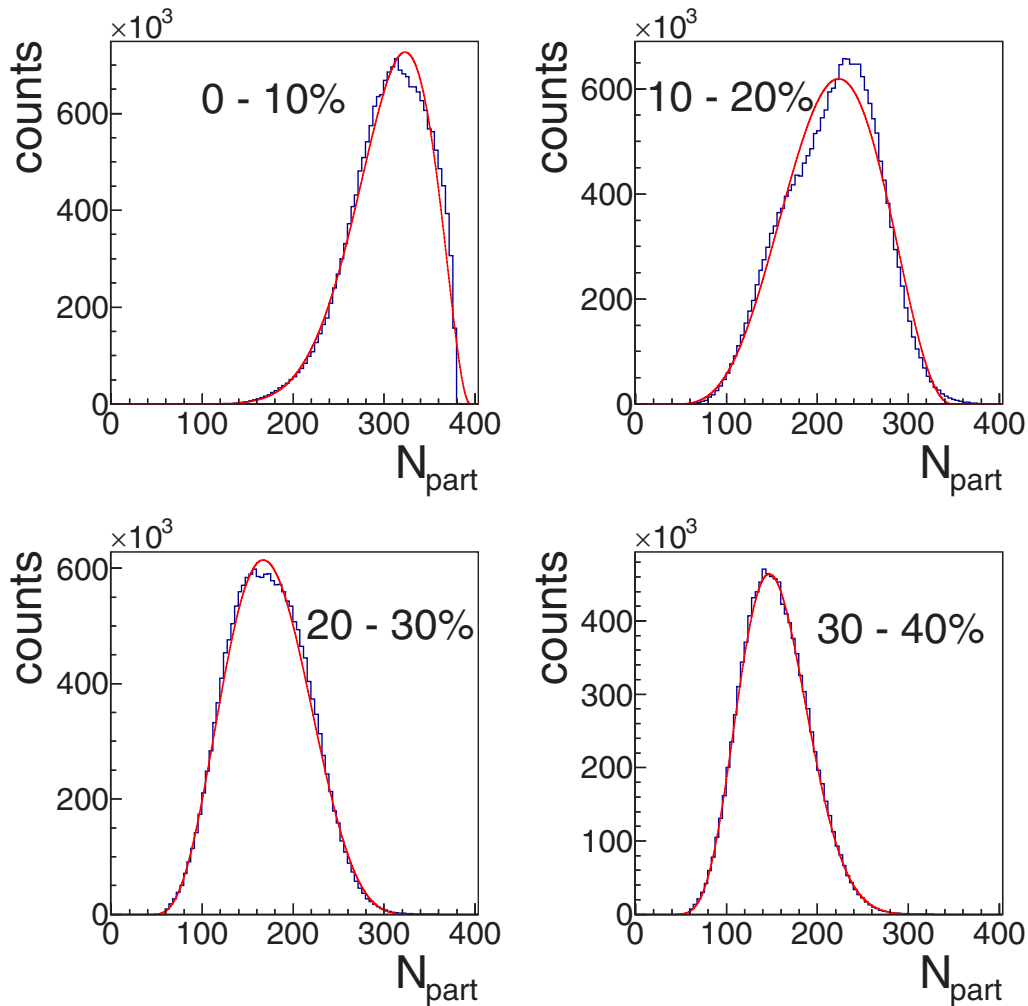


FIG. 33. Comparison of the four-parameter β distribution (red line) with the true N_{part} distributions (dark blue histogram) obtained from IQMD for four different centrality selections. For each selection, the two distributions are normalized to the same number of counts.

the quality of this modeling, moments beyond fourth order would have to be included and hence a more sophisticated

expansion, like Gram-Charlier [57] or Poisson-Charlier [101], would have to be employed.

-
- [1] Y. Aoki, G. Endrődi, Z. Fodor, S. D. Katz, and K. K. Szabó, *Nature (London)* **443**, 675 (2006).
- [2] A. Bazavov, T. Bhattacharya, C. DeTar, H. T. Ding, S. Gottlieb, R. Gupta, P. Hegde, U. M. Heller, F. Karsch, E. Laermann *et al.* (HotQCD Collaboration), *Phys. Rev. D* **90**, 094503 (2014).
- [3] M. Stephanov, *Prog. Theor. Phys. Suppl.* **153**, 139 (2004).
- [4] Y. Hatta and M. A. Stephanov, *Phys. Rev. Lett.* **91**, 102003 (2003).
- [5] M. A. Stephanov, *Phys. Rev. Lett.* **102**, 032301 (2009).
- [6] M. Asakawa, S. Ejiri, and M. Kitazawa, *Phys. Rev. Lett.* **103**, 262301 (2009).
- [7] V. V. Begun, M. Gaździcki, M. I. Gorenstein, and O. S. Zozulya, *Phys. Rev. C* **70**, 034901 (2004).
- [8] M. Kitazawa and M. Asakawa, *Phys. Rev. C* **86**, 024904 (2012).
- [9] M. Stephanov, K. Rajagopal, and E. Shuryak, *Phys. Rev. D* **60**, 114028 (1999).
- [10] B. Berdnikov and K. Rajagopal, *Phys. Rev. D* **61**, 105017 (2000).
- [11] M. Bluhm, Y. Jiang, M. Nahrgang, J. M. Pawłowski, F. Rennecke, and N. Wink, *Nucl. Phys. A* **982**, 871 (2019).
- [12] C. Athanasiou, K. Rajagopal, and M. Stephanov, *Phys. Rev. D* **82**, 074008 (2010).
- [13] M. A. Stephanov, *Phys. Rev. Lett.* **107**, 052301 (2011).
- [14] V. Koch, in *Relativistic Heavy Ion Physics* (Springer, Heidelberg, 2010), pp. 626–652.
- [15] M. Asakawa and M. Kitazawa, *Prog. Part. Nucl. Phys.* **90**, 299 (2016).
- [16] A. Bzdak, S. I. Esumi, V. Koch, J. Liao, M. Stephanov, and N. Xu, *Phys. Rep.* **853**, 1 (2020).
- [17] C. Alt, T. Anticic, B. Baatar, D. Barna, J. Bartke, L. Betev, H. Białkowska, C. Blume, B. Boimska, M. Botje, J. Bracinić,

- R. Bramm, P. Bunčić, V. Cerny, P. Christakoglou *et al.* (NA49 Collaboration), *Phys. Rev. C* **76**, 024914 (2007).
- [18] C. Alt, T. Anticic, B. Baatar, D. Barna, J. Bartke, L. Betev, H. Białkowska, C. Blume, B. Boimska, M. Botje, J. Bracinik, R. Bramm, P. Bunčić, V. Cerny, P. Christakoglou *et al.* (NA49 Collaboration), *Phys. Rev. C* **78**, 034914 (2008).
- [19] T. Anticic, B. Baatar, D. Barna, J. Bartke, H. Beck, L. Betev, H. Białkowska, C. Blume, M. Bogusz, B. Boimska, J. Book, M. Botje, P. Bunčić, T. Cetner, P. Christakoglou *et al.* (NA49 Collaboration), *Phys. Rev. C* **87**, 024902 (2013).
- [20] T. Anticic, B. Baatar, J. Bartke, H. Beck, L. Betev, H. Białkowska, C. Blume, B. Boimska, J. Book, M. Botje, P. Bunčić, P. Christakoglou, P. Chung, O. Chvala, J. Cramer *et al.* (NA49 Collaboration), *Phys. Rev. C* **89**, 054902 (2014).
- [21] T. Anticic, B. Baatar, D. Barna, J. Bartke, L. Betev, H. Białkowska, C. Blume, B. Boimska, M. Botje, J. Bracinik, P. Bunčić, V. Cerny, P. Christakoglou, P. Chung *et al.* (NA49 Collaboration), *Phys. Rev. C* **81**, 064907 (2010).
- [22] T. Anticic, B. Baatar, J. Bartke, H. Beck, L. Betev, H. Białkowska, C. Blume, M. Bogusz, B. Boimska, J. Book, M. Botje, P. Bunčić, T. Cetner, P. Christakoglou, O. Chvala, J. Crame *et al.* (NA49 Collaboration), *Eur. Phys. J. C* **75**, 587 (2015).
- [23] M. Maćkowiak-Pawlowska (NA61/SHINE Collaboration), *EPJ Web of Conferences* **206**, 03003 (2019).
- [24] K. Grebieszko *et al.* (NA61/SHINE Collaborator), *PoS (CORFU2018)*, 152 (2019).
- [25] M. M. Aggarwal, Z. Ahammed, A. V. Alakhverdyants, I. Alekseev, J. Alford, B. D. Anderson, D. Arkhipkin, G. S. Averichev, J. Balewski, L. S. Barnby, S. Baumgart *et al.* (STAR Collaboration), *Phys. Rev. Lett.* **105**, 022302 (2010).
- [26] L. Adamczyk, J. K. Adkins, G. Agakishiev, M. M. Aggarwal, Z. Ahammed, I. Alekseev, J. Alford, C. D. Anson, A. Aparin, D. Arkhipkin, E. C. Aschenauer, G. S. Averichev *et al.* (STAR Collaboration), *Phys. Rev. Lett.* **112**, 032302 (2014).
- [27] X. Luo, in *Proceedings of the 9th International Workshop on Critical Point and Onset of Deconfinement—PoS (CPOD2014) 019* (Sissa Medialab, Italy, 2015).
- [28] A. Rustamov, *Nucl. Phys. A* **967**, 453 (2017).
- [29] A. Adare, S. S. Adler, S. Afanasiev, C. Aidala, N. N. Ajitanand, Y. Akiba, H. Al-Bataineh, J. Alexander, A. Al-Jamel, K. Aoki, L. Aphecetche, R. Armendariz *et al.* (PHENIX Collaboration), *Phys. Rev. C* **78**, 044902 (2008).
- [30] L. Adamczyk, J. K. Adkins, G. Agakishiev, M. M. Aggarwal, Z. Ahammed, I. Alekseev, J. Alford, C. D. Anson, A. Aparin, D. Arkhipkin, E. C. Aschenauer, G. S. Averichev *et al.* (STAR Collaboration), *Phys. Rev. Lett.* **113**, 092301 (2014).
- [31] A. Adare, S. Afanasiev, C. Aidala, N. N. Ajitanand, Y. Akiba, R. Akimoto, H. Al-Bataineh, J. Alexander, H. Al-Ta'ani, A. Angerami, K. Aoki, N. Apadula *et al.* (STAR Collaboration), *Phys. Rev. C* **93**, 011901 (2016).
- [32] L. Adamczyk, J. R. Adams, J. K. Adkins, G. Agakishiev, M. M. Aggarwal, Z. Ahammed, N. N. Ajitanand, I. Alekseev, D. M. Anderson, R. Aoyama, A. Aparin, D. Arkhipkin, E. C. Aschenauer, M. U. Ashraf *et al.*, *Phys. Lett. B* **785**, 551 (2018).
- [33] J. Adam, L. Adamczyk, J. R. Adams, J. K. Adkins, G. Agakishiev, M. M. Aggarwal, Z. Ahammed, I. Alekseev, D. M. Anderson, A. Aparin, E. C. Aschenauer, M. U. Ashraf, F. G. Atetalla, A. Attri, G. S. Averichev, V. Bairathi, K. Barish, A. Behera, R. Bellwied *et al.* (STAR Collaboration), [arXiv:2001.02852](https://arxiv.org/abs/2001.02852) [nucl-ex].
- [34] C. Yang (STAR Collaboration), *Nucl. Phys. A* **967**, 800 (2017).
- [35] G. Agakishiev, A. Balanda, B. Bannier, R. Bassini, D. Belver, A. V. Belyaev, A. Blanco, M. Boehmer, J. L. Boyard, P. Braun-Munzinger, P. Cabanelas, E. Castro, S. Chernenko, T. Christ, M. Destefanis, J. Diaz, F. Dohrmann, A. Dybczak, T. Eberl *et al.* (HADES Collaboration), *Eur. Phys. J. A* **41**, 243 (2009).
- [36] J. Pietraszko, T. Galatyuk, V. Grilj, W. Koenig, S. Spataro, and M. Träger, *Nucl. Instrum. Methods Phys. Res. A* **763**, 1 (2014).
- [37] B. Klinger, B. Lommel, A. Hübner, W. Hartmann, and J. Steiner, *Nucl. Instrum. Methods Phys. Res. A* **655**, 95 (2011).
- [38] J. Adamczewski-Musch, O. Arnold, C. Behnke, A. Belounnas, A. Belyaev, J. C. Berger-Chen, J. Biernat, A. Blanco, C. Blume, M. Böhmer, P. Bordalo, S. Chernenko, L. Chlad, C. Deveaux *et al.* (HADES Collaboration), *Eur. Phys. J. A* **54**, 85 (2018).
- [39] W. Reisdorf *et al.*, *Nucl. Phys. A* **612**, 493 (1997).
- [40] A. Bzdak, V. Koch, D. Oliinychenko, and J. Steinheimer, *Phys. Rev. C* **98**, 054901 (2018).
- [41] P. Garg and D. K. Mishra, *Phys. Rev. C* **96**, 044908 (2017).
- [42] X. Luo, J. Xu, B. Mohanty, and N. Xu, *J. Phys. G: Nucl. Part. Phys.* **40**, 105104 (2013).
- [43] S. Bass, *Prog. Part. Nucl. Phys.* **41**, 255 (1998).
- [44] R. Brun, *GEANT 3.21, Detector Description and Simulation Tool*, CERN Long Writeup No. W5013 (CERN, Geneva, Switzerland, 1993).
- [45] C. Hartnack, R. K. Puri, J. Aichelin, J. Konopka, S. Bass, H. Stöcker, and W. Greiner, *Eur. Phys. J. A* **1**, 151 (1998).
- [46] P.-B. Gossiaux and J. Aichelin, *Phys. Rev. C* **56**, 2109 (1997).
- [47] Y. Leifels (private communication).
- [48] M. Szala *et al.* (HADES Collaboration), in *The XVIII International Conference on Strangeness in Quark Matter (SQM 2019)*, Springer Proceedings in Physics Vol. 250, edited by D. Elia, G. Bruno, P. Colangelo, and L. Cosmai (Springer, Berlin, 2020).
- [49] O. Pechenova, V. Pechenov, T. Galatyuk, T. Hennino, R. Holzmann, G. Kornakov, J. Markert, C. Müntz, P. Salapura, A. Schmah, E. Schwab, and J. Stroth, *Nucl. Instrum. Methods Phys. Res., Sec. A* **785**, 40 (2015).
- [50] C. Zeitnitz and T. Gabriel, *Nucl. Instrum. Methods Phys. Res., Sec. A* **349**, 106 (1994).
- [51] J. Adamczewski-Musch, O. Arnold, C. Behnke, A. Belounnas, A. Belyaev, J. C. Berger-Chen, J. Biernat, A. Blanco, C. Blume, M. Böhmer, P. Bordalo, S. Chernenko, L. Chlad, C. Deveaux *et al.* (HADES Collaboration), *Phys. Lett. B* **793**, 457 (2019).
- [52] X. Luo, *J. Phys. G: Nucl. Part. Phys.* **39**, 025008 (2012).
- [53] X. Luo, *Phys. Rev. C* **91**, 034907 (2015).
- [54] A. Bzdak and V. Koch, *Phys. Rev. C* **100**, 051902(R) (2019).
- [55] A. Bzdak and V. Koch, *Phys. Rev. C* **86**, 044904 (2012).
- [56] X. Luo and N. Xu, *Nucl. Sci. Tech.* **28**, 112 (2017).
- [57] A. Stuart and K. Ord, *Kendall's Advanced Theory of Statistics: Distribution Theory* (John Wiley & Sons, Chichester, UK, 2004), Vol. 1.
- [58] W. Broniowski and A. Olszewski, *Phys. Rev. C* **95**, 064910 (2017).
- [59] P. J. Smith, *Am. Stat.* **49**, 217 (1995).

- [60] Q. Zheng, *Comput. Stat.* **17**, 507 (2002).
- [61] A. Bzdak and V. Koch, *Phys. Rev. C* **91**, 027901 (2015).
- [62] M. Kitazawa, *Phys. Rev. C* **93**, 044911 (2016).
- [63] T. Nonaka, M. Kitazawa, and S. I. Esumi, *Phys. Rev. C* **95**, 064912 (2017).
- [64] M. Kirejczyk, *Acta Phys. Pol. B* **35**, 2425 (2004).
- [65] S. He and X. Luo, *Chin. Phys. C* **42**, 104001 (2018).
- [66] M. Kitazawa and X. Luo, *Phys. Rev. C* **96**, 024910 (2017).
- [67] A. Bzdak, R. Holzmann, and V. Koch, *Phys. Rev. C* **94**, 064907 (2016).
- [68] H. Mahmoud, *Pólya Urn Models* (CRC Press, Boca Raton, FL, 2008).
- [69] P. Garg, D. K. Mishra, P. K. Netrakanti, A. K. Mohanty, and B. Mohanty, *J. Phys. G: Nucl. Part. Phys.* **40**, 055103 (2013).
- [70] R. Brun and F. Rademakers, *Nucl. Instrum. Methods Phys. Res., Sec. A* **389**, 81 (1997).
- [71] G. D'Agostini, *Nucl. Instrum. Methods Phys. Res., Sec. A* **A362**, 487 (1995).
- [72] A. Höcker and V. Kartvelishvili, *Nucl. Instrum. Methods Phys. Res., Sec. A* **372**, 469 (1996).
- [73] S. Schmitt, *J. Instrum.* **7**, T10003 (2012).
- [74] W. Tang, X. Li, X. Qian, H. Wei, and C. Zhang, *J. Instrum.* **12**, P10002 (2017).
- [75] T. Nonaka, M. Kitazawa, and S. I. Esumi, *Nucl. Instrum. Methods Phys. Res., Sec. A* **906**, 10 (2018).
- [76] O. Behnke, K. Kröniger, G. Schott, and T. Schöner-Sadenius (eds.), *Data Analysis in High Energy Physics* (Wiley-VCH, Weinheim, Germany, 2013).
- [77] V. Skokov, B. Friman, and K. Redlich, *Phys. Rev. C* **88**, 034911 (2013).
- [78] P. Braun-Munzinger, A. Rustamov, and J. Stachel, *Nucl. Phys. A* **960**, 114 (2017).
- [79] J. Arndt, *Matters Computational: Ideas, Algorithms, Source Code* (Springer, Heidelberg, 2011).
- [80] W. Cassing and E. Bratkovskaya, *Phys. Rep.* **308**, 65 (1999).
- [81] T. Sugiura, T. Nonaka, and S. I. Esumi, *Phys. Rev. C* **100**, 044904 (2019).
- [82] B. Efron, *Ann. Stat.* **7**, 1 (1979).
- [83] B. Efron, *J. Am. Stat. Assoc.* **82**, 171 (1987).
- [84] A. Pandav, D. Mallick, and B. Mohanty, *Nucl. Phys. A* **991**, 121608 (2019).
- [85] B. Ling and M. A. Stephanov, *Phys. Rev. C* **93**, 034915 (2016).
- [86] A. Bzdak, V. Koch, and N. Strodthoff, *Phys. Rev. C* **95**, 054906 (2017).
- [87] A. Bzdak and V. Koch, *Phys. Rev. C* **96**, 054905 (2017).
- [88] P. J. Siemens, *Nature (London)* **305**, 410 (1983).
- [89] B. Borderie and J. Frankland, *Prog. Part. Nucl. Phys.* **105**, 82 (2019).
- [90] V. Vovchenko, M. I. Gorenstein, and H. Stoecker, *Phys. Rev. Lett.* **118**, 182301 (2017).
- [91] V. Vovchenko, L. Jiang, M. I. Gorenstein, and H. Stoecker, *Phys. Rev. C* **98**, 024910 (2018).
- [92] R. V. Poberezhnyuk, V. Vovchenko, A. Motornenko, M. I. Gorenstein, and H. Stöcker, *Phys. Rev. C* **100**, 054904 (2019).
- [93] A. Bzdak, V. Koch, and V. Skokov, *Phys. Rev. C* **87**, 014901 (2013).
- [94] P. Braun-Munzinger, A. Rustamov, and J. Stachel, *Nucl. Phys. A* **982**, 307 (2019).
- [95] C. A. Pruneau, *Phys. Rev. C* **100**, 034905 (2019).
- [96] S. Van der Werf, *Nucl. Instrum. Methods* **153**, 221 (1978).
- [97] A. H. Tang and G. Wang, *Phys. Rev. C* **88**, 024905 (2013).
- [98] G. Bellia, A. D. Zoppo, E. Migneco, and G. Russo, *Nucl. Instrum. Methods Phys. Res.* **226**, 424 (1984).
- [99] W. J. Ockels, *Z. Phys. A* **286**, 181 (1978).
- [100] K. M. R. Audenaert, [arXiv:0809.4155](https://arxiv.org/abs/0809.4155) [math.ST].
- [101] A. D. Barbour, *Ann. Probab.* **15**, 748 (1987).